University of Potsdam
Faculty of Science
Institute of Chemistry

A combined approach for the analysis of biomolecules using IR-MALDI ion mobility spectrometry and molecular dynamics simulations of peptide ions in the gas phase

by

José Andrés Villatoro Leal

A thesis submitted for the degree of
"Doctor rerum naturalium" (Dr. rer. nat.)
in Physical Chemistry
to the Institute of Chemistry, Faculty of Science, University of Potsdam

Defended on November 05 2018 in Potsdam

Reviewers:

Prof. Dr. Hans-Gerd Löhmannsröben
P.D. Dr. Marcus Weber
Prof. Dr. Bend Abel

ZIB

to measure is to know
SALSA

Published online at the
Institutional Repository of the University of Potsdam:
URN urn:nbn:de:kobv:517-opus4-419723
http://nbn-resolving.de/urn:nbn:de:kobv:517-opus4-419723

Publications

- As “Paper in the Forefront”: José Villatoro, Martin Zühlke, Daniel Riebe, Jens Riedel, Toralf Beitz, and Hans-Gerd Löhmannsröben. 2016. “IR-MALDI Ion Mobility Spectrometry.” *Anal Bioanal Chem* 408 (23): 6259–68. doi: 10.1007/s00216-016-9739-x.
- José Villatoro, Martin Zühlke, Daniel Riebe, Toralf Beitz, Marcus Weber, Jens Riedel, and Hans-Gerd Löhmannsrüben. 2016. “IR-MALDI Ion Mobility Spectrometry: Physical Source Characterization and Application as HPLC Detector.” *International Journal for Ion Mobility Spectrometry 19* (4). Springer Verlag: 197–207. doi: 10.1007/s12127-016-0208-1.
- José Villatoro, Marcus Weber, Martin Zühlke, Amadeus Lehmann, Karl Zenichowski, Daniel Riebe, Toralf Beitz, Hans-Gerd Löhmannsröben, Oliver Kreuzer. Working paper. “Structural characterization of peptides using electrospray ion mobility spectrometry and collision cross-section determination based on molecular dynamics.”

Conference presentations

- J. Villatoro, D. Riebe, T. Beitz, M. Weber, H.-G. Löhmannsröben. “High field mobility of polyatomic ions determined by IR-MALDI Ion Mobility Spectrometry at Intermediate Pressure”. **Poster**, *26th International Conference on Ion Mobility Spectrometry*, Warsaw (Poland), July 2017.
- J. Villatoro. “Low and High Field Mobilities determined by IR-MALDI Ion Mobility Spectrometry: From atmospheric pressure to reduced pressure measurements”. **Oral presentation**, *Bunsentagung*, Kaiserslautern (Germany), May 26 2017.
- J. Villatoro, D. Riebe, T. Beitz, M. Weber, H.-G. Löhmannsröben. “IR-MALDI Ion Mobility Spectrometry: Low and High Field Mobilities of Peptide Ions at Intermediate Pressure”. **Poster**, *50th annual conference of the German Society for Mass Spectrometry (DGMS)*, Kiel (Germany), March 2017.
- J. Villatoro, A. Erler, D. Riebe, T. Beitz, M. Weber, H.-G. Löhmannsröben. “Low and High Field Mobilities determined by IR-MALDI Ion Mobility Spectrometry at Intermediate Pressure”. **Poster**, *Future of Chemical Physics (Sponsored by The Journal of Chemical Physics)*, Oxford (UK) September 2016.
- J. Villatoro, M. Zühlke, A. Erler, D. Riebe, T. Beitz, M. Weber, H.-G. Löhmannsröben. “Low and High Field Mobilities determined by Laser-based IMS at Intermediate Pressure”. **Oral presentation**, *25th International Conference on Ion Mobility Spectrometry*, Boston (USA), July 22 2016.
- J. Villatoro, M. Zühlke, D. Riebe, T. Beitz, H.-G. Löhmannsröben. “IR-MALDI Ion Mobility Spectrometry: Characterization and applications”. **Oral presentation**, *International Conference on Applied Optics and Photonics 2016 – 117th annual conference of the German Society for Applied Optics (DGaO)*, Hannover (Germany), May 13 2016.
- J. Villatoro, M. Zühlke, D. Riebe, T. Beitz, H.-G. Löhmannsröben. “IR-MALDI-IMS: Characterization and applications”. **Poster**, *6. Anwendertreffen Ionenmobilitätsspektrometrie*, Hannover (Germany), February 2016.

- J. Villatoro, D. Riebe, J. Riedel, T. Beitz, H.-G. Löhmannsröben. “Ion mobility spectrometry for the study of dispersion and ionization processes in IR-FL-MALDI”. **Poster**, *49th annual conference of the German Society for Mass Spectrometry (DGMS)*, Hamburg (Germany), February 2016.
- J. Villatoro, M. Zühlke, D. Riebe, T. Beitz, H.-G. Löhmannsröben. “IR-FL-MALDI ion mobility spectrometry for the detection of proteins and peptides”. **Oral presentation**, *24th International Conference on Ion Mobility Spectrometry*, Córdoba (Spain), July 24 2015.
- J. Villatoro, M. Zühlke, D. Riebe, T. Beitz, H.-G. Löhmannsröben. “An IR-MALDI ion mobility spectrometer as HPLC Detector”. **Poster***, HPLC 2015 — The 42nd International Symposium on High Performance Liquid Phase Separations and Related Techniques*, Geneva (Switzerland), June 2015.
- J. Villatoro, M. Zühlke, D. Riebe, T. Beitz, H.-G. Löhmannsröben. “IR-MALDI Ion Mobility Spectrometry”. **Poster**, *ANAKON*, Graz (Austria), March 2015.

Zusammenfassung

Das Ziel dieser Arbeit war die Zusammenführung der schonende Ionisationsquelle Infrared Matrix-Assisted Laser Dispersion Ionization (IR-MALDI), der Isomer-diskriminierende Ionenmobilitätsspektrometrie und einer neuartigen, auf Molecular Dynamics (MD) Simulationen basierte Berechnungsmethode für Stoßquerschnitte.

Der erste Schritt war die Charakterisierung des Flüssigkeitsdispersionsphänomens in IR-MALDI: Zwei verschiedenen Ionentransportmechanismen wurden nachgewiesen und weiter studiert. Die Beziehung zwischen Peakform, Diffusion, Desolvatation und Ionen Extraktionspuls wurde beschrieben. Die Geschwindigkeit der Ionen, die aus dem Dispersionsphänomen stammen, wurde durch Ionenmobilitätsspektrometrie und Shadowgraphie untersucht. Shadowgraphie hat ebenfalls das Verhalten des Dispersionsphänomens erläutert. Eine hohe, schnell abklingende initielle Geschwindigkeit wurde beobachtet.

Das Verständnis des IR-MALDI Verfahrens ermöglichte die Optimierung der verschiedenen Ionenmobilität (IM) Spektrometer zum analytischen Zweck. Eine Atmosphärendruck- und zwei Niederdruckvariante von IM Spektrometern wurden mit gepulster Ionenextraktion genutzt. Die Pulsparameter (Pulsverzögerung, -breite, -höhe) und verschiedene elektrische Felder an unterschiedlichen Stellen der Spektrometer wurden systematisch variiert. Deren Einfluss auf die Peakauflösung und -fläche wurde untersucht und im Rahmen des IR-MALDI Verfahrens erklärt. Das Verständnis der Anatomie der Anfangsionenwolke wurde ebenfalls durch diese Experimente vertieft.

Die analytische Leistungsfähigkeit eines IM-Spektrometers wurde dann untersucht. Nachweisgrenzen und lineare Bereiche wurden bestimmt und in Zusammenhang mit dem IR-MALDI Verfahren interpretiert. Anhand der Trennung von Isomeren und einfachen Mischungen wurde die Anwendung dieser Technik demonstriert und ihre Vorteile, die Detektion einfachgeladener Ionen und die Möglichkeit der HPLC-Kopplung (High Performance Liquid Chromatography), aufgezeigt. Mit dem Niederdruckspektrometer wurde der Einfluss hoher reduzierter Feldstärken auf die Ionenmobilität von polyatomische Ionen in polyatomische Gasen untersucht.

Der letzte Schwerpunkt war die Charakterisierung von Peptidionen. Die Peptiden wurden mit Elektrospray (ESI) IM-Spektrometrie vermessen. Der hieraus erhaltene Datensatz diente zur Etablierung einer Stoßquerschnitt Berechnungsmethode mittels MD. Anstatt verschiedener Kandidat-Strukturen und deren Stoßquerschnitte, ergibt diese neuartige semi-automatisierte Methode einen einzigen, gemittelten Stoßquerschnitt. Die MD Methode wurde dann mit einer anderen, einfacheren Methode und mit den experimentellen Ergebnissen von ESI und IR-MALDI-IM Spektrometrie verglichen. Zudem wurde der Zusammenhang zwischen Ladungszustands- und Stoßquerschnittsdifferenzen zwischen den Peptiden untersucht. Weitere Strukturelle Informationen konnten aus den Simulationen extrahiert, und zur Charakterisierung der Peptiden verwendet werden.

Abstract

The aim of this doctoral thesis was to establish a technique for the analysis of biomolecules with infrared matrix-assisted laser dispersion (IR-MALDI) ion mobility (IM) spectrometry. The main components of the work were the characterization of the IR-MALDI process, the development and characterization of different ion mobility spectrometers, the use of IR-MALDI-IM spectrometry as a robust, standalone spectrometer and the development of a collision cross-section estimation approach for peptides based on molecular dynamics and thermodynamic reweighting.

First, the IR-MALDI source was studied with atmospheric pressure ion mobility spectrometry and shadowgraphy. It consisted of a metal capillary, at the tip of which a self-renewing droplet of analyte solution was met by an IR laser beam. A relationship between peak shape, ion desolvation, diffusion and extraction pulse delay time (pulse delay) was established. First order desolvation kinetics were observed and related to peak broadening by diffusion, both influenced by the pulse delay. The transport mechanisms in IR-MALDI were then studied by relating different laser impact positions on the droplet surface to the corresponding ion mobility spectra. Two different transport mechanisms were determined: phase explosion due to the laser pulse and electrical transport due to delayed ion extraction. The velocity of the ions stemming from the phase explosion was then measured by ion mobility and shadowgraphy at different time scales and distances from the source capillary, showing an initially very high but rapidly decaying velocity. Finally, the anatomy of the dispersion plume was observed in detail with shadowgraphy and general conclusions over the process were drawn.

Understanding the IR-MALDI process enabled the optimization of the different IM spectrometers at atmospheric and reduced pressure (AP and RP, respectively). At reduced pressure, both an AP and an RP IR-MALDI source were used. The influence of the pulsed ion extraction parameters (pulse delay, width and amplitude) on peak shape, resolution and area was systematically studied in both AP and RP IM spectrometers and discussed in the context of the IR-MALDI process. Under RP conditions, the influence of the closing field and of the pressure was also examined for both AP and RP sources. For the AP ionization RP IM spectrometer, the influence of the inlet field (IF) in the source region was also examined. All of these studies led to the determination of the optimal analytical parameters as well as to a better understanding of the initial ion cloud anatomy.

The analytical performance of the spectrometer was then studied. Limits of detection (LOD) and linear ranges were determined under static and pulsed ion injection conditions and interpreted in the context of the IR-MALDI mechanism. Applications in the separation of simple mixtures were also illustrated, demonstrating good isomer separation capabilities and the advantages of singly charged peaks. The possibility to couple high performance liquid chromatography (HPLC) to IR-MALDI-IM spectrometry was also demonstrated. Finally, the reduced pressure spectrometer was used to study the effect of high reduced field strength on the mobility of polyatomic ions in polyatomic gases.

The last focus point was on the study of peptide ions. A dataset obtained with electrospray IM spectrometry was characterized and used for the calibration of a collision cross-section (CCS) determination method based on molecular dynamics (MD) simulations at high temperature.

Instead of producing candidate structures which are evaluated one by one, this semi-automated method uses the simulation as a whole to determine a single average collision cross-section value by reweighting the CCS of a few representative structures. The method was compared to the intrinsic size parameter (ISP) method and to experimental results. Additional MD data obtained from the simulations was also used to further analyze the peptides and understand the experimental results, an advantage with regard to the ISP method. Finally, the CCS of peptide ions analyzed by IR-MALDI were also evaluated with both ISP and MD methods and the results compared to experiment, resulting in a first validation of the MD method. Thus, this thesis brings together the soft ionization technique that is IR-MALDI, which produces mostly singly charged peaks, with ion mobility spectrometry, which can distinguish between isomers, and a collision cross-section determination method which also provides structural information on the analyte at hand.

Table of Contents

Acknowledgments

I would like to thank everyone who has made it possible for me to be where I am today. From family, first and foremost, to friends, colleagues and everyone in between, without you this work would have never been possible. The list is simply too long to name you all. You know who you are, so to you I simply say thank you, danke, gracias and merci.

Abbreviations

ACN:	Acetonitrile
AP:	Atmospheric pressure
CCS:	Collision cross-section
CHCA:	α-cyano-4-hydroxycinnamic acid
CRM:	Charge residue model
DEDMAB:	Dodecylethyldimethylammonium bromide
DHB:	2,5-dihydroxybenzoic acid
DMAC:	Dimethylammonium chloride
EHSS:	Elastic hard sphere scattering
ELDI:	Electrospray-assisted laser desorption ionization
ESI:	Electrospray ionization
FWHM:	Full width at half maximum
GC:	Gas chromatography
HPLC:	High performance liquid chromatography
IEM:	Ion evaporation model
IF:	Inlet field
ILM:	Ionic liquid matrix
IM:	Ion mobility
IIR:	Incomplete ion recombination
IR:	Infrared
IR-FL-MALDI:	Infrared free liquid matrix assisted laser dispersion ionization
ISP:	Intrinsic size parameters
LADESI:	Laser-assisted desorption electrospray ionization
LAESI:	Laser ablation electrospray ionization
LEMS:	Laser electrospray mass spectrometry
LILBID:	Laser-induced liquid beam/bead ionization/desorption
MAB:	Methylammonium bromide
MALDESI:	Matrix-assisted laser desorption electrospray ionization

MALDI:	Matrix-assisted laser desorption ionization
MC:	Monte Carlo
MD:	Molecular dynamics
MS:	Mass spectrometry
OPO:	Optical parametric oscillator
PA:	Projection approximation
PA:	Pulse amplitude
PD:	Pulse delay
PEEK:	Polyether ether ketone
PSA:	Projected superposition approximation
PW:	Pulse width
RP:	Reduced pressure
SA:	Sinapic acid
SEDI:	Scattering on electron density isosurfaces
SPE:	Supercritical phase expansion
SATP:	Standard atmospheric temperature and pressure; 298.15 K and 100 kPa
STP:	Standard temperature and pressure; 273.15 K and 101,325 Pa
TBAB:	Tetrabutylammonium bromide
TDAB:	Tetradecylammonium bromide
THAB:	Tetrahexylammonium bromide
TM:	Trajectory method
TOAB:	Tetraoctylammonium bromide
UV:	Ultraviolet

Nomenclature

Latin

A:	Free energy
A_{g}:	Gaussian function amplitude
$\Delta_{ij}A$:	Free energy difference between states i and j
A_{S}:	Solvation peak area
A'_{S}:	Raw peak tailing area
A_{T}:	Total peak area
a:	Morse potential parameter. $a = (k_{ij}^{r}/2\varepsilon_{\mathrm{m}})^{1/2}$
b:	Impact parameter
b_{min}:	Minimum impact parameter to avoid a hard sphere collision
c_{a}:	Speed of sound in a medium
D:	Diffusion coefficient
D :	Diffusion tensor
$\mathcal{D}$:	Operator
D_{L}:	Longitudinal diffusion coefficient
D_{T}:	Transverse diffusion coefficient
d:	Distance
E:	Electric field
E_{IR}:	Electric field in the ionization region
$(E/N)_{\mathrm{c}}$:	Critical reduced field strength
$(E/N)_{\mathrm{h}}$:	Reduced field strength at which the ion-neutral interaction potential becomes hard-sphere
e:	Elementary charge
F_i:	Force exerted on an atom i
g:	Relative velocity
j:	Ionic flux density
K:	Mobility coefficient
K_0:	Reduced mobility coefficient

$K_0(0)$: Reduced mobility under zero field conditions

k: First order rate constant for the desolvation process

k_1^-: Ion annihilation rate

k_B: Boltzmann's constant

k_{ij}^r: Spring constant

k_{ijk}^θ: Angle constant

L: Drift tube length

L_IR: Ionization region length

L_p: Laser penetration depth

l_D: Debye screening length

l_Diff: Diffusion length

m_G: Mass of the neutral gas molecule

m_i: Mass of an atom i

m_I: Ion mass

N: Neutral gas number density

$N_{\mathrm{V},i}$: Number density of the i^{th} ion

n: Number of atoms

n: Peak capacity

$\mathcal{n}$: Spatial number density of ions

$\mathcal{n}_0$: Initial ion concentration

n_i: Number of times an amino acid i appears in a peptide sequence

P: Pressure

P_0: Standard pressure. 101,325 Pa

p_i: Intrinsic size parameter for an amino acid i

$\mathcal{p}_i$: Probability of state i

q: Charge

R: Droplet radius

r: Distance between two atoms or charge centers

r_0: Ion cloud radius

r_{cut}: Cutoff radius for non-bonded interaction potentials

r_i: Atomic coordinates of i

r_{list}: Cutoff distance for neighbor lists

r_{m}: Distance at which a potential energy function reaches it minimum. Equilibrium distance.

s: Planar source density

T: Temperature

T_0: Standard temperature, 273.15 K

T_{E}: Elevated temperature for MD simulations, 1,443 K

T_{IR}: Temperature in the ionization region

T_{b}: Boiling temperature

T_{c}: Thermodynamic critical temperature

T_{s}: Spinodal temperature

t: Time

t_{d}: Drift time

t'_{d}: Apparent drift time

t_{diff}: Temporal FWHM of a Gaussian peak created by diffusion broadening

t_{DT}: Transit time in the drift tube

t_{g}: Gate pulse width

t_{IR}: Transit time in the ionization region

t_{SC}: Coulombic broadening

U: Mean internal energy difference

ΔU: Mean internal energy difference between two states i and j

V_n: Torsion angle potential barrier height

$V(r^N)$: Potential energy of the system containing N atoms

$v(r_1, \dots, r_n)$: Interaction potential for a group of n different atoms

$v_{\mathrm{a}}(\theta_{ijk})$: Harmonic bond angle potential for θ_{ijk}

$v_{\mathrm{b}}(r)$: Harmonic bond potential between atoms i and j

$v_{\mathrm{Coul}}(r)$: Coulomb potential between atoms i and j

v_{d}: Drift velocity

$v_{\mathrm{d}}^{n}(\phi_{ijkl})$: Periodic torsion potential for ϕ_{ijkl} with periodicity n

$v_{\mathrm{HS}}(r)$: Hard sphere potential as a function of the distance between the spheres

v_{IR}: Ion average velocity in the ionization region

$v_{\mathrm{LJ}}(r)$: Lennard-Jones potential between atoms i and j

$v_{\mathrm{Morse}}(r)$: Morse potential between atoms i and j

(x_i, y_i, z_i): Coordinates of the i^{th} atom

y: Coefficient dependent on the relative measurement accuracy

Z_i: Charge state of the i^{th} particle

z: Charge state

$\vec{z}$: Drift axis

Greek

α: Alpha function

$\langle\alpha\rangle$: Ion creation rate

α_{p}: Polarizability

β: Thermodynamic beta, $1/k_{\mathrm{B}}T$

$\beta(x, y, z, t)$: Source term

β_{E}: Thermodynamic beta at elevated temperature T_{E}

γ: Surface tension

ε_0: Vacuum permittivity

ε_i: Energy of state i

ε_{m}: Well depth for a potential energy function

ε_{r}: Relative permittivity of the medium

θ_{ijk}: Angle between two consecutive bonds

θ_{m}: Equilibrium angle

κ: Thermal diffusivity of the irradiated material

μ: Reduced mass

ξ_i:	Number of states in conformation i
ϖ:	Periodicity
σ:	Van der Waals diameter
σ_{g}:	Standard deviation of Gaussian peak
σ_{space}:	Spatial spreading of an ion peak arriving at the detector
σ_{time}:	Temporal spreading of an ion peak arriving at the detector
τ:	Peptide backbone N-C_α-C bond angle
τ:	Exponential decay time
τ_{ac}:	Time required for acoustic energy dissipation
τ_{P}:	Laser pulse duration
τ_{th}:	Time required for energy dissipation through thermal conduction
$\Phi(\varphi_1, \varphi_2, \varphi_3, b, r)$:	Scattering potential
Φ_{IQ}:	Ion-quadrupole interaction potential
ϕ:	Peptide backbone C_{n-1}-N-C_α-C dihedral angle
ϕ_{ijkl}:	Dihedral/torsion angle between planes ijk and jkl
ϕ_{s}:	Phase shift
$\varphi_1, \varphi_2, \varphi_3$:	Angles describing the collision geometry
X:	Scattering angle
χ:	Membership function
ψ:	Peptide backbone N-C_α-C-N_{n+1} dihedral angle
Ω_{D}:	Average collision cross-section
Ω_{exp}:	Experimental collision cross-section
Ω_{ISP}:	ISP-determined collision cross-section
Ω_{MD}:	Molecular dynamics determined collision cross-section
Ω'_{MD}:	Molecular dynamics determined collision cross-section (before correction)
Ω_{PA}:	CCS of an equivalent polyalanine peptide
ω:	Peptide backbone C_α-C-N_{n+1}-$\mathrm{C}_{\alpha_{n+1}}$ dihedral angle
ω_{h}:	FWHM of an IM peak

I. Introduction

Every living organism, whether large or small, can be seen simply as a macroscopic – and complex – molecular arrangement. All the wide range of molecules present in such biological organisms falls under the category of biomolecules. They are the basis of life and include proteins and peptides, carbohydrates, lipids, nucleic acids and various metabolites and intermediate assemblies. These molecules act for example as enzymes, antibodies, neurotransmitters, energy sources, information storage... They are all essential to the proper functioning of the organism. As a more general term, all of those molecules which are susceptible to interact with biological systems are biologically relevant molecules. Some examples include pesticides, herbicides, fungicides, antibiotics, neuroleptics and various other drugs. The modes of action of biologically relevant molecules and the ways in which they interact with an organism are varied, but their role is often dependent on their shape, and their shape is the result of their molecular structure and their surrounding environment. On the one hand, a powerful tool to study molecular structure and motion are computer simulations. They can help establish a link between macroscopic and microscopic properties, model fast to ultrafast processes, understand interactions at the molecular level, or explore conditions which are not experimentally available or attainable. They can as well bridge the gap between theory and experiment by comparing *in-silico* to experimental results.

On the other hand, experimental techniques such as mass spectrometry (MS) are employed for the routine analysis of biologically relevant molecules. MS separates ions through their mass-to-charge ratio m/z and is usually applied in synthesis control, proteomics and environmental studies, to name a few. Often, such studies require the analysis of complex mixtures of biologically relevant molecules, which is facilitated by coupling different techniques together ("hyphenation"). MS is often coupled to chromatographic techniques such as HPLC (high performance liquid chromatography) and GC (gas chromatography). It is frequently used in conjunction with ion mobility (IM) spectrometry as well, given that IM provides isomeric discrimination, which is something that MS alone cannot directly do. The first commercially available IM-MS device was the Synapt, introduced by the Waters corporation in 2006. It marked the rise in popularity of IM spectrometry for pharmaceutical, clinical and biomolecular applications [1]. As a standalone technique, IM spectrometry is commonly used for chemical warfare agent and explosive detection, as well as for drug detection. For this purpose, standalone IM spectrometers mostly use radioactive, corona discharge or photoionization sources. However, the analysis of sensitive compounds such as biomolecules, complexes and ionic aggregates requires a soft ionization technique in order to preserve molecular structure and avoid fragmentation. In certain cases, even the native conformation of biomolecules might be preserved. Electrospray ionization (ESI) [2,3] and matrix-assisted laser desorption and ionization (MALDI) [4,5] are ideally suited for this purpose and remain the most popular in MS and IM-MS for biological applications. ESI was already implemented in IM spectrometers in the late 1980s by the Hill group [6,7] but fewer than 50 publications on standalone ESI-IM spectrometry exist up to date [8]. MALDI-IM spectrometry experiments have also been carried out by the Bowers [9], Russel [10], Pawliszyn [11,12] and Hill [13] groups. Although both ionization techniques are soft,

strong contrasts exist between them. While ESI produces multiply charged ions, MALDI produces mostly singly charged ones. Where MALDI requires a time-consuming co-crystallization step, ESI enables the direct analysis of liquid samples and solutions. A third option, bridging the gap between ESI and classical MALDI, is IR-MALDI (Infrared matrix-assisted laser dispersion ionization) [14], also known as LILBID (Laser-induced liquid beam/bead ionization/desorption) [15,16]. It produces mostly low-charge states like classic MALDI but, by using a liquid matrix, avoids the co-crystallization step. Furthermore, the liquid matrix makes it compatible with the direct analysis of solutions, like ESI. This makes it a very suitable technique for the analysis of complex mixtures of biologically relevant molecules: preservation of weak bonds, easier peak attribution due to simplified charge distributions and direct analysis of aqueous solutions, the native environment of biomolecules. Thus, the combination of IR-MALDI with IM spectrometry, complemented by molecular dynamics simulations, results in a powerful characterization technique for biomolecules.

While IR-MALDI has been successfully applied as a soft ionization technique for large molecular assemblies and several examples of applications exist [17–20], only a few studies have been carried out regarding its mechanism. The aim of this work was to assemble, characterize and optimize an IR-MALDI-IM spectrometer for the study of the IR-MALDI dispersion process and for its use in the analysis of biomolecules and various biologically relevant substances. Molecular dynamics simulations of peptides in the gas phase were also integrated into a novel collision cross-section calculation method which bridged the gap to the experimental results.

In the following work, the IR-MALDI technique will first be placed back into the more general MALDI context. Information from laser ablation studies as well as specific IR-MALDI studies will then be put together in order to provide a cohesive overview of the technique, its development and what is known regarding its mechanism. Theoretical considerations regarding molecular simulation through atomic interaction potentials will also be discussed, followed by the theory of ion mobility spectrometry at low fields and the appropriate ion-neutral interaction potential models. Finally, a quick summary of the factors determining high-field ion mobilities will be given. It will then be discussed how IR-MALDI and IM spectrometry were used together in this project to gain insights into the dispersion/ionization mechanism of the ionization technique. It will then be shown that IR-MALDI-IMS was also developed and optimized into a robust analytical method for biologically relevant molecules, both at atmospheric and at reduced pressure. The latter can help shed some light on polyatomic ion behavior at high field strengths, which are conditions usually encountered for example in field asymmetric ion mobility (FAIMS). Finally, it will also be shown how molecular dynamics can complement the purely experimental results in order to better understand peptide structures. A new approach to IM collision cross-section estimation based on thermodynamic reweighting of high temperature MD simulations will be presented and then applied to peptides analyzed with IR-MALDI.

II. Theory

II.1 IR-MALDI

II.1.1 Development of IR-MALDI

II.1.1.1 Traditional MALDI

In typical matrix-assisted laser desorption and ionization (MALDI), the target analyte is co-crystallized with a matrix on a given substrate, followed by laser irradiation, usually with ultraviolet (UV) light. A liquid matrix can also be mixed with an analyte solution and then deposited on a plate. The choice of the matrix will depend on the analyte and the application, but some of the most commonly used matrices in UV-MALDI are CHCA (α-cyano-4-hydroxycinnamic acid), SA (sinapic acid) and DHB (2,5-dihydroxybenzoic acid). If an IR (infrared) laser is used, carboxylic acids, alcohols, indoles, amines and water can be used as matrices. The matrix absorbs the laser radiation and transforms it into heat either through electronic (UV) or vibrational (IR) excitation. This leads to material ejection without degradation of the analyte material. According to the laser fluence, the material ejection can be seen as desorption or ablation. In the desorption regime, mostly gaseous matrix and analyte are ejected. In the ablation regime, clusters, droplets and aggregates are produced. If the laser pulse is short enough, larger chunks of material can be expelled (spallation) through stress confinement. While useful for certain laser ablation applications, spallation does not commonly occur in typical MALDI experiments [21–23]. Following material ejection, the ionization in MALDI takes place in a two-step process. Primary ion formation, the mechanism of which is still subject to debate, and secondary ion formation. Secondary ion formation in a dense plume has been studied mostly for UV-MALDI but similar results could be expected in a dense IR-MALDI plume as well [23].

II.1.1.2 Laser and matrix

The role of the matrix is to bring the analyte into the gas phase, and assist with the ionization process. Matrix and laser wavelength must be chosen together according to the application, as the matrix should usually have a larger absorption coefficient than the analyte at a given wavelength. The typical UV matrices contain a chromophore which absorb the incident radiation by means of electronic transitions in the compound. On the other hand, typical IR matrices absorb vibrational energy, which results in lower internal energy deposition and translates into a softer ionization process which preserves non-covalent bonds [14,24–28]. However, due to the cost and lack of versatility IR lasers available in the past, UV-MALDI has been thus far preferred in commercial mass spectrometers [23,29]. This constraint is progressively being lifted thanks to the wide array of mid-infrared laser technologies which have recently become available [30,31]. Gas lasers, chemical lasers, solid state lasers, semiconductor lasers, free electron lasers, fiber lasers and optical parametric oscillators (OPO) can all be used in the mid-IR range. Thus, a wide range of wavelengths can be obtained with the various laser systems. For example, solid-state Er:YAG and Er:YSGG can operate in the 3 µm range and CO_2 lasers in the 10 µm range, while optical parametric oscillator (OPOs) and free electron lasers emit radiation of a tunable wavelength. It is then possible to excite different functional groups: O–H, N–H and C–H stretch vibrations, as well as weaker

hydrogen bonded modes of these groups [28] are excited around the 3 µm range, C=O stretch vibrations around 5.5 µm and C–O and C–N stretching and O–H bending in the 10 µm range.

II.1.1.3 Towards a liquid matrix

The co-crystallization step between matrix and analyte in MALDI can be a laborious task. Furthermore, it can lead to the formation of "hot spots", which are the result of analyte/matrix heterogeneities and result in low reproducibility between laser shots [32]. This has led to renewed interest in liquid matrices, which have the advantage of directly using a solution of the analyte in the matrix, saving time and guaranteeing homogeneity. Furthermore, non-covalently bound complexes which might dissociate due to the relatively harsh conditions during drying and co-crystallization are also preserved [33]. Finally, liquid matrices are intrinsically compatible with liquid phase separation techniques and constitute self-renewing target surfaces. The reason solid matrices are usually preferred over liquid ones is due to their stability in vacuum, which has been often necessary in mass spectrometry. Recently, ionic liquid matrices [32,34,35] have been developed for UV-MALDI. They are nonmolecular salts with a melting point below 100 °C, which are made up of traditional MALDI matrices like CHCA, DHB or SA and an organic base such as tributylamine, pyridine or 1-methylimidazole. They do not require a co-crystallization step and result in homogeneous solutions which have low vapor pressures, making them suitable for vacuum. Ionic liquid matrices (ILMs) also include the necessary UV-chromophores of traditional matrices and don't require any additional compounds for desorption and ionization. ILMs are not, however, actual liquid matrices, as most samples are either solid or vitreous when spotted on a MALDI target [32]. Furthermore, their preparation, though under softer conditions than for traditional matrices, remains time-consuming.

There are however some highly viscous liquids which can be directly used as matrices for MALDI under vacuum conditions. In UV-MALDI, 3-nitrobenzyl alcohol [36,37] has been used, and in IR-MALDI, glycerol [38,39]. Some mixed [40,41] and binary [5,42–44] systems have been used as well, with interesting results. In both cases absorbers in the UV-vis range were either dissolved or mixed with a viscous solvent which absorbs in a different range (UV or IR), resulting in a mono or bi-phasic matrix solution. The resulting matrix should be able to enable the MALDI process at either the solvent or the additional absorber's wavelength range.

II.1.1.4 Liquid matrices for IR-MALDI of biological compounds

In the case of IR-MALDI, glycerol was used as a matrix because it has one of the lowest vapor pressures amongst common liquids [45], which translates into low volatility and higher stability in vacuum. For the same reason water ice was also used in early studies. The advantage of water is that it is the native medium for biological molecules such as proteins and peptides. Furthermore, it has its absorption maximum in the infrared at 2.94 µm [46], which would mean a softer ionization process when compared to UV radiation. The problem with ice was lower sensitivity, low signal-to-noise ratio and limited reproducibility [47]. The advent of Faubel's liquid jet [48] enabled the introduction of liquids with higher volatilities into vacuum in the form of a

supercooled filament. Brutschy's group were the first to use it as an ionization technique. They used alcoholic solutions in combination with a CO_2 laser [15,16] and called it LILBID, for laser-induced liquid beam ionization/desorption. Subsequently, they used the liquid beam technique with aqueous solutions and a Nd:YAG OPO [49] as well. Further development of LILBID made use of liquid droplets on demand, reducing sample consumption and expanding the acronym to laser-induced liquid beam/bead ionization/desorption [20]. The technique was also established in the Abel group [14], where higher resolution was achieved by designing a new trap for the liquid jet. There, the technique was referred to as liquid beam (laser) desorption as well as infrared free-liquid matrix-assisted laser dispersion ionization (IR-FL-MALDI). Both groups have since then reported numerous applications of this technique in combination with MS, detecting non-covalently bound complexes, using it for (bio)kinetics studies, polymer characterization, analysis of complex mixtures, HPLC coupling and determination of the oxidation state of biomolecules in solution, to name a few [50].

II.1.1.5 Atmospheric pressure

The development of atmospheric pressure (AP) ionization sources for mass spectrometry also took place for liquid MALDI, both for UV [51–53] and IR sources [54–56]. This means that no particular requirements for the solvent's compatibility with vacuum were necessary anymore, be it restricting the liquid matrix to a few viscous substances or using a cryotrap in the case of the microbeam. In fact, a capillary with a droplet of a matrix/analyte solution at its tip is all that is needed [57]. This opens up simple on-line coupling to liquid chromatography, although for higher flow rates in HPLC the liquid beam technique is better suited, as the Abel group reported [58]. They used their existent nanoESI equipment, operating it at high flow rates and effectively expanding its usage to IR-MALDI. Before these advancements, only electrospray ionization had been used to analyze aqueous solutions at atmospheric pressure. Now, a range of hybrid ESI/MALDI techniques have been explored. In laser spray [59,60], an infrared laser was focused on the tip of an ESI capillary. In ELDI (electrospray-assisted laser desorption ionization), the material is ablated by a UV laser without the need for a matrix and ionized by an electrospray aerosol [61]. LAESI (laser ablation electrospray ionization) and IR-LADESI (infrared laser-assisted desorption electrospray ionization) use the same principle as ELDI but with an IR laser [62,63]. MALDESI (matrix-assisted laser desorption electrospray ionization) is also similar to these techniques, with the difference that it applies a positive dc potential to the sample plate. It also uses a matrix for assisted desorption, as opposed to ELDI [64,65]. LEMS (laser electrospray mass spectrometry) uses a UV femtosecond laser and applies a dc potential of opposite polarity to MALDESI [66]. These techniques are of particular interest for the direct analysis of biological tissue while still obtaining highly charged states as in ESI. A wide range of techniques using laser desorption, ablation or even acoustic desorption, followed by other atmospheric pressure ionization methods complements these MALDI/ESI hybrid approaches [67].

II.1.2 Mechanism

II.1.2.1 General principle

The actual process in IR-MALDI will depend on the matrix material properties as well as on the laser parameters used. More specifically, it will depend on thermal and stress confinement[1]. The ablation mechanism in water has been modelled through molecular dynamics and has been show to proceed by steps [68,69]. An initial vaporization step occurs, where less than 1 % of the deposited energy is used. Then, a phenomenon known as phase explosion sets in: the material starts to expand due to laser heating until it eventually explodes. The expanding plume is initially a mixture of sublimated molecules and liquid matter, which then goes through a foam-like transition state and finally decomposes into clusters and droplets. One major consequence of the phase explosion is the rapid cooling of the expanding plume. Extreme temperature and pressure conditions are reached during the process. Aqueous solutions can even be brought into the supercritical state, but evaporative cooling and expansion stabilize the biomolecules, which are kept intact. Furthermore, the larger the biomolecule, the more internal degrees of freedom it has, which prevents it from fragmenting – or dissociating in the case of complexes – before reaching the detector [70], keeping in line with the perceived softness of the IR-MALDI technique. This is analogous to classic solid UV-MALDI, where both simulations [71,72] and experiments yield peak sample temperatures between 500 and 1,200 K as it's initially ablated from the material surface. However, rapid cooling due to vaporization and subsequent plume expansion then takes over.

II.1.2.2 Thermal confinement

If the laser pulse τ_{p} is shorter than the time required to dissipate the absorbed energy by thermal conduction τ_{th}, the condition for thermal confinement is fulfilled. The laser penetration depth L_{p} and the thermal diffusivity of the irradiated material κ are key parameters according to $\tau_{\mathrm{th}} = L_{\mathrm{p}}^2/\kappa$. At a wavelength of 2.94 µm, $L_{\mathrm{p}} = 1.5$ µm for water and $\tau_{\mathrm{th}} =$ 13 µs [46,73]. This means that the ablation process of water at 2.94 µm with nanosecond pulsed lasers always takes place under thermal confinement conditions.

According to Miotello and Kelly, three kinds of thermal processes may lead to the ejection of material from the surface of a condensed-phase material after irradiation by a laser: vaporization, normal boiling and explosive boiling, which they use interchangeably with phase explosion [74]. Normal vaporization can occur under any conditions, but requires either long energy deposition times or high fluences, leading to temperatures higher than the boiling temperature T_{b} of the material. The vaporization is also enhanced if the temperature is raised rapidly, even if T_{b} is not reached, as the liquid surface ceases to be in equilibrium with the surrounding vapor. Vaporization then occurs until the liquid surface and the vapor have reached a temperature and pressure equilibrium again [75]. In normal boiling, bubbles form through heterogeneous nucleation at a temperature T only minimally higher than T_{b}. After the material is kept long enough at $T > T_{\mathrm{b}}$, the bubbles may diffuse enough to escape the liquid surface. This means that normal boiling is

[1] Confinement takes place when the energy deposition is faster than the energy dissipation and as such the response of the system depends only on the total deposited energy and not on the deposition time

impossible for pure water and nanosecond laser pulses but can occur with microsecond pulses [76].

Finally, if superheating occurs and the temperature exceeds that of the liquid spinodal at the corresponding pressure, phase explosion occurs by homogeneous nucleation and spinodal decomposition[2]. Figure 1 (left) illustrates this phenomenon. A liquid initially at SATP (standard atmospheric temperature and pressure) conditions – point (1) – is heated under isobaric conditions until T_{b}, corresponding to point (2) on the binodal curve. Homogeneous nucleation occurs from the metastable superheated state, from point (2) to point (3), while spinodal decomposition implies spontaneous phase separation from an unstable state after the temperature exceeds the spinodal temperature T_s at point (3). The system relaxes back into equilibrium by separating into saturated liquid – point (4') – and vapor at pressures close to that of saturated liquid at the corresponding T_s – point (4). For water at atmospheric pressure, this corresponds to a 90-fold increase in pressure up to 9.2 MPa at $T_s \approx 305$ °C [75]. The system then slowly relaxes back to point 2. Vogel, Apitz and Venugopalan distinguish between this phase explosion pathway and an intermediate process between normal boiling and the (1) → (3) → (4) pathway, which they term explosive boiling.

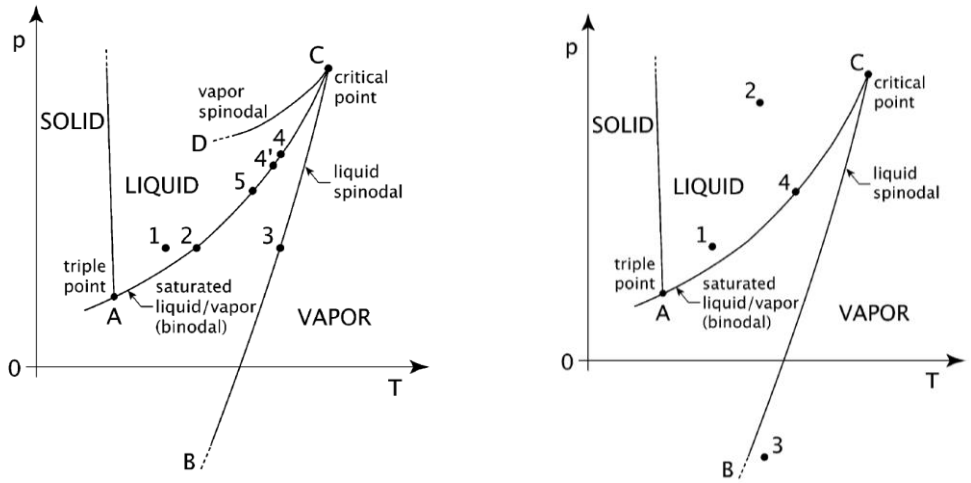

Figure 1: Left: Pressure vs temperature projection of the thermodynamic phase diagram including the spinodal curve. Specific states of interest are (1) ambient temperature and pressure, (2) boiling temperature under ambient conditions, (3) spinodal temperature at ambient pressure, and (4) saturated conditions corresponding to the ambient spinodal temperature. Right: Path taken through the p vs T projection of the thermodynamic phase diagram for a temperature rise above 100 °C under stress confinement conditions. The transition 1 → 2 corresponds to the heating phase that is coupled with the generation of compressive stress. The transition 2 → 3 corresponds to the passage of the tensile stress wave that leads to a crossing of the spinodal limit, resulting in phase separation. After the passage of the stress wave, the system reaches point 4, that corresponds to explosive boiling into the large number of bubbles produced shortly before. Both reprinted with permission from [75]*, © 2003, American Chemical Society*

For homogeneous heating, if the energy deposition is fast enough, the irradiated volume does not have time to expand, such that an isochoric heating process can be considered, quickly leading to the supercritical state. This can be visualized in the 3D phase diagram of water in figure 2.

[2] The rapid demixing of one phase into two separate, coexisting phases

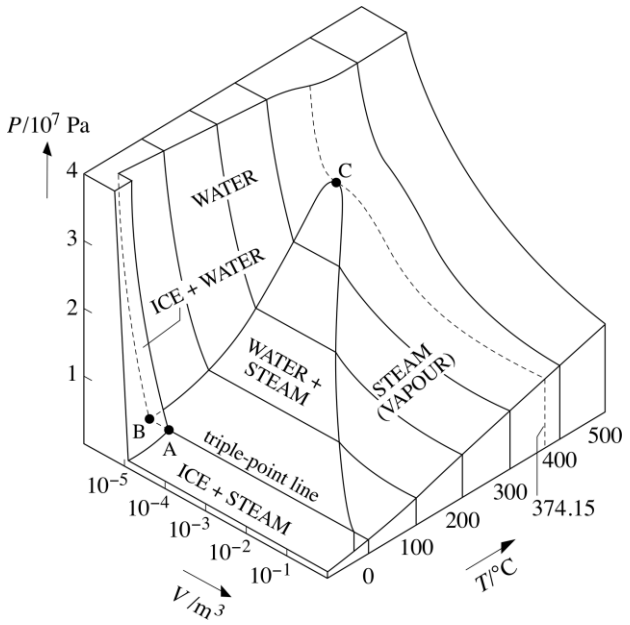

Figure 2: Pressure-Volume-Temperature surface for 1 mol H_2O (© 1996 Open University [77]*)*

II.1.2.3 Stress confinement

The laser-induced heating of the water volume leads to the creation of thermoelastic stress with both a compressive (higher pressure) and a tensile[3] (lower pressure) component, which can reach very high amplitudes under stress confinement [78]. The conditions for stress confinement are that τ_{p} be shorter than the time constant for acoustic energy dissipation, $\tau_{\mathrm{ac}} = L_{\mathrm{p}}/c_{\mathrm{a}}$, where c_{a} is the speed of sound in the medium. For water irradiated at 2.94 µm, $\tau_{\mathrm{ac}} \sim 1$ ns, which means that with an 8 ns laser pulse, thermomechanical stress propagation will have an influence on the ablation process. Microcavitation due to stress confinement has in fact been found to play an important role with liquids, unlike with solid matrices [68].

Cavitation is the formation of bubbles through tensile stress under isothermal conditions, while *boiling* is due to heating under isobaric conditions. However, when heating under stress confinement conditions occurs, the distinction between cavitation and boiling becomes hard to make, as both heating and tensile stress contribute to bubble formation. Consider Figure 1 (right): from SATP (1), heating and compressive stress bring the liquid to state (2), but the propagation of the resulting stress wave with alternating compressive and tensile components progressively shifts the system towards (3). A negative thermoelastic pressure wave can incur in bubble formation and/or growth at an accelerated rate after the binodal is crossed, leading to explosive boiling at (3) once the system is past the spinodal. Once the stress wave has passed, the system relaxes to point (4), on the binodal, with two separated phases. Thus, phase separation can occur at lower temperatures. Effectively, stress confinement can lower the ablation threshold and lead to a more efficient ablation.

[3] Tension can be seen as a negative compression and vice-versa

II.1.2.4 Recoil

The late stage of material ejection is driven by ablation-induced recoil stress and takes place at longer timescales than phase explosion. It lasts considerably longer as well (in the sub-second range in the case of water) [79]. The initial plume of ejected material is driven by an accelerating force, leading the aerosol away from the ablation spot but generating an equally strong recoil force. The recoil force leads to a purely compressive stress [78], which can propagate through the water at values of several hundred MPa [76,79]. Work by Klein et al. indicates that the higher the energy which is applied, the stronger the recoil stress will be [80]. The high compressive stress can even momentarily suppress the phase explosion process by moving to high pressure regions in the P vs T phase diagram. For long enough laser pulses, energy deposition into the pressurized system may then continue and lead it towards the supercritical state [79]. Due to the liquid's incompressibility, the only way for the layer under stress to be displaced is radially, where it collides with further incompressible liquid and is extruded upwards as a cylinder. The effect is similar as the upward water extrusion (commonly referred to as "splash") generated by the compressive stress following the impact of a projectile, say a rock, on a body of water. The cylinder then collapses into a cone and merges into an upwards jet flow due in part to surface tension and to the under pressure of the cavity below. The last stage is disintegration of the jet due to hydrodynamic instabilities. The droplets produced by this stage are significantly larger than the fine initially produced aerosol [75,79].

II.1.2.5 Plume dynamics

The initial material ejection from a liquid surface consists purely of vapor, as the deposited volumetric energy density in the top layers is higher than the vaporization enthalpy of water at SATP conditions ($\varepsilon = 2.59$ kJ·cm^{-3}). Then, the phase explosion of the superheated water layer begins and the composition of the plume changes to a mixture of vapor and liquid droplets, which increase in size as time progresses. This creates a first vaporization shockwave against ambient air, which propagates at speeds of 1,500 m·s^{-1} and is accelerated to 2,000 – 4,000 m·s^{-1} with the onset of phase explosion. The compressive stress wave in water begins to propagate approximately at the same time as the first shockwave phase but precedes the acceleration phase. Apitz and Vogel reported a speed of 2,300 m·s^{-1} corresponding to 930 MPa for the water shockwave. The speed in the condensed phase actually depends on the water content. The reported velocity of the ejected water droplets, ejected with the second, phase-explosion induced shockwave, is around 280 m·s^{-1} [75,76,79]. At low fluences, close to the ablation threshold, the plume rises orthogonally to the ablation surface and acquires a mushroom shape due to interactions with the ambient air, with a stem that is thinner than the ablation spot. The plume expansion creates an elevated pressure in the ambient gas due to pile-up at the shock front. This is also called the "snowplow" effect. At high fluences, shielding through scattering and absorption by the ablation plume of the incident radiation slow down the process by limiting the amount of energy reaching the surface of the liquid. The plume remains denser in the presence of a surrounding gas (as opposed to vacuum conditions) and thus plume reactions can take place.

II.1.3 Ionization in IR-MALDI

II.1.3.1 Supercritical phase expansion and incomplete ion recombination

The Brutschy and Abel groups [14–16] have previously proposed supercritical phase expansion (SPE) as the main mechanism for IR-MALDI using liquid microbeams in vacuum. They propose a homogeneous heating that results in a supercritical phase which then isotropically expands. During this expansion, pre-formed aggregates and ions are isolated according to an incomplete ion recombination (IIR) model. The density and the dielectric constant of the supercritical fluid decrease during the early stages of phase expansion, which reduces shielding and facilitates ion recombination. The rate of recombination depends on the distance between oppositely charged ions. In solution, the distance between the recombining ions can be approximated by the Debye screening length, l_{D}, which can also give an idea about the rate of recombination in the gas phase [81].

$$l_{\mathrm{D}} = \left(\frac{e^2}{\varepsilon_0 \varepsilon_{\mathrm{r}} k_{\mathrm{B}} T} \sum_i Z_i^2 N_{\mathrm{V},i} \right)^{-\frac{1}{2}} \quad (1)$$

Where e is the elementary charge, ε_0 the vacuum permittivity, ε_{r} the relative permittivity of the medium (also called dielectric constant), k_{B} the Boltzmann constant, Z_i the charge state of the i^{th} ion, $N_{\mathrm{V},i}$ the number density of the i^{th} ion in solution. The IIR model can be seen as an analog to the lucky survivor model, where those ions which are sufficiently far away from their now non-shielded counter ions are detected as the “lucky survivors”. Since the Debye screening length depends on the charge state of the ions, Z_i, those with low charges are more likely to survive. Coulomb attraction discharges the rest. Although this model reasonably accounts for the saturation of the ion signal at higher concentrations, it fails to explain its linear response with regard to the concentration over several orders of magnitude. The dependence on the number density of ions in solution should mean that the ion signal decreases with increasing concentration. Furthermore, stroboscopic experiments by the Abel group show that for a liquid microbeam, rather than homogenous supercritical phase expansion, the liquid is dispersed into droplets. Even if an SPE did take place, recondensation would result in the formation of droplets and dispersed liquid [50]. The SPE model could also be seen as a limit case of infinite dispersion in the liquid dispersion model, and different experimental conditions could explain different results and thus different models.

II.1.3.2 Liquid dispersion in microbeams

The liquid dispersion mechanism proposed for the microbeam setup in vacuum is a two-step process. First, a non-thermal desorption stage takes place due to the propagation of a shockwave throughout the microbeam. This shockwave arises from a temperature gradient at the laser impact side of the microbeam and leads to the detachment of a layer of liquid on the backside [82]. Second, thermal volume expansion/phase explosion follows. At lower energies, the initial shockwave desorption step is not seen, only the thermal phase [81]. Takamizawa et al. also observed an acoustic wave propagating at the surface of their microbeam at atmospheric

pressure, leading to heating and explosive boiling at the front side, followed by the back. Furthermore, they observed an increase in droplet size due to recondensation in the microsecond scale after the initial explosive boiling phase [83]. In the observations reported by Apitz and Vogel for an infinitely large volume of water, shockwaves propagate both in air and water at higher fluences [79]. The model for the microbeam could then perhaps be seen as the specific case for a free liquid of finite thickness in or close to the stress confinement regime. In addition, under certain conditions, it has been shown that the liquid microbeam can be transferred into a supercritical state with extreme pressures from 20 to 35 kbar and temperatures from 1,500 to 2,000 K [70].

II.1.3.3 Charge production

The microbeam studies of IR-MALDI in vacuum are interesting since the lack of bath gas implies that no additional thermal energy could be transferred to the droplets in order to evaporate the solvent. In other words, droplets generated by liquid dispersion evaporated just through their own internal energy. This could only occur for the smallest droplets produced, as most of them are too large to evaporate completely in vacuum. The probability of obtaining charged droplets depends on the amount of droplets produced which are smaller than l_{D}, which in turn means that the probability of having two or more charges in the droplet is smaller, leading to low charged states. The mechanism itself is thought to be through protonation in solution. This is due to the fact that no apparent correlation between signal and analyte gas phase basicity is observed in mass spectrometry, as well as the fact that the ion product of water is higher under high temperature and density conditions than at NTP. The latter makes protons more readily available to fix on the basic sites of the analyte molecule [81]. The evaporation of the solvent then results in a charged desolvated molecule, meaning that the charges are generated purely through the dispersion mechanism rather than through an active ionization [4] mechanism. The resulting charge distribution follows a Poisson statistical distribution for low concentrations, with Coulomb interaction decreasing ion yields at intermediate concentrations and recombination being responsible for a sharp decrease in intensity at very high concentrations [84]. Work by Komatsu et al. support the liquid dispersion mechanism: they observed that the addition of salt in increasing concentrations to a lysozyme solution also resulted in the suppression of the analyte ion signal at high NaCl concentrations and that the ion abundance in the gas phase linearly depends on the IR laser power, excluding multiphoton processes in the ionization [85].

II.1.3.4 Ion release

In electrospray ionization theory, charged droplets undergo size reduction due to solvent evaporation in a heated bath gas, followed by fission when the Rayleigh limit is attained (equation 2), at which the surface tension γ and Coulombic repulsion are balanced out. R is the droplet radius and q its charge.

[4] The generation of an ion by loss or gain of an electron or through chemical reactions

$$q = 8\pi\sqrt{\varepsilon_0 \gamma R^3} \quad (2)$$

Solvent composition and temperature are determining factors in this step: a more volatile solvent will evaporate more easily and one with lower volatility will require a higher temperature [86,87]. The following ion ejection can take place through the ion evaporation model (IEM) [88,89], the charge residue model (CRM) [2,90] or the chain ejection model (CEM) [91,92]. It is generally accepted that the IEM explains the release of small ions the CRM of large globular analytes and the CEM of unfolded non polar polymer chains [87].

The liquid dispersion model echoes the charge residue model in that as the solvent progressively evaporates, most of the charges in the droplet are transferred to the molecule until only the naked ion in the gas phase is left. The authors of the liquid dispersion model state that the direct ion evaporation can be ruled out due to large solvation energies [50,81,93], but they examine only large biological complexes, mostly in vacuum. It is unclear whether CEM or IEM might play a role for the latter stage of ion release after laser dispersion at atmospheric pressure as well. IEM is the model that has been suggested for small cationic bioorganic species such as drug molecules and metabolites [94], which is the range of molecules that this work focuses on.

II.2 Molecular dynamics

II.2.1 Solving Newton's equations of motion

Molecular simulations are an important tool in order to model the world around us. For a given thermodynamic ensemble, they can estimate macroscopic properties of the system based on the statistical distribution of its microscopic states. There are two main families of simulation techniques, which are Monte Carlo (MC) and molecular dynamics (MD) [95]. The first rely on random sampling applied to discrete systems where events occur according to a law of probability. The second rely on the numerical resolution of the classical equations of motion. Hybrid MD-MC approaches exist as well.

The objective of the simulation is not to exactly reproduce nature, which would be impossible, but to accurately sample conformations from the distribution in phase space[5] using statistics. Since molecular dynamics are concerned with molecular motion, both intra- and intermolecular processes can be modeled, such as for example molecular bond movement, receptor binding, protein folding and many more. However, the direct use of molecular dynamics would give rise to a microcanonical ensemble (NVE, i.e. constant number, constant volume and constant energy), so a thermostat is required to fix the temperature rather than the energy. This gives rise to a canonical ensemble (NVT) where the most likely distribution of states is the Boltzmann distribution, given as

$$p_i = \frac{e^{-\varepsilon_i / k_B T}}{\sum_{j=1}^{N} e^{-\varepsilon_j / k_B T}}, \quad (3)$$

[5] The ensemble containing all possible states of the system

where p_i and ε_i are the probability and energy of state i in a distribution with N accessible states.

This way, both kinetic and thermodynamic studies can be carried out with MD. It is also very often used to study conformational transitions, as it models the change in the position of atoms over time (their velocities). This makes Newton's second law of motion the basis for MD (equation 4):

$$F_i = m_i \frac{\partial^2 r_i}{\partial t^2} \tag{4}$$

F_i is the force exerted on an atom i, m_i its mass, r_i its coordinates and t the time. The force can also be written as a function of the partial derivative of the potential energy of the system $V(r^N)$ with respect to the atomic coordinates, as shown in equation 5.

$$F_i = -\frac{\partial V(r^N)}{\partial r_i} \tag{5}$$

However, since the time step of the simulations has to be small enough to be on the order of magnitude of the considered atomic processes (femtoseconds) and the force depends on the coordinates of all of the atoms in the simulation, the computational requirements can quickly become very high for larger systems and simulation times. This is why in practice it is more convenient to express the potential energy $V(r^N)$, from which the forces are derived, in terms of pair, three-body or four-body interactions between the atoms, as shown in equation 6. The first term, $v(r_i)$, represents the effect of an external potential or of the container walls. In the periodic boundary simulation of a system under no external influences, it is neglected [95,96].

$$V(r^N) = \sum_i v(r_i) + \sum_i \sum_{j>i} v(r_i, r_j) + \sum_i \sum_{j>i} \sum_{k>j} v(r_i, r_j, r_k) + \cdots \tag{6}$$

There are two sorts of interactions which are considered: bonded and non-bonded interactions, corresponding to bond vibrations, angle vibrations and torsion potentials for the first one and van der Waals and electrostatic interactions for the second. Various potential expressions exist for each of these cases, the exact expression and decomposition will however depend on the force field that is used. This is the collection of potential energy functions and parameters that is used in simulations and it will depend on the desired application. The parametrization of these force fields is done semi-empirically by fitting the potential equations parameters to experimental results with the help of quantum chemical calculations. Spectroscopic data is used for intramolecular interactions and, when it exists, for intermolecular interactions as well. However, most of the time macroscopic physicochemical properties of the liquid or the solid are employed.

II.2.2 Non-bonded interactions

II.2.2.1 Lennard-Jones interaction

Equation 7 shows the most commonly used non-bonded interaction potential form, which is derived from the potential first proposed by Sir John Edward Lennard-Jones [97]. It is a pair interaction, composed of a short range repulsive term in r^{-12} and a term in r^{-6} related to intermediate range attraction through the van der Waals force, as illustrated in Figure 3. The

different parameters are r, the distance between the two atoms i and j, ε_{m}, the corresponding potential well depth and σ, the van der Waals diameter, i.e. the distance between the two atom nuclei at their closest possible approach. By definition, $r_{\mathrm{m}} = \sqrt[6]{2}\sigma$ for the Lennard-Jones interaction. It is the equilibrium distance, i.e. the distance at which the potential function reaches its minimum, so that $v_{\mathrm{LJ}}(r) = -\varepsilon_{\mathrm{m}}$.

$$v_{\mathrm{LJ}}(r) = 4\varepsilon_{\mathrm{m}}\left[\left(\frac{\sigma}{r}\right)^{12} - \left(\frac{\sigma}{r}\right)^{6}\right] = \varepsilon_{\mathrm{m}}\left[\left(\frac{r_{\mathrm{m}}}{r}\right)^{12} - 2\left(\frac{r_{\mathrm{m}}}{r}\right)^{6}\right] \tag{7}$$

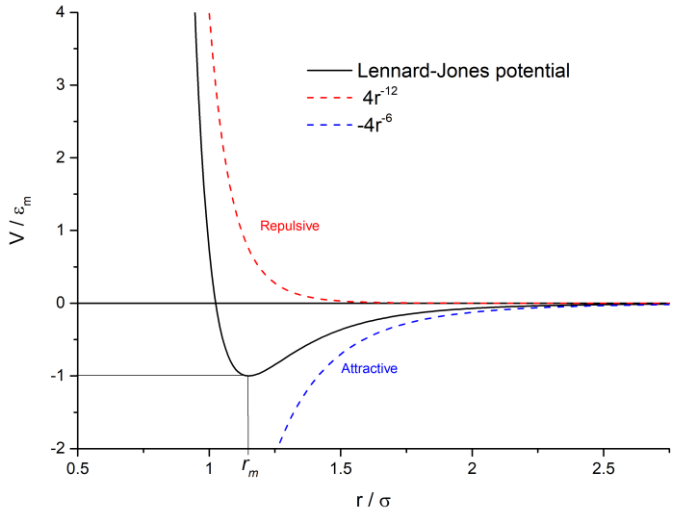

Figure 3: Lennard-Jones potential with repulsive and attractive contributions

II.2.2.2 Coulomb interaction

In the case of electrostatic charges, the resulting long range pair interaction is described by the Coulomb potential as presented in equation 8. The algebraic charge states Z_i and Z_j determine whether the force will be attractive or repulsive, depending on their respective signs.

$$v_{\mathrm{Coul}}(r) = \frac{Z_i Z_j e^2}{4\pi\varepsilon_r\varepsilon_0 r} \tag{8}$$

These interactions are useful in the case of, for example, ionic molecules or for the determination of hydrogen bonds using the partial charges of the atoms.

II.2.2.3 Cut-off and neighbor lists

In practice, non-bonded interactions are not calculated for every single atom pair, given that at long distance the interactions are already too weak to be significant. A cutoff distance r_{cut} can be defined for a non-bonded interaction potential, where if the distance r between two atoms is above r_{cut}, the potential value is set to 0. This is also known as a truncated potential. However, this would still mean calculating every interatomic distance at every time step, which can still become computationally expensive. For this reason, Verlet suggested using lists of nearby atoms

instead [98]. These lists are created at the beginning of the simulation for every atom and are only updated when needed. The method is based on the cutoff distance r_{cut} as well, but an additional distance r_{list} such that $r_{\mathrm{list}} > r_{\mathrm{cut}}$ is also defined. For each atom, all atoms within a distance of r_{list} are added to its list of neighbors and only the atoms in the list of neighbors are checked for interactions. Since the atoms move around during the simulation, the list will need to be reconstructed before non-listed atoms come within interaction range, which can be done by keeping track of atom displacement since the last update. For larger systems with over a thousand atoms, the simulation space can be divided into cells, into which all the atoms are sorted at every time step. For an atom in a given cell, only all other atoms in the same cell as well as all immediately adjacent cells are checked for interaction [95].

The introduction of r_{cut} implies a discontinuity in the potential function, which according to equation 5 poses a problem for the determination of the force at that point. In order to assure continuity, different strategies exist. Specifically for the Coulomb interaction, the assumption can be made that the dielectric environment after r_{cut} is constant, thus modifying the potential expression. This is called a reaction field. For non-bonded interactions in general, the "cut and shift" as well as "tapering" strategies also exist [99]. The potential is either shifted by a bit so that its value is zero at r_{cut} or multiplied by a smooth taper function that goes to zero between a given radius r_{taper} and r_{cut}, such that $r_{\mathrm{taper}} < r_{\mathrm{cut}}$.

II.2.3 Bonded interactions

The intramolecular bonded interactions will include pair, three-body and four-body potentials. The first case will describe a bond vibration, the second the angle between two bonds and the third the angle between two planes. These are illustrated in Figure 4.

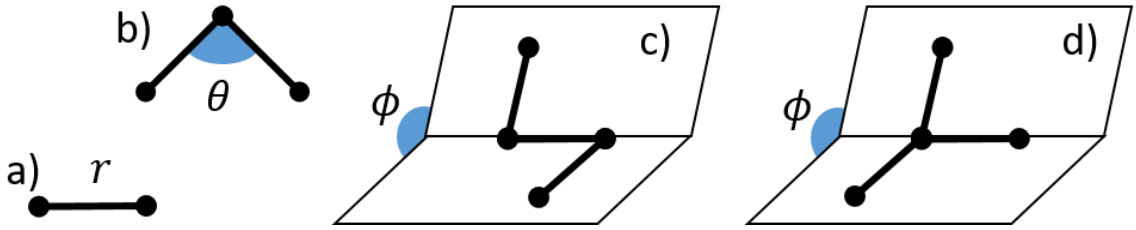

Figure 4: Bonded interactions. a) Bond stretching with the interatomic distance r b) angle bending with the bond angle θ, c) proper dihedral and d) improper dihedral angle with ϕ the dihedral angle

II.2.3.1 Pair interaction

The stretching of a covalent bond between two atoms can be described by either a harmonic potential or as a Morse oscillator. The first, in equation 9 is a simple, computationally inexpensive model and is used for systems close to the energy minimum [100]. The second is useful for modelling bond breaking, since the force is annulled at an infinite distance, as shown in Figure 5. This is due to the exponential term in equation 10, where k_{ij}^{r} is the spring constant and $a = \sqrt{\left(k_{ij}^{r}/2\varepsilon_{\mathrm{m}}\right)}$. The Morse potential can be used for systems in equilibrium and close to dissociation.

$$v_{\mathrm{b}}(r) = \frac{1}{2} k_{ij}^{r} (r - r_{\mathrm{m}})^2 \tag{9}$$

$$v_{\mathrm{Morse}}(r) = \varepsilon_{\mathrm{m}} \left(1 - e^{-a(r - r_{\mathrm{m}})}\right)^2 \tag{10}$$

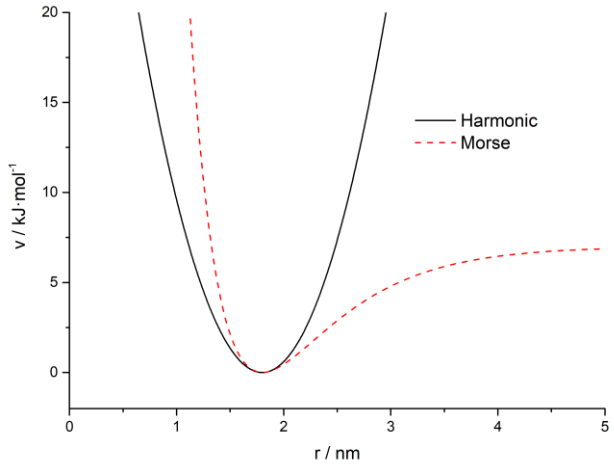

Figure 5: Bonded pair potentials

II.2.3.2 Angle potential

The angle potential is a three-body interaction. Its harmonic expression in equation 11 follows that of the harmonic bond stretching potential v_{b}, with k_{ijk}^{θ} the angle constant, θ_{ijk} the angle in radians as defined in Figure 4 and θ_{m} the equilibrium angle.

$$v_{\mathrm{a}}(\theta_{ijk}) = \frac{1}{2} k_{ijk}^{\theta} (\theta_{ijk} - \theta_{\mathrm{m}})^2 \tag{11}$$

II.2.3.3 Dihedrals

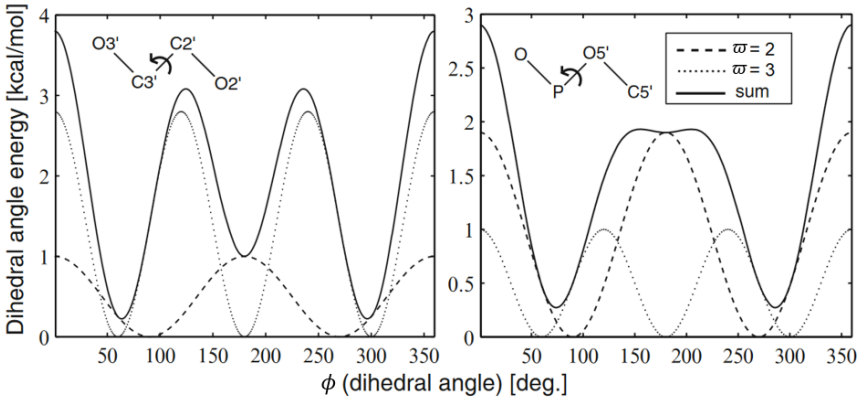

Figure 6: Torsion angle potentials with periodicities of 2 and 3 and the sum of both for an O-C-C-O nucleic acid ribose (left) and a O-P-O-C nucleic acid (right) rotation. Adapted by permission from Springer Nature: Springer, [101]*, © Springer Science+Business Media, LLC 2010*

The four-body interaction potential in equation 12 describes a torsion or dihedral angle. Proper dihedral angles are defined according to the UIPAC convention, where in the case of four atoms i, j, k and l, ϕ_{ijkl} is the angle between the ijk and jkl planes. The *cis* configuration corresponds

to $\phi_{ijkl} = 0$. ϖ is the periodicity of the function, V_n is the associated barrier height and ϕ_s is the phase shift angle.

$$v_d^n(\phi_{ijkl}) = \frac{1}{2}V_n(1 + \cos(\varpi\phi_{ijkl} - \phi_s)) \quad (12)$$

The same group of four atoms can contribute multiple terms to the torsion potential, resulting in a form of truncated Fourier series allowing to better describe an energy landscape, as shown in Figure 6, adapted from [101]. Improper dihedrals can be expressed as a harmonic potential analogous to equations 9 and 11, or through a periodic function such as (12) [102].

For small molecules, several cross-terms exist for the expression of the bonded potential, for example bond-angle or bond-bond. In the case of larger molecules, such as peptides and proteins, the above mentioned terms are enough. In fact, for most bond lengths, the range of variation around the local energy-minimum is small, with very short time scales and large restoring forces. Angles are somewhat looser, but dihedrals vary a lot more [103].

II.2.4 Peptides

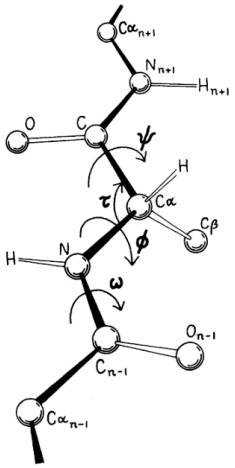

Figure 7: "A key to nomenclature for the atoms of the polypeptide chain, the tetrahedral bond angle τ and the backbone dihedral angles ϕ, ψ and ω." Reprinted by permission from Springer Nature: Springer, [103]*, © Plenum Press, New York 1989*

In the case of peptides and proteins, which are biopolymers of amino acid monomer units, a distinction is made between the side chain dihedrals and those of the main polymer chain. The latter is called the *backbone* and is formed by a series of amide bonds, or *peptide bonds*. The backbone dihedral angles have their own notation convention as shown in Figure 7. Due to the partial double-bond character of the peptide bond, ω is in the large majority of cases very close to flat (180 ° ± 10 °) with C_α, C, N_{n+1} and $C_{\alpha_{n+1}}$ in the same plane. These dihedrals will determine the secondary structure of a protein or large peptide. The conformation in general will be determined through the backbone structure as well as the side-chain dihedrals, depending on the flexibility of the latter. An overview of the 21 proteinogenic amino acids is given in figure 8. The amino acids at the ends of the chain are referred to as N-terminal and C-terminal, depending on whether they have a free amino or carboxyl group remaining, respectively.

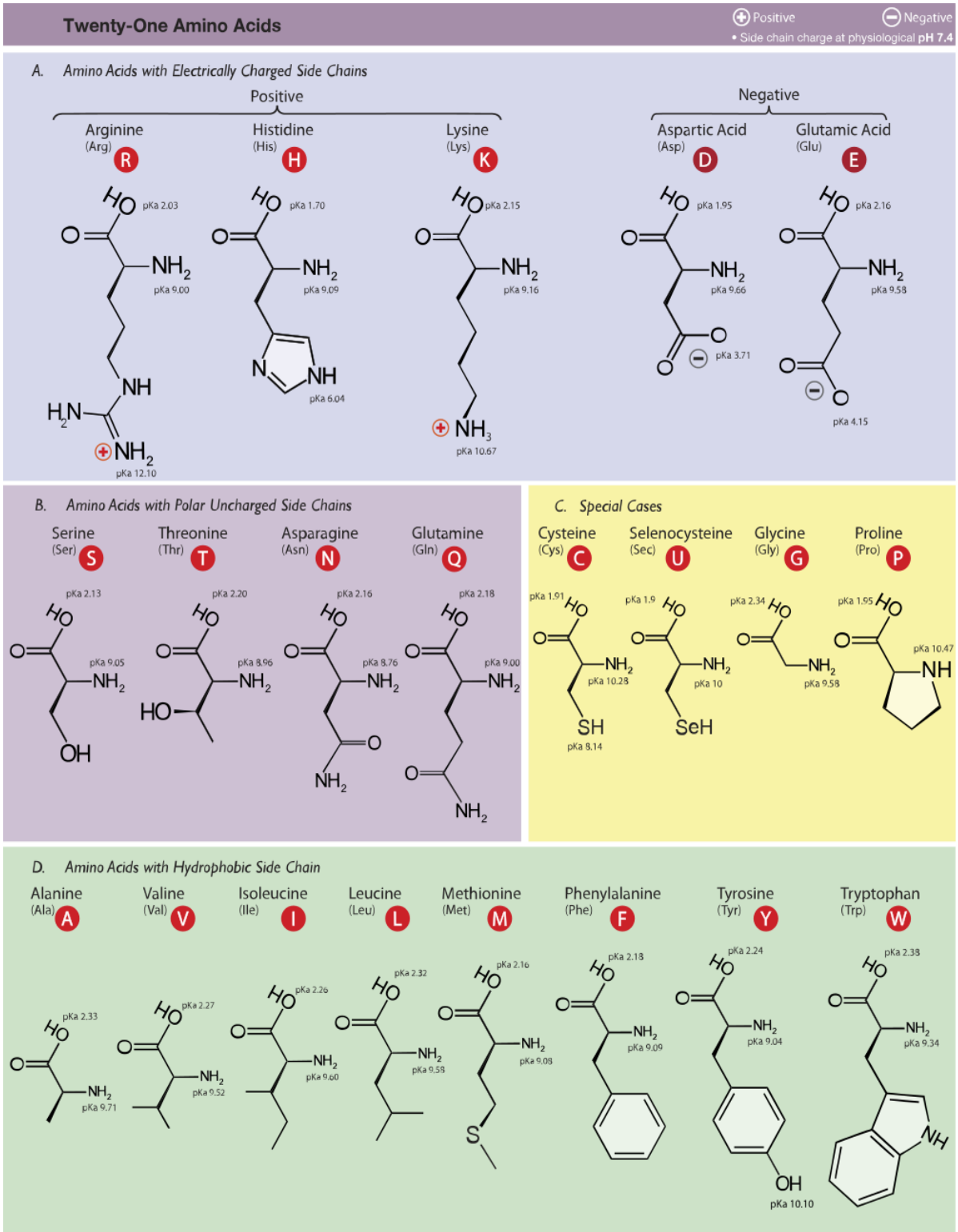

Figure 8: The 21 proteinogenic L-α-amino acids by Dan Cojocari, Princess Margaret Cancer Centre, University of Toronto. Licensed under CC BY-SA 3.0. https://commons.wikimedia.org/wiki/File:Amino_Acids.svg

The borders remain unclear, but if the number of amino acid monomer units is approximately below 50, the biopolymer is called a peptide. Above 50, it is a protein. Approximately under 20 amino acids are oligopeptides. Its charge state in solution depends on the pH according to the pKa values in figure 8.

Biopolymers such as peptides, proteins and DNA are treated in force fields as a series of monomer units with their own parameters. These monomers are an individual charge unit, called residue, meaning that the sum of the partial charges for one residue must add up to an integer. In the case of peptides and proteins, the residues are single amino acids. The most popular force field families for biomolecular simulations are CHARMM (Chemistry at HARvard Molecular Mechanics), AMBER (Assisted Model Building with Energy Refinement) and OPLS (Optimized Potential for Liquid Simulations) [104,105]. OPLS has been optimized to reflect the properties of liquids, while CHARMM and AMBER are more typical for biopolymers. Each force field has its own set of parameters for their bonded and non-bonded interactions, with slight variations. An example is given in figure 9 for alanine and partial atomic charges.

	OPLS-aa	CHARMM27	AMBER99sb-ildn
N	-0.50	-0.47	-0.4157
H	0.30	0.31	0.2719
C_α	0.14	0.07	0.0337
H_α	0.06	0.09	0.0823
C_β	-0.18	-0.27	-0.1825
$H_{\beta1}$	0.06	0.09	0.0603
$H_{\beta2}$	0.06	0.09	0.0603
$H_{\beta3}$	0.06	0.09	0.0603
C	0.50	0.51	0.5973
O	-0.50	-0.51	-0.5679

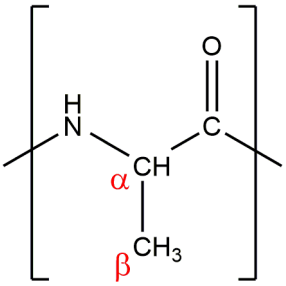

Alanine residue

Figure 9: Alanine residue and its partial atom charges given as multiples of the elementary charge for three force field implementations

Before a molecular dynamics simulation is run, an energy minimization is performed. This means that atomic positions are adjusted so that the net force on each atom is close to 0. It enables a suitable starting point for the MD simulation, free of steric constraints and with appropriate bond lengths and angles. Since the potential function is known (equation 6), finding a local minimum for it implies finding the point where all the first order partial derivatives are equal to zero and the second order ones are non-negative; i.e. the Hessian matrix[6] has non-negative eigenvalues. Saddle points in the potential energy landscape are passes between energy minima and correspond to Hessian matrices with both negative and positive eigenvalues. In practice, computing a Hessian matrix at every time step of an energy minimization algorithm becomes expensive, both in computing power as well as storage requirements. This is the reason why it is often preferred to only use the first derivatives for energy minimization, taking steps in the direction of the negative gradient [102].

Most structures found in nature often correspond to basins around minima of the potential energy surface, i.e. the most energetically favorable arrangements of atoms. Energy minimization algorithms which directly descend into an energy well might miss the lowest energy minima through energetic trapping. In order to overcome this situation, a simulated annealing procedure

[6] Matrix of partial second order derivatives

can be performed. This is a form of function optimization which is used to find its global minimum. In a similar way to annealing in metallurgy, the molecule which is subjected to simulated annealing in molecular dynamics undergoes a series of temperature cycles. Heating, equilibration at a high temperature then cooling down is repeated x times. The x structures which are generated are energy minimized and the y lowest energy conformers among them are subjected to another series of x' simulated annealing cycles. The y' lowest energy structures among the x' generated structures are then selected, resulting in $y \times y'$ low energy structures. These are then candidate structures which are used for structure attribution when comparing theory to experiment.

II.3 Ion mobility spectrometry

II.3.1 Motion of ions in the gas phase

Ion mobility spectrometry is a technique which enables the analysis of ions in the gas phase. It is based on the movement of ions through a gas under the influence of an electric field E, whereby ions are separated according to their ion mobility K. If the ions are thought of as a mobile phase advancing through and interacting with a quasi-stationary gaseous phase, a parallel to gas chromatography or electrophoresis can be drawn up. This is why the technique has been formerly known as plasma chromatography or even gaseous electrophoresis [106]. IM spectrometry does not rely on the same principle of partition as gas chromatography but it is an electrophoretic technique [107]. The fundamental mobility equation is presented in equation 13, where v_d is the drift velocity of the ion through a specific gas at a given temperature T and pressure P. It is valid when the ions are thermalized, meaning that they are in thermal equilibrium with the surrounding gas and that any energy gained through collisions with the medium is negligible in comparison to this. These conditions are referred to as low field conditions.

$$\overrightarrow{v_\mathrm{d}} = K\vec{E} \tag{13}$$

At low field strengths, K relates to the diffusion coefficient D of a cloud of ions in an electric field through what is known as the Einstein, Nernst-Einstein, Nernst-Townsend or even Nernst-Townsend-Einstein relationship (equation 14).

$$K = \frac{ZeD}{k_\mathrm{B}T} \tag{14}$$

where Z is the charge state of the ion and T the gas temperature. Both D and K directly depend on the temperature, the pressure and the ion-gas pair.

Equation 14 derives from (15), the expression of the ionic flux density $\vec{j}$ through equation 13 and Fick's law of diffusion, which relates $\vec{j}$ to the gradient of the ion spatial number density $\vec{\nabla}n$ via D.

$$\vec{j} = n\overrightarrow{v_\mathrm{d}} - D\vec{\nabla}n \tag{15}$$

Equation 15 then leads to a continuity equation of the form

$$\frac{\partial n}{\partial t} - \vec{\nabla}j + (\langle\alpha\rangle - k_1^-)n = 0 \tag{16}$$

where $\langle\alpha\rangle$ is the rate of creation of ions and k_1^- their rate of annihilation [108,109]. Hence, by adding a source term $\beta(x,y,z,t)$ to represent an input of ions at the beginning of the drift region, the transport equation describing the three-dimensional drift and diffusion of a single ion species is can be written as

$$\frac{\partial n(x,y,z,t)}{\partial t} = \mathcal{D}n + \beta(x,y,z,t) \tag{17}$$

where $\mathcal{D}$ is an operator defined as

$$\mathcal{D} \equiv D_{\mathrm{T}}\left(\frac{\partial^2}{\partial x^2} + \frac{\partial^2}{\partial y^2}\right) + D_{\mathrm{L}}\frac{\partial^2}{\partial z^2} - v_{\mathrm{d}}\frac{\partial^2}{\partial z} + \langle\alpha\rangle - k_1^-. \tag{18}$$

When in high field conditions, the scalar diffusion coefficient D becomes a tensor as defined in (19), where D_{T} and D_{L} are the transverse and longitudinal diffusion coefficients, respectively.

$$\mathrm{D} \equiv \begin{bmatrix} D_{\mathrm{T}} & 0 & 0 \\ 0 & D_{\mathrm{T}} & 0 \\ 0 & 0 & D_{\mathrm{L}} \end{bmatrix} \tag{19}$$

Thus, equation 17 is valid in the general case, for both low and high field conditions.

If ion production or annihilation rates are considered negligible, for a narrow initial ion distribution, the ion density along the drift axis becomes

$$n(0,z,t) = \frac{s}{\sqrt{4\pi D_{\mathrm{L}}t}}\left[1 - \exp\left(-\frac{r_0^2}{4D_{\mathrm{T}}t}\right)\right]\exp\left[-\frac{(z - v_{\mathrm{d}}t)^2}{4D_{\mathrm{L}}t}\right] \tag{20}$$

with r_0 the radius of the ion cloud and s the planar source density [108]. In the case of a wider initial ion distribution, Spangler and Collins [109,110] proposed the following solution

$$n(0,z,t) = \frac{n_0}{2}\left[1 - \exp\left(-\frac{r_0^2}{4D_{\mathrm{T}}t}\right)\right]\left[\mathrm{erf}\left(\frac{z - v_{\mathrm{d}}t}{2\sqrt{D_{\mathrm{L}}t}}\right) - \mathrm{erf}\left(\frac{z - v_{\mathrm{d}}t - v_{\mathrm{d}}t_{\mathrm{g}}}{2\sqrt{D_{\mathrm{L}}t}}\right)\right] \tag{21}$$

where t_{g} is the initial width of the gate pulse applied to the shutter grid, which determined the width of the initial ion cloud in their experiments, and n_0 is the initial ion concentration. The full width at half maximum (FWHM, ω_{h}) of the resulting ion mobility peak can be approximated by

$$\omega_{\mathrm{h}}^2 = t_{\mathrm{diff}}^2 + t_{\mathrm{g}}^2, \tag{22}$$

where t_{diff} is the temporal FWHM of a Gaussian peak created by diffusion broadening of a narrow ion packet during its drift though the drift tube. If the initial ion density exceeds a certain value, defined by Spangler in [111], interionic interactions, known as the space charge effect, must be taken into account and corrected for in (20–22).

The relation between the FWHM and the standard deviation allows to determine t_{diff} through σ_{time}, the temporal spreading of the ion cloud.

$$t_{\mathrm{diff}} = 2\sqrt{2\ln(2)}\ \sigma_{\mathrm{time}}. \tag{23}$$

σ_{time} relates to the spatial spreading, σ_{space}, through the drift length L and drift time t_{d}, as shown in (24).

$$\frac{\sigma_{\text{space}}}{L} = \frac{\sigma_{\text{time}}}{t_{\text{d}}} \tag{24}$$

The spatial spreading of an ion peak arriving at the detector will depend on the diffusion coefficient. In one dimension, it corresponds to the mean square deviation of the position [111,112] such that

$$\sigma_{\text{space}} = \sqrt{2D_{\text{L}}t_{\text{d}}}. \tag{25}$$

By applying equations 25 and 24 and using the relation between the standard deviation of a Gaussian peak and its FWHM, equation 26 is obtained.

$$t_{\text{diff}} = \frac{1}{L}\sqrt{16\ln(2)\,D t_{\text{d}}^3} \tag{26}$$

The resolution of a spectrometer, defined by the ratio $t_{\text{d}}/\omega_{\text{h}}$, can thus be written for an infinitely narrow ion distribution as

$$\frac{t_{\text{d}}}{\omega_{\text{h}}} = \frac{L}{\sqrt{16\ln(2)\,D_{\text{L}}\,t_{\text{d}}}}, \tag{27}$$

which shows that the resolution of an IM spectrometer can be improved by employing a longer drift tube or decreasing the drift times (through a higher electric field). According to (22), a broader initial ion distribution ($t_{\text{g}} > 0$) would decrease the resolution.

II.3.2 Collision cross-section determination: ion-neutral interaction models

The mobility in equation 14 can also be written as the Mason-Schamp equation 28, where the dependence on ion-neutral interactions is made apparent through the average collision cross-section Ω_{D}.

$$K = \frac{3}{16}\frac{Ze}{N}\left(\frac{1}{m_{\text{I}}} + \frac{1}{m_{\text{G}}}\right)^{\frac{1}{2}}\left(\frac{2\pi}{k_{\text{B}}T}\right)^{\frac{1}{2}}\frac{1}{\Omega_{\text{D}}} \tag{28}$$

Ω_{D} is actually a momentum transfer collision integral, averaged over all ion-gas relative thermal velocities and orientations. N is the gas number density, m_{I} the ion mass and m_{G} the mass of the neutral gas molecule. The mobility constant can then be normalized to standard temperature and pressure conditions (STP) to obtain the reduced mobility K_0, which is a constant for a given ion under low field conditions. The standard temperature T_0 and pressure P_0 correspond to 273.15 K and 101,325 Pa.

$$K_0 = K\frac{T_0}{T}\frac{P}{P_0} \tag{29}$$

Under low field conditions, K_0 is considered a constant, and a characteristic value of an ion. Reported values are typically not in perfect agreement, the common accepted precision of most low resolution spectrometers being ± 2 %. However, high accuracy measurements of K_0 with a precision of ± 0.2 % have been achieved [113,114]. Thus, a substance with well-known reduced mobility can be used as a standard for IM spectrometry in order to correct for different

experimental conditions and variabilities. This then enables the accurate determination of the unknown reduced mobility as follows:

$$\frac{K_{0\,(\text{unknown})}}{K_{0\,(\text{standard})}} = \frac{t_{\text{d}\,(\text{standard})}}{t_{\text{d}\,(\text{unknown})}} \tag{30}$$

Given the intrinsic relationship between Ω_{D} and K, at a given temperature and pressure, under low field conditions, Ω_{D} can be used to characterize a substance. It is therefore useful to have reference values against which to compare experimental results. Once a molecular structure is known, it is possible to approximate the value of the collision cross-section (CCS). These structures correspond to minima in the potential energy surface of the molecules and are obtained from quantum chemical calculations for smaller molecules or with force fields and simulated annealing for larger ones. There are then various ways to approximate CCS values, each with their own advantages and drawbacks, but they are all based on the equation below, relating to the orientationally averaged collision integral Ω_{D}:

$$\begin{aligned}\Omega_{\text{D}} = \frac{1}{4\pi^2}\int_0^{2\pi} \text{d}\varphi_1 \int_0^{\pi} \text{d}\varphi_2 \sin\varphi_2 \int_0^{2\pi} \text{d}\varphi_3 \frac{\pi}{8} \\ \times \left(\frac{\mu}{k_B T}\right)^3 \int_0^{\infty} \text{d}g\, \text{e}^{-\mu g^2/2k_{\text{B}}T} g^5 \\ \times \int_0^{\infty} \text{d}b\, 2b(1-\cos \text{X}(\varphi_1, \varphi_2, \varphi_3, g, b))\end{aligned} \tag{31}$$

Where μ is the reduced mass, g the relative velocity, b the impact parameter defined in figure 10, φ_1, φ_2 and φ_3 are angles which define the collision geometry and $\text{X}(\varphi_1, \varphi_2, \varphi_3, g, b)$ is the scattering angle. Thus, the different terms correspond to the integrations over all directions of space, over the relative ion-neutral velocity distribution and over all scattering angles.

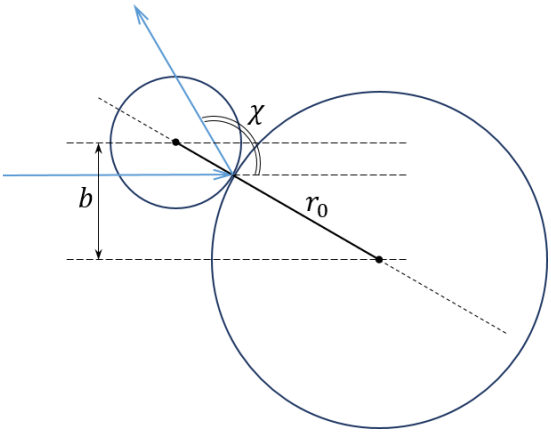

Figure 10: Definition of the scattering angle χ and the impact parameter b

Given that equation 31 is computationally expensive to calculate, different approximations have been made in order to numerically determine collision integrals. Currently, three methods exist: the projection approximation (PA), the exact hard-sphere scattering (EHSS) model and the trajectory method (TM). The latter is not to be confused with the term *trajectory* used in molecular dynamics to refer to the series of time-dependent atomic positions and velocities that constitute

the output of a simulation. These CCS calculation methods, from PA to EHSS to TM, use an additional term to account for an additional interaction. The difference between them is illustrated in figure 11.

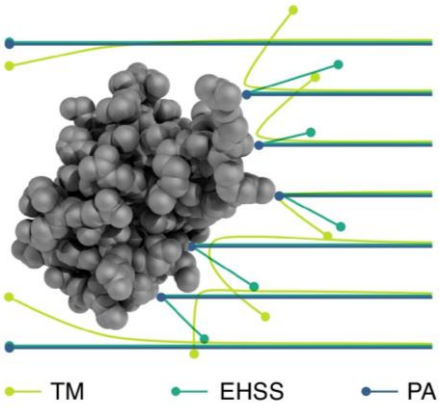

Figure 11: CCS calculation methods. Reprinted from [115]*, © 2017, with permission from Elsevier*

II.3.2.1 Projection approximation (PA)

The simplest CCS approximation technique is by projection approximation. This method is based on the original shadow-projection method proposed by Mack [116]. A series of 2D projections of the target molecule are carried out in order to compute a rotationally averaged surface. Mack did this with a light source, a pencil, paper, a planimeter and various three-dimensional beeswax models of hydrocarbons (Figure 12, left). Nowadays, computational methods use a 3D molecular structure determined from experiment or *in silico*. The atoms are represented by hard spheres with a radius equal to the atom's van der Waals radius. A box is tightly drawn around each 2D projection of the input structure and its cross-section is calculated according to the Monte Carlo method [117] (Figure 12, right):

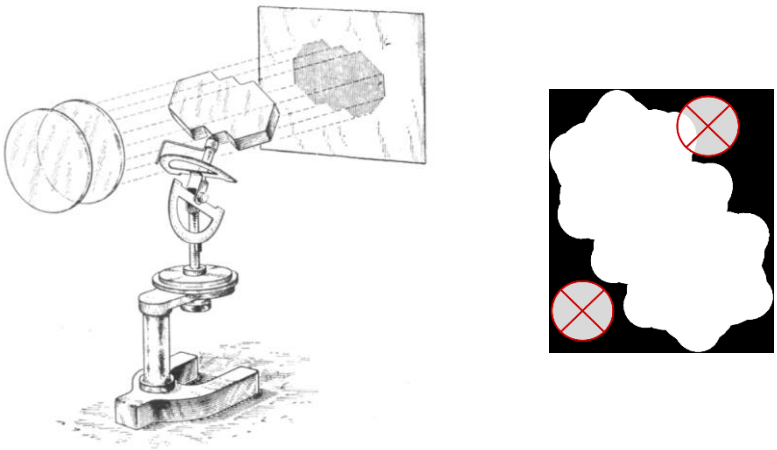

Figure 12: Left: Mack's shadow-projection setup with a beeswax anthracene model. Reprinted with permission from [116]*. ©1925, American Chemical Society. Right: A depiction of the projection approximation algorithm for the anthracene structure using van der Waals radii*

1. Random points inside the box are selected
2. If the distance from a point to any molecular atom center is smaller than the sum of the van der Waals radii of both atom and gas, it is considered a “hit”. If not, it is a “miss”
3. Once the ratio of “hits” to the number of points has converged, it is multiplied by the area of the box to obtain the collision cross-section value for the given orientation

The above can be mathematically expressed as equation 32, a simplification of equation 31.

$$\Omega_{\mathrm{D}} = \frac{1}{4\pi^2}\int_0^{2\pi} \mathrm{d}\varphi_1 \int_0^{\pi} \mathrm{d}\varphi_2 \, \sin\varphi_2 \int_0^{2\pi} \mathrm{d}\varphi_3 \, \pi b_{min}^2 \tag{32}$$

where $b_{\min}$ is the minimum impact parameter for the collision geometry defined by the angles φ_1, φ_2 and φ_3 that avoids hard-sphere contact with the atoms of the molecule. The PA is a good approximation method and the fastest one available, but it fails to take into account ion-gas interactions. A significant error in the CCS values of structures with concave surfaces has been observed, where shadowing from direct collisions or multiple collisions with the same gas atom due to reflections are not accounted for [118]. Introducing time dependence for φ_1, φ_2 and φ_3 in order to incorporate thermal rotation into the equation improves the results, especially for heavier gases, but does not escape the surface convexity pre-requisite for the validity of the approximation [119].

The projected superposition approximation (PSA) method corrects for this concavity dependence by replacing atomic hard-sphere radii with an atomic collision probability. In other words a probabilistic “hit-or-miss” function is introduced in order to calculate the average collision cross section. This value is then corrected by a shape factor accounting for concaveness, thus producing the final CCS value. This method is more computationally expensive than the PA method but not as demanding as the EHSS, producing values which reportedly compare to more sophisticated methods (EHSS and TM) [120–123].

II.3.2.2 Exact hard sphere scattering (EHSS) method

The EHSS method is a more sophisticated method which accounts for the scattering effects during ion-neutral interactions, modelled as hard-sphere collisions, following a potential $v_{\mathrm{HS}}(r)$ with a simple expression:

$$v_{\mathrm{HS}}(r) = \begin{cases} 0 & \text{if } r \geq r_0 \\ \infty & \text{if } r < r_0 \end{cases} \tag{33}$$

Where r_0 is the sum of the van der Waals radii of the molecule and gas atoms. If $b \geq r_0$, the gas atom misses the molecule. If not, a collision takes place. The above case for the PA method (equation 32) is a specific case for the collision of two hard spheres, where the collision integral is equal to the projection. In the EHSS, the influence of the scattering angle χ is made explicit, thus allowing access to the true hard-sphere collision integral by numerically integrating equation 34. The trajectories of the gas atoms are monitored until they leave the system, thus following possible multiple collisions and deflections, which χ accounts for.

$$\Omega_{\mathrm{D}} = \frac{1}{4\pi^2}\int_0^{2\pi} \mathrm{d}\varphi_1 \int_0^{\pi} \mathrm{d}\varphi_2 \sin\varphi_2 \int_0^{2\pi} \mathrm{d}\varphi_3 \times \int_0^{\infty} \mathrm{d}b\; 2b(1-\cos \mathrm{X}(\varphi_1,\varphi_2,\varphi_3,b)) \tag{34}$$

The EHSS has been expanded upon by moving away from hard-sphere atoms with van der Waals radii and instead using surfaces of isoelectronic density to model ions. The method is referred to as the SEDI (scattering on electron density isosurfaces) model [124], and electron density information is obtained from quantum chemical calculations. The surface used in SEDI is smoother than the one resulting from the hard-sphere approximation and provides a more realistic scattering model. Furthermore, the scattering will be dependent on the interaction between the electron clouds of the target ion as well as the gas, which means that SEDI is more accurate than atomic models given that it accounts for changes in the electronic density due to charges.

However, neither of these scattering-based models (nor the PA) account for long-range interactions, which is a further source of deviation from experimental results.

II.3.2.3 Trajectory method (TM)

The trajectory method is the only method which explicitly takes long range interactions into account. It is the most computationally expensive one but one of the most precise methods, in particular for small molecules [115]. In this method the scattering angle is determined by numerically integrating the equations of motion using the potential described in equation 35.

$$\Phi(\varphi_1,\varphi_2,\varphi_3,b,r) = 4\sum_i^n \varepsilon_{\mathrm{m}}\left[\left(\frac{\sigma}{r}\right)^{12} - \left(\frac{\sigma}{r}\right)^{6}\right] - \frac{\alpha_{\mathrm{p}}}{2}\left[\left(\sum_i^n \frac{Z_i e x_i}{r^3}\right)^2 + \left(\sum_i^n \frac{Z_i e y_i}{r^3}\right)^2 + \left(\sum_i^n \frac{Z_i e z_i}{r^3}\right)^2\right] \tag{35}$$

n is the number of atoms in the target ion, $Z_i e$ is the partial charge of the i^{th} atom, x_i, y_i and z_i are coordinates that define the relative position of the i^{th} ion atom with respect to the gas atom, with r the distance between the two and α_{p} the polarizability of the gas atom. The first term is a two-body 6-12 interaction potential (Lennard-Jones interaction) following that of equation 7 and the second term is the ion-induced dipole interaction. The TM CCS thus stems from the most detailed potential form among the available methods and is especially necessary when heavier, more polarizable atoms are considered [125]. The TM was originally developed for monoatomic gases, but a version using nitrogen was also reported [126,127]. Due to the fact that nitrogen is a diatomic molecule, in this version the ion-quadrupole interaction potential (equation 36) and the orientation of the molecule are also taken into account. The quadrupole moment was simulated by assigning negative partial charges to each nitrogen atom and the corresponding positive charge to the center of mass.

$$\Phi_{\mathrm{IQ}} = \sum_{j=1}^{3} \sum_{i}^{n} \frac{Z_i Z_j e^2}{r_{ij}} \tag{36}$$

The indices i and j correspond to the ion atoms and the neutral gas partial charge centers, respectively, with r_{ij} the distance between the charge centers of the atom and the gas. This potential is then averaged over all orientations of the nitrogen molecule and used in the CCS calculation. Although computationally expensive, this is the only method that has thus far been developed for nitrogen, and more generally for any polyatomic neutral gas molecule [126,127].

II.3.3 High field mobility

The motion of an ion through the bath gas will be governed by the collisions that it undergoes with the gas atoms. With a higher electric field E, the drift velocity will increase (equation 13). With a higher pressure, the neutral number density N will be higher, thus incurring in more collisions and kinetic energy losses, slowing the ion down. It is the ratio E/N, also called reduced field strength, which in fact governs the motion of the ions. The unit of E/N is the Townsend (Td), which is equal to 10^{17} V·cm^2. If either the electric field increases or the gas number density decreases significantly, in other words at a high E/N, the ions are no longer thermalized. The latter means that the thermal energy of the drift gas no longer noticeably exceeds the energy gained by the ion through collisions with gas molecules. This is called the standard high field effect.

$$\begin{aligned} K_0\left(\frac{E}{N}\right) &= K_0(0)\left[1 + \alpha_2\left(\frac{E}{N}\right)^2 + \alpha_4\left(\frac{E}{N}\right)^4 + \cdots + \alpha_{2n}\left(\frac{E}{N}\right)^{2n}\right] \\ &= K_0(0)\left[1 + \alpha\left(\frac{E}{N}\right)\right] \end{aligned} \tag{37}$$

In this case, the reduced mobility is no longer a constant, but rather a function of the reduced field strength according to equation 37 [128], where $K_0(0)$ is the reduced mobility under zero field conditions and α the so-called alpha function, which describes the dependence of the ion mobility on E/N.

$$(E/N)_{\mathrm{c}} = 8 k_{\mathrm{B}} T \frac{\Omega_{\mathrm{D}}}{Ze} \sqrt{\frac{2 y m_{\mathrm{I}}}{3\pi(m_{\mathrm{I}} + m_{\mathrm{G}})}} \tag{38}$$

The onset of the high field regime takes place after a critical reduced field value, $(E/N)_{\mathrm{c}}$, given in equation 38 [128]. The parameter y is a coefficient dependent of the relative measurement accuracy. Given that y is unknown, equation 38 is in no way quantitative, but it can give a good idea regarding the dependence of $(E/N)_{\mathrm{c}}$ on the ion and gas properties. In the Rayleigh limit ($m_{\mathrm{I}} \gg m_{\mathrm{G}}$), $(E/N)_{\mathrm{c}}$ is proportional to Ω_{D}/Z, meaning it's controlled by the size and geometry of the ion rather than that of the gas. For ions of the same size, the dependence on the mass is rather weak, as for ions in the Lorentz limit ($m_{\mathrm{I}} \ll m_{\mathrm{G}}$). This can be seen by reformulating equation 38 as equation 39 [128], where m_{I} is only implicitly included within K_0.

$$(E/N)_{\mathrm{c}} = \frac{\sqrt{3k_{\mathrm{B}}yT/m_{\mathrm{G}}}}{K_0 N_0} \tag{39}$$

In general, the magnitude of the effect decreases for heavier ions and gas atoms. $(E/N)_{\mathrm{c}}$ both increases for larger gas atoms and for larger ions as seen in figure 13. There, the mobility of monoatomic cations in monoatomic gases is measured as well as calculated from ab-initio potentials. These are the simplest models to calculate, giving good agreement between experiment and *in-silico* calculations. There are two types of possible behavior for an ion/gas pair: in type 1, the mobility of the ions monotonically decreases with increasing E/N and for type 2 ions it first rises to a maximum before dropping.

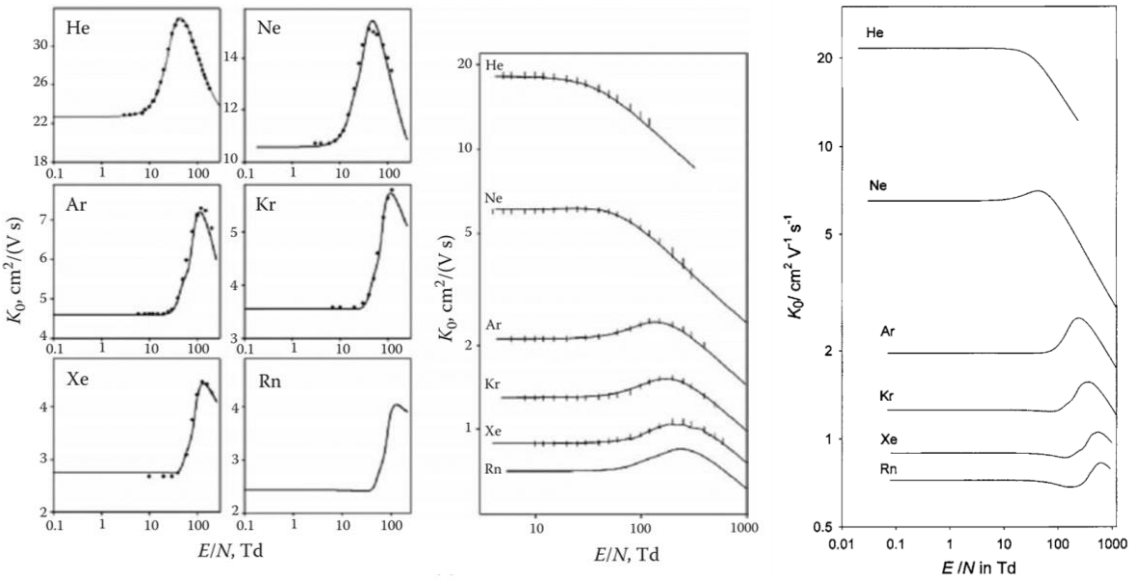

Figure 13: Reduced mobility of Li^+ (left), Cs^+ (center) and Cd^+ (right) in noble gases. Li^+ and Cs^+ republished with permission of Taylor & Francis Group, LLC, from [128]*, © 2009; permission conveyed through Copyright Clearance Center, Inc. Originally from* [129,130]*, reproduced with permission of the PCCP Owner Societies. Cd^+ reproduced from* [131]*, with the permission of AIP Publishing*

When considering ion-neutral interactions as in Figure 11, glancing collisions are the most sensitive to the ion-gas collision energy. Glancing collisions are those which are no longer hard-sphere collisions ($b > b_{\mathrm{min}}$) but where an interaction still occurs through long-range potentials. When $b \approx b_{\mathrm{min}}$, slower gas molecules are more strongly scattered than faster, more energetic ones. Thus, as E/N increases, the collisions become more energetic, the deflection is lower and by (28) and (31), the mobility increases. After a certain value $(E/N)_{\mathrm{h}}$, any potential approaches the hard-sphere potential, for which the mobility continuously decreases [128]. Type 1 behavior then takes place if $(E/N)_{\mathrm{h}} < (E/N)_{\mathrm{c}}$. Cooling and heating can make ions switch behavior from type 1 to type 2 and back, respectively. A third type of behavior has been observed for heavier transition metal ions (such as Hg^+ and Cd^+) in heavy noble gases (Figure 13, right): due to the high polarizability of both ion and gas, strong dispersion forces scaling in r^{-6} occur. These lead to a dip in the mobility before subsequently rising after $(E/N)_{\mathrm{c}}$.

In polyatomic gases, charge-induced quadrupole interactions also scale as r^{-6}. These interactions, along with inelastic collisions, make the dip more common for polyatomic

species, so-called non-standard effects also exist which can influence K_0. These effects depend only on the increase in electric field rather than on reduced field strength. They are collisional alignment, dipole alignment, complex dissociation and inelastic collisions. For dipole alignment, consider a long molecule with a point charge at one end. At high electric fields the Coulomb force exerted on the charge will result in the alignment of the molecule along its drift axis, thus resulting in a much lower apparent collision cross-section and by extension, a much higher mobility. In collisional alignment, medium-sized and small ions are oriented in a preferential direction through collisions with neutral gas atoms. High electric field values can also result in the dissociation of weak bonds, leading to unfolding of molecules or even to the dissociation of complexes. These structural changes will also result in a drastic change in mobility. Inelastic collisions, unlike elastic hard-sphere collisions, enable energy transfer to vibrational or rotational modes of the polyatomic gas and/or ion. This decreases the apparent effect of the rising E/N on the mobility.

III. Experimental and theoretical methods

III.1 Experimental

III.1.1 General

Two IR lasers were used in the experiments. Both were Q-switched Nd:YAG OPO lasers with a nominal pulse full width at half maximum (FWHM) of 7 ± 2 ns. The first was an Opolette 2940 (Opotek Inc.) with a fixed wavelength of 2,940 nm and a peak energy of 6 mJ. The second was a tunable wavelength Opolette IR 2731 (Opotek Inc.) with a peak energy of 3 mJ. It was set to 2,940 nm as well, the wavelength corresponding to the absorption maximum of the –OH stretch vibration of water. The repetition rate was set at 20 Hz and the Q-switch peak power was delivered after 140 µs. The focused spot size was 0.28 mm^2.

Observation of the IR-MALDI dispersion plume took place with a CCD camera (either DFK 41 AU02, The Imaging Source or NS4133BU, iCube). A red stroboscopic diode was synchronized with the laser Q-switch and positioned along the optical axis of the camera, so as to place the dispersion plume of the IR-MALDI process exactly between diode and camera. The droplets produced in the dispersion mechanism cast a shadow in front of the diode, hence this observation technique's name of "shadowgraphy". The delay between the diode and the laser was varied with a delay generator. Due to the opening time of the camera shutter, each picture was an average over two subsequent laser pulses. Inverted color images were obtained by subtracting a lightened background image taken before the dispersion process from the plume image and returning the absolute values (Difference blending mode) in order to improve contrast.

For comparison purposes, the ESI-IM spectrometer described in [132] was used as well as a linear ion trap mass spectrometer (LTQ XL, Thermo Scientific) with an IR-MALDI source. The droplet source (see below) was simply placed in front of the ion transfer tube of the mass spectrometer and the resulting plume was sucked in through hydrodynamic forces.

The drift gas was nitrogen.

III.1.2 Substances and reactions

Most substances were acquired from Sigma Aldrich. The investigated substances are promazine, chlorprothixene, perphenazine, imipramine, atrazine, bradykinin, diquat monohydrate, chloridazone, metoxurone, monurone, methabenzthiazurone, chlortolurone, isoproturone, metazachlor, metolachlor, histidine, arginine, ammonium carbonate, methylammonium bromide (MAB), dimethylamine hydrochloride (DMAC) and the tetraalkylammonium bromides [$N(C_nH_{2n+1})_4Br$]: tetramethylammonium bromide [TMAB $N(CH_3)_4Br$], tetrabutylammonium bromide [TBAB, $N(C_4H_9)_4Br$], tetrahexylammonium bromide [THAB, $N(C_6H_{13})_4Br$], tetraoctylammonium bromide [TOAB, $N(C_8H_{17})_4Br$], tetradecylammonium bromide [TDAB, $N(C_{10}H_{21})_4Br$], and dodecylethyldimethylammonium bromide [DEDMAB, $N(CH3)_2(C_2H_5)(C_{12}H_{25})Br$].

All other peptides (Ac-ACTERMAAHNLCGG-NH_2, ADLKIESS, AFFRHD-NH_2, AIENPADVS-NH_2, CRRETAWAC, DNDAN-NH_2, DNDPN-NH_2, DNDRN-NH_2, EMGRAPLDL, GILGFVFTL-NH_2, GILGFVTFTL,

GRADSP, GRGDNP, GRGDSP, IVAIENPAD-NH_2, KKGSKK-NH_2, KRHRK-NH_2, LLHLAVIGALLAVGATKVPRNQDWLGVSRQL, NALPE, RAKFKQLL, RLRSGRS-NH_2, RPKPQQ, SIINFEKL-NH_2, VLDFAPPGA, Ac-YGDSMDRIEKDRLQGMA-NH_2) were synthesized by peptides&elephants (Hennigsdorf, Germany) via solid phase synthesis with a Tetras Asynchronous Multiple Peptide Instrument (Advanced ChemTech). For ESI, the freeze-dried peptide probes were dissolved in a mixture of acetonitrile and water in an eight-to-two volume ratio (ACN/H_2O 8:2) and diluted to a concentration of 250 µM. TBAB was also added to these solutions in a concentration of 2.5 µM and used as a mobility standard for drift time correction. Unless stated otherwise, peptide solutions with a concentration of 500 µM and 1 µM TBAB in ACN/H_2O 1:1 were prepared and analyzed by IR-MALDI.

Cysteine-containing peptides form a disulfide bond in the presence of oxygen. In order to study the linear forms of these peptides, the bonds were cleaved by adding a 20-fold excess of dithiothreitol (DTT) in the presence of 1 mM sodium tetraborate (pH = 8.6) over 24 h [133].

III.1.3 Atmospheric pressure IM spectrometer

Two IR-MALDI source variations were used in combination with the atmospheric pressure spectrometer (Figure 14). First, a droplet source was employed. It consists of a solution pumped with a syringe pump (KD Scientific) through a gauge 32 stainless steel capillary (Hamilton, 110 µm i.d., 230 µm o.d.), with rates of about 10 µL·min^{-1}. This produced a droplet of about 1 mm at the tip of the capillary, onto which the laser beam was focused. The solvent was acetonitrile and water in a one-to-one ratio (ACN/H_2O 1:1). A sample valve (Knauer) with a sample loop of 20 µL was added for direct analyte solution injection. The second variation which was used was the microbeam source. A glass capillary nozzle (o.d. = 1.0 mm, i.d. = 0.235 mm, tapered to i.d. = 20 ± 2 µm at the nozzle, Biomedical Instruments) was coupled to an HPLC pump (Azura P 6.1 L, Knauer) and a sample loop was added, as with the droplet source. A conductive sleeve was wrapped around the glass capillary in order to apply a voltage and keep a linear electric field in the ionization region.

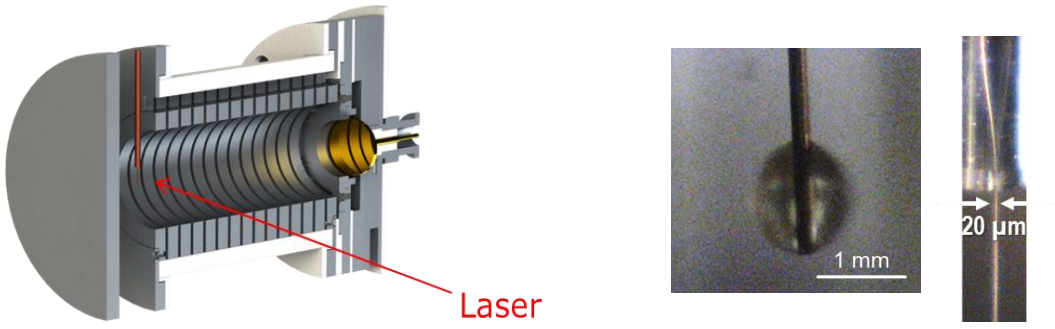

Figure 14: Left: Simplified schematics of the atmospheric pressure ion mobility spectrometer used in combination with the IR-MALDI source. Right: Droplet source and microbeam source. The diameter of the beam is 20 µm

The HPLC parameters were the same as in [132]: a reversed-phase column (Hypersil Gold, Thermo, 150 × 2.1 mm, 3 µm) used in conjunction with a water-acetonitrile gradient which proceeded in two stages. First, the solvent composition stayed constant for 5 min at 25/75 % acetonitrile/water.

The percentage of acetonitrile then steadily rose up to 80 % over 20 min. The flow rate was kept constant at 300 µL·min^{-1}.

The spectrometer itself (Figure 14) was assembled out of a series of alternating stainless steel ring electrodes (4 cm inner diameter, 4 mm thickness) and teflon separator rings, resulting in an 11 cm-long drift tube with a Faraday plate detector and a 10^{10} V·A^{-1} amplifier (FEMTO DLPCA-200) connected to a USB oscilloscope (Handyscope HS3, TiePie engineering). The drift tube was heated externally to 170 °C with an electrically insulated heating wire wrapped around its length. The temperature was chosen based on previous work [134]. The ionization region consisted of a repeller plate placed in front of the first drift ring electrode, which housed a metallic mesh for electric shielding of drift and ionization regions with regard to each other. Two variations of the ionization region were used. In the first one, used in most cases, the separation between repeller and drift tube was set at 5 mm, with either the droplet source capillary or the microbeam capillary centered between them. The other version was used only in one experiment in order to study the ablation plume with the droplet source. The distance between repeller and drift tube was set at 10 mm. The distance between the metal capillary of the droplet source and the inlet of the drift tube was then varied by moving the spectrometer along its drift axis while the capillary and the optical components remained static. Thus, reproducibility between measurements was ensured.

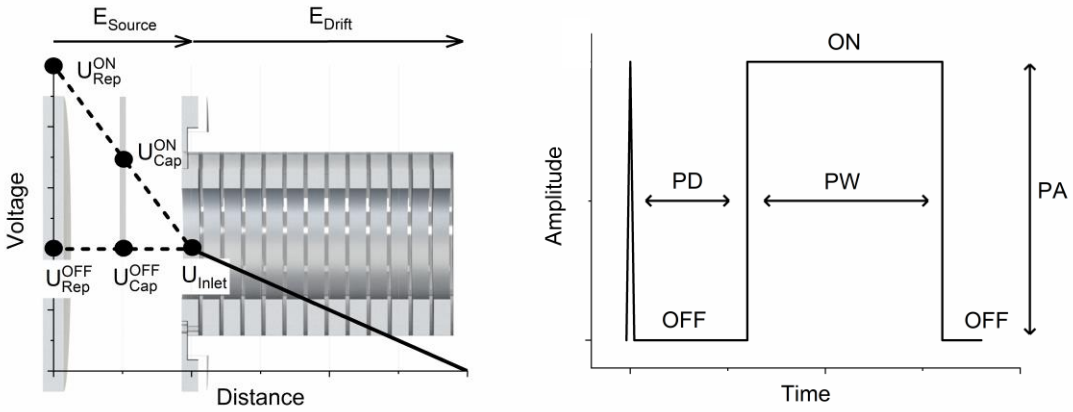

Figure 15: Left: Illustration of the pulse parameters in the atmospheric pressure IR-MALDI spectrometer ionization region. Right: Depiction of the ion injection pulse characteristics for cations

Pulsed ion injection was used in order to enable desolvation in the ionization region before introduction of the ions into the drift region. It is illustrated in figure 15, left. The electric field in the drift region (E_{Drift}) was set through a resistor cascade by adjusting the voltage of the first ring electrode (U_{Inlet}). In the ionization region, the electric field (E_{Source}) was set by applying independent voltages to the repeller plate (U_{Rep}) and the capillary (U_{Cap}), always so as to keep E_{Source} linear. Synchronized pulsed floating potentials (U^{ON}) were applied on top of a base potential (U^{OFF}) for these two electrodes. The superscripts "ON" and "OFF" refer to whether the floating potential is applied or not. The base potential was set so that $U^{OFF}_{Rep} = U^{OFF}_{Cap} = U_{Inlet}$, creating a field-free region where the ions are first produced. After a certain time, they are "pushed" into the drift region by the floating potential. For cations, this means that $U^{ON}_{Rep} > U^{ON}_{Cap} > U_{Inlet} > 0$. The pulsing sequence can be observed in figure 15, right. The beginning of the sequence

is given by the laser pulse. After a certain delay (pulse delay, PD), the floating potential is turned on for a certain amount of time (pulse width, PW). The pulse amplitude (PA) relates to the magnitude of the floating potential, so that $PA \propto \left(U_{Rep}^{ON} - U_{Rep}^{OFF}\right)$. Dividing by the distance between the repeller plate and the first ring electrode gives the PA in $V \cdot cm^{-1}$.

III.1.4 Reduced pressure spectrometer

A spectrometer (Figure 16) was specifically developed in our group to work at reduced pressure [135]. It can be operated at pressures as low as 6 mbar and consists of a 21.2 cm long, vacuum-tight drift tube heated with two heating sleeves to a temperature of 40 °C. The drift tube is made of alternating stainless steel ring electrodes and polyether ether ketone (PEEK) separators. On one end, it has a Faraday plate detector with a 10^9 $V \cdot A^{-1}$ amplifier (ISAS Elektronik VV9) connected to a digital phosphor oscilloscope (Tektronix TDS 5052). On the other end, a vacuum tight ionization cup-like section caps the tube. It consists of a stainless steel cup encased in an insulating PEEK shell. A grid prevents cross-talk between drift tube and cup. The latter is fitted with three window openings, a large opening for the vacuum pump and as a smaller opening for the introduction of a 1/16 in (1.59 mm) tube, such as a standard MS ion transfer tube. The distance between the center of the tube and the metal grid on the first drift ring was 6.5 mm. The whole cup is heated with a heating rod to 60 °C. The carrier solution composition was ACN/H_2O 8:2.

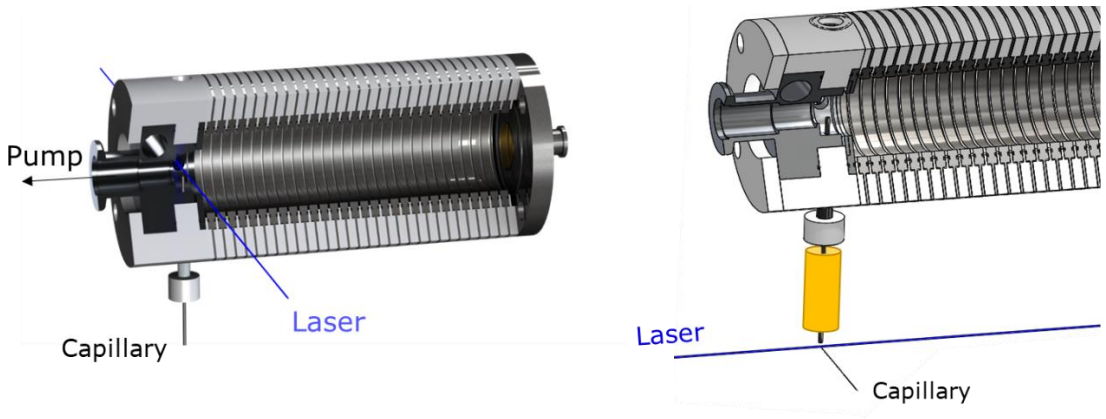

Figure 16: Reduced pressure spectrometer. Left: reduced pressure ionization. Right: atmospheric pressure ionization

Two configurations of the source were used. In one version, the sample capillary from the droplet source was introduced through a stainless steel tube and vacuum fittings into the cup (Figure 16, left). The ionization then took place at reduced pressure by focusing the laser through a CaF_2 window. In the other version, an MS ion transfer tube (LTQ Orbitrap XL, ThermoFisher Scientific) was used as an interface between the cup, at reduced pressure (RP), and the droplet source, operating at atmospheric pressure (AP) (Figure 16, right). The transfer tube was heated externally to 200 °C and a spherical repeller electrode was hooked to the end of the ion transfer tube in order to improve ion transmission (Figure 17). The sample capillary was at a distance of around 0.7 mm from the ion transfer tube and the electric field generated over this distance by the voltage difference between the ion transfer tube (with extraction pulse off) and the capillary is referred to as inlet field (IF).

Figure 17: Spherical repeller electrode at the end of the ion transfer tube. The sample capillary tip is just before that of the ion transfer tube. A Teflon sheet insulates the heating element from the high voltage components

The voltage in the cup was also pulsed, to serve as a sort of ion gate. As with the AP IM spectrometer, the electric field in the drift region E_{Drift} was fixed through a resistor cascade and adjusting the voltage of the first drift ring electrode. The cup and the tube coming into it are kept at the same voltage, so the pulse amplitude is defined through the length between the tube and the inlet grid. This means that for the RP ionization, the droplet capillary is also at the same voltage as the cup whereas for the AP ionization setup only the ion transfer tube is at the same voltage as the cup, with an independent droplet capillary voltage. The voltage pulsing scheme was such that $0 < U_{Cup}^{OFF} < U_{Inlet}$ and $U_{Cup}^{ON} > U_{Inlet} > 0$.

III.2 Simulating ions in the gas phase

III.2.1 Parametrization

There are various studies comparing force fields [136–141], but the amber99sb-ildn [142] version used in this work appears to be a generally robust, well-refined one for peptides and proteins. Due to the IR-MALDI process, mostly singly charged peptides are observed. The ESI process also produces its own charge states, which are not always the same as in solution. Given that the Amber force fields are parametrized to reflect the charge states of peptide ions in solution, it was necessary to expand the amber99sb-ildn force field in order to reflect the observed charge states in ESI as well as IR-MALDI. New residues had to be defined in order to include N-neutral and C-neutral peptides as well as neutral arginine. For this purpose, new partial charges as well missing parameters for the bonded interaction potential terms as defined in Section II.2.3 were determined.

The charges used in Amber were originally determined through the restrained electrostatic potential (RESP) method [143]. The R.E.D.D. Server Development [143–148] automates this procedure and results in a higher reproducibility for complex systems with bonded residues (as opposed to standalone molecules where Antechamber [149,150] might be used). This is why it was chosen here for the residue partial-charge derivation. However, Antechamber still provided interaction potential parameters when those were missing. The only interaction potential in the

new residues in need of parametrization was the angle potential according to equation 11 between the sp^2 amino group N, C_α and the carbonyl C atom. This was required in order to construct the terminal neutral $-NH_2$. The obtained values were $\theta_m = 109.500\,°$ and $k_{ijk}^{\theta} = 668.959\ kJ{\cdot}mol^{-1}{\cdot}nm^{-2}$.

III.2.2 Running a molecular dynamics simulation

Peptide structures are initially drawn with Chimera 1.11.2rc [151]. The protonation sites were determined according to the relative basicities of the different amino acids and sites in the gas phase [152]. When no clear conclusion could be drawn, all of the most likely structures were used. The MD package employed was GROMACS 5.1.1 [153–155]. Before an MD simulation is run, the structure is first energy-minimized using a steepest descent algorithm. After energy minimization, the molecular dynamics simulation was run for 10 ns with a 0.5 fs time step. The general approach to MD consists of three steps: initialization, force calculation and integration of the equations of motion [156]. The initialization procedure consists of taking the starting energy-minimized structure and assigning random velocities to all the atoms, out of which atomic positions and/or velocities for a "previous time step" can be calculated. This "previous time step" is only virtual, but it's required in order to solve Newton's equations of motion at $t = 0$. The next step is the force determination through equation 5, with the parameters for the potential energy functions being dictated by the chosen force field. Finally, the movement of the atoms is simulated by solving Newton's equations of motion with either the atomic positions or their velocities, depending on the chosen algorithm. The resulting output of an MD simulation is called a *trajectory* (not to be confused with the *trajectory method*, TM, for CCS calculation). It contains all the positions, velocities and forces calculated throughout the simulation for every atom at successive time steps, also called *frames* (like the series of frames that make up a movie). Different tools can then be applied to the computed trajectories in order to study the resulting structures and transitions. An example is the root-mean-square deviation (RMSD) of atomic positions. This value relates to the average distance between the atoms of two superimposed structures and indicates how similar they are. The higher the RMSD, the more the compared structures differ from each other. Another possibility is to perform an RMSF (root mean square fluctuation) evaluation, which estimates how much the position of each individual atom fluctuates over time around its average position. Hydrogen bonds can also be computed based on the distance between donor groups (OH and NH) and acceptors (O, N), as well as the hydrogen-donor-acceptor bond angle.

Here, the MD simulations were run in vacuum (implicit solvent), with a relative permittivity of 1.000362 in order to reflect nitrogen gas (obtained by extrapolation of the data compiled in [157]), at an artificially elevated temperature $T_E = 1{,}443$ K in order to sufficiently sample the conformational space. The system was simulated without cutoffs and the thermostat used was velocity rescaling [158] (more details on the energy minimization and molecular dynamics parameters can be found in the Appendix). The high temperature ensures that the molecule will overcome potential barriers and not remain stuck in just a few potential wells (local minima of the potential function). Thus, all conformational states observed during IM measurements at 293 –

313 K will be represented throughout the simulation. While the usual approach is to subject peptides to simulated annealing before calculating the collision cross-section of several candidate structures and comparing each one to the experimental results, the approach proposed here is to use the molecular dynamics simulation trajectory as a whole, resulting in a single, averaged collision cross-section value for a peptide in the gas phase. This is possible by thermodynamic reweighting of the conformational distribution at high temperature.

III.2.3 Clustering and reweighting

From the simulation trajectory, two sets of data are extracted: on the one hand, all atomic coordinates and on the other hand all potential energy values for every available time step. A procedure was developed in MATLAB (MathWorks) and the Unix Bourne Again SHell (Bash, GNU Project) for the automatic treatment of this data. The scripts can be found in the Appendix. In every coordinate set thus obtained, redundant information is present. Consider a $-CH_3$ group. The three hydrogen atoms are equivalent and as long as the position of one is known, the other two are immediately determined. As such, not every atom is necessary to describe the molecule. For this reason, random interatomic distances are used to describe the molecule at a given time step. Several sets of interatomic distances are independently selected. These subsets put together will constitute the basis for the following operations on the peptide. The simulation trajectory is then expressed in this basis set, frame by frame. This means the trajectory is transformed from a matrix of dimension 3 with p time steps, n atoms and 3 coordinates into a matrix M of dimension 2 with p time steps and q distances. Every line vector in M represents a time step in the trajectory, expressed as a series of values corresponding to the q interatomic distances in the basis set. A moving average is then performed over k successive time steps in M in order to better bring out changes in conformation, which gives a matrix M' of size $(p + 1 - k) \times q$.

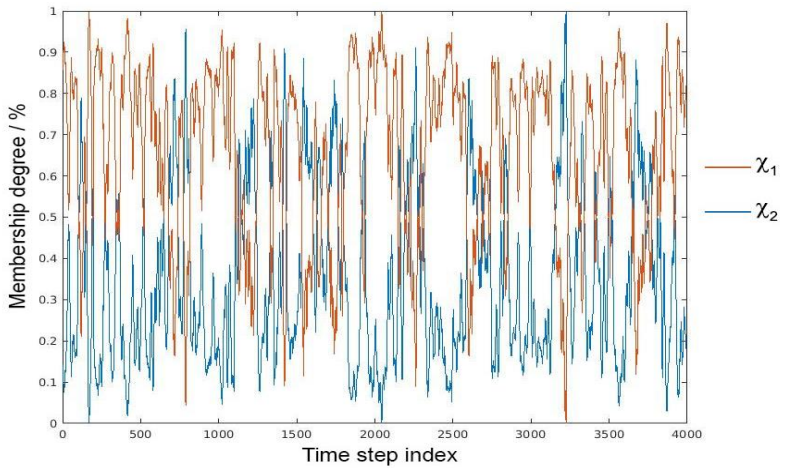

Figure 18: χ distribution of the cyclic doubly charged peptide Ac-ACTERMAAHNLCGG- NH_2

Clustering through PCCA+ (Robust Perron Cluster Analysis) [159–161] is then applied in order to find the predominant average "conformations" in M'. These correspond to m membership functions $\chi_1, \chi_2, \ldots, \chi_m$ such that every time step in M' can be expressed as a linear combination of χ functions (Figure 18). In other words, another basis change takes place, from M' to χ, a matrix

of size $(p + 1 - k) \times m$. Every conformation can be traced back to a set of k frames in the original trajectory with the corresponding atomic positions, velocities and energies. From the χ functions, the statistical distribution of states during the MD simulation at T_{E} can be determined through a simple average.

The low temperature distribution of conformations is obtained through a reweighting approach according to the extrapolation method developed by Weber et al. [162]. This method uses Helmholtz free energy differences between conformations for thermodynamic reweighting based on the partition function[7]. As the simulation corresponds to a canonical ensemble, the distribution of states follows a Boltzmann distribution. This means that for two conformations χ_i and χ_j, the free energy difference $\Delta_{ij}A$ between them can be approximated by equation 40, derived from (3).

$$\Delta_{ij}A(\beta) \approx -\frac{1}{\beta}\ln\left(\frac{\xi_i}{\xi_j}\right) \tag{40}$$

Where $\beta = 1/k_{\mathrm{B}}T$ and ξ_i/ξ_j is the ratio between the number of states in conformations χ_i and χ_j. At elevated temperature, ξ_i/ξ_j is obtained as mentioned above. $\Delta_{ij}A(\beta_{\mathrm{E}})$ is thus known. The model then establishes a relationship (equation 41) calculating the free energy difference at low temperature, $\Delta_{ij}A(\beta)$ based on the mean internal energy difference between states i and j at 0 K and at T_{E}, $\Delta U(\infty)$ and $\Delta U(\beta_{\mathrm{E}})$ respectively. The internal energy U is equal to the potential energy of the system given that the mean kinetic energy of all examined substates is identical.

$$\Delta_{ij}A(\beta) = \frac{1}{\beta}\left((\beta - \beta_{\mathrm{E}})\Delta U(\infty) + \ln\left(\frac{\beta}{\beta_{\mathrm{E}}}\right)\beta_{\mathrm{E}}\big(\Delta U(\beta_{\mathrm{E}}) - \Delta U(\infty)\big) + \beta_{\mathrm{E}}\Delta_{ij}A(\beta_{\mathrm{E}})\right) \tag{41}$$

$\Delta U(\beta_{\mathrm{E}})$ is derived from the potential energies in the simulation trajectory at T_{E} and $\Delta U(\infty)$ from the potential energy difference between the k energy-minimized representative structures of each conformation. Equation 40 is then used to determine the distribution between conformations, ξ_i/ξ_j, at low temperature.

III.2.4 Collision cross-section calculation

III.2.4.1 Molecular dynamics

The structures corresponding to each conformation are then extracted from GROMACS and used for average collision cross-section determination after format conversion with Open Babel 2.3.2 [163]. The CCS was determined through a version of the trajectory method in the MOBCAL [118,125] software which had been modified to use nitrogen as drift gas instead of helium [127]. The objective is not to determine the CCS of specific structures but a weighted value which represents the ion throughout its flight in a drift tube. First, an averaged collision cross-section value is determined for each conformation and then, after reweighting by the low temperature statistics, the average value for a given peptide ion structure is obtained.

[7] For a system in thermodynamic equilibrium, the partition function describes the distribution of states

The thus obtained CCS values were compared to experimental results obtained in our group [164] with ESI-IM spectrometry. MD values (Ω'_{MD}) systematically overestimated experimental ones (Ω_{exp}), but it was possible to apply a linear correction factor based on the singly and doubly charged peptides (Figure 19) to obtain the final Ω_{MD} values, with the standard error of the regression being 12.3 Å². This means it varies from 3 % for doubly charged RAKFKQLL to 6 % for DNDAN-NH_2. It would seem a separate correction factor could be used for triply charged peptides, but not enough data points were available.

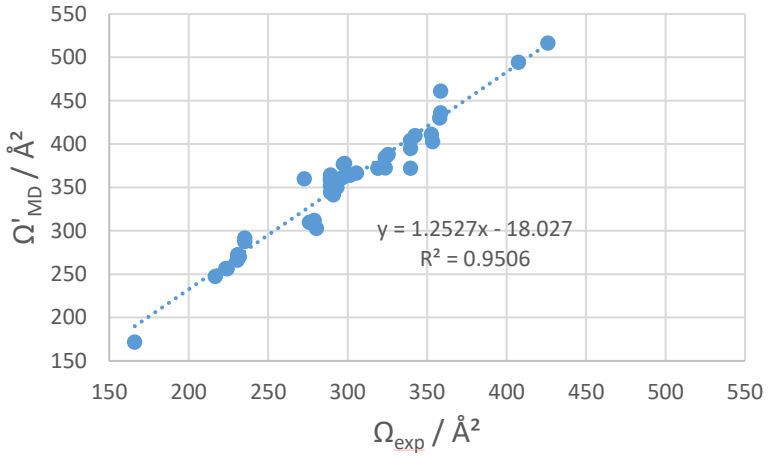

Figure 19: Correlation between MD and experimental CCS values

This method and correction are only applied to peptides. Ammonium ions were simply drawn in Chimera 1.11.2rc, energy-minimized there and then ran in the nitrogen version of MOBCAL.

III.2.4.2 Intrinsic size parameter

The corrected vales, Ω_{MD}, were also compared to Ω_{ISP}, collision cross-section values obtained through the intrinsic size parameters (ISP) method [165]. This is an empirical approximation method based on a corrected polyalanine CCS value according to equation 40. The cross-section Ω_{PA} of a polyalanine peptide of equal mass and charge as a given peptide is corrected by the influence of its structure. The correction factor depends on a parameter p_i, which quantifies the intrinsic size contribution of a given amino acid, and on n_i, the amount of times the amino acid appears in the peptide sequence.

$$\Omega_{\mathrm{ISP}} = \Omega_{\mathrm{PA}} \frac{\sum_i n_i p_i}{\sum_i n_i} \tag{42}$$

The ISP were established in helium drift gas with a large database of R- and L-terminal peptides which were obtained through tryptic digestion. The ISP set and the polyalanine regression curve which resulted in the smallest errors were used after evaluating 7 different sources [166–172]. The parameters for singly and triply charged peptides were taken from [166] and those for doubly charged peptides from [172]. The polyalanine CCS values at different charge states were taken from [168].

IV. Results and discussion

IV.1 IR-MALDI process characterization

IV.1.1 Desolvation and peak shape

The droplet source was used in combination with the atmospheric pressure spectrometer, mostly with the 5 mm-long ionization region. Tetrabutylammonium (TBA^+), a reference standard used in IM spectrometry, was chosen here as a model substance to study the influence of different parameters on a typical analyte spectrum. Observing the TBA^+ peak shape at different electric field values (Figure 20) gives some insight into the influence of the IR-MALDI dispersion process on IM spectra. Based on Section II.3.1, an ideal IM spectrometry peak is Gaussian in shape, given that its drift time will only depend on its mobility and its shape on the diffusion coefficient. Ideally, ions start out as a compact cloud which then advances through the drift tube. As the ion cloud rushes forward, transversal as well as longitudinal diffusion occur. The longer the ion packet takes to move through the drift tube, the broader it will become through diffusion. It should, however, remain Gaussian in shape, unlike the peaks which are observed in figure 20.

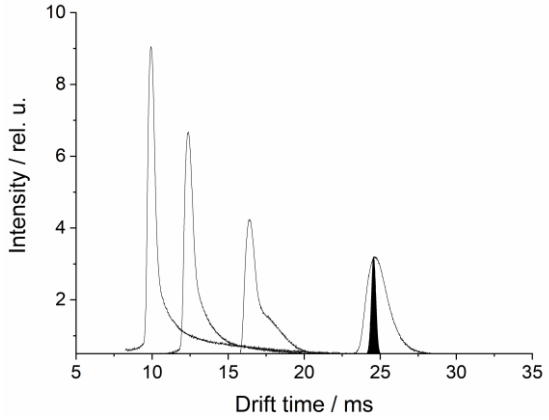

Figure 20: IM spectra (10 µM TBAB, TBA^+ ion peaks, solvent peaks removed for clarity) for different static electric drift fields. From left to right: 500, 400, 300, 200 $V \cdot cm^{-1}$); reference diffusion-broadened (filled) peak for comparison

When using a static electric field in the ionization region, every ion and charged droplet produced in the dispersion process immediately feels the influence of the electric field and starts moving towards the detector. This results in asymmetric peaks with strong tailing, as ions and droplets stemming from various stages in the dispersion process and in various desolvation states contribute to the signal. The higher the electric field, the narrower the analyte peak, the longer the tailing and the stronger its asymmetry. In fact, the peak at 200 $V \cdot cm^{-1}$ seems almost symmetric and has but a slight tailing. However, if its shape stemmed from pure diffusion broadening, it would be closer to that of the filled peak, which is a reference shape for the corresponding theoretical diffusion-broadened TBA^+ peak according to equation 20, where an infinitely narrow initial ion distribution is considered. Thus, diffusion alone is not enough to explain the broad peak shape, indicating that it must be a direct result of the initial conditions in the IR-MALDI process: this is the first sign that the initial distribution of ions must stem from a broad size distribution of dispersed droplets. A weak electric field exerts a weaker influence on the motion of ions, leaving

them more time to fully desolvate and resulting in a broad peak with low asymmetry. As the field increases, desolvated ions are extracted more efficiently, at an earlier time, and result in the main, narrow body of the peak. On the other hand, charged nano-droplets and larger aggregates are also extracted more easily at higher fields, completing their desolvation throughout their flight in the drift tube and resulting in drift times higher than those of the desolvated ion. These incompletely desolvated ions make up the tailing that is observed.

In a heated bath gas at atmospheric pressure, the evaporation of droplets produced during the dispersion of the solvent through phase explosion is enhanced in comparison to vacuum. As dicussed before, given the size distribution of droplets present in the dispersion plume, it takes them different times to evaporate and produce free ions. A static field results in tailing through the constant action of the electric field on ions which desolvate at different stages, from different droplet sizes. In order to provide the same temporal starting point for the ions and reduce tailing, they were first produced in a field-free ionization region and then introduced into the drift region by applying an electric pulse. The pulse comes at a given delay (PD) in regard to the laser pulse and has a certain width (PW) and a certain value, or amplitude (PA). Here the pulse amplitude was applied so as to keep the electric field linear throughout the spectrometer as in the static field experiments. The laser spot was focused on the bottom of the droplet produced at the tip of the metal capillary (Figure 14, right). A very large pulse width was used to ensure only the influence of the pulse delay, i.e. the desolvation time, had an influence on the peak tailing.

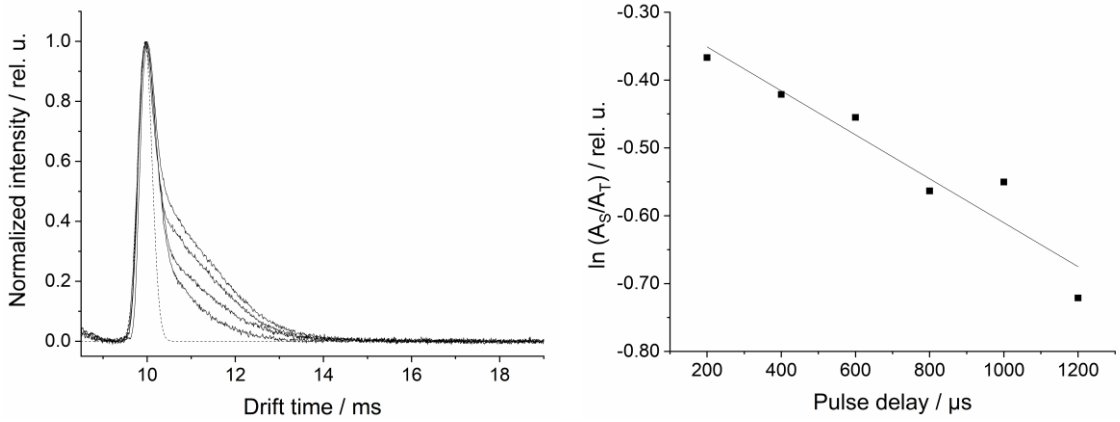

Figure 21: Left: Decrease in the tailing of intensity normalized TBA⁺ peaks with a fixed 6 ms pulse width and increasing pulse delay, top to bottom: PD = 200, 600, 1,000, 1,200 µs, ideal Gaussian peak shape overlaid as dotted line. Right: Dependence of the solvated ions fraction (solvation area/total peak area, A_S/A_T) on the pulse delay for the determination of the desolvation kinetics: 1st order reaction, with a rate constant k = 324 ± 50 s^{-1}

Peak tailing was directly compared between TBAB spectra by normalizing the intensity of the analyte peak (Figure 21, left). A Gaussian function was then fitted to the rising edge of the TBA^+ peak (dotted line) and the area of the resulting theoretical peak was used as reference for desolvated ions. Integration of the experimental peaks for every spectrum gives the total peak area A_{T}, corresponding to both solvated and desolvated ions. It is assumed that only the initially desolvated ions contribute to the symmetric, Gaussian part of the peak and that only the initially solvated ones are responsible for the tailing. A simple subtraction gives the peak area corresponding to solvation, A_{S}. Assuming that at 443 K desolvation is thermodynamically favored and that the ratio of desolvated to solvated ions is not altered by other phenomena such as ion

loss or diffusion, the fraction of solvated ions A_S/A_T, which is a function of time, can be used to study the desolvation process kinetics. Figure 21 (right) enables the determination of a first order rate constant, $k = 324 \pm 50\ s^{-1}$ with an initial solvation ratio $(A_S/A_T)_0 = 75 \pm 3$ % such that:

$$\frac{A_S}{A_T} = \left(\frac{A_S}{A_T}\right)_0 e^{-kt} \tag{43}$$

First order desolvation kinetics imply that the desolvation rate depends linearly on the solvation ratio. The half-life of equation 43 is 2.1 ± 0.3 ms, meaning it would take 6.4 ± 0.9 ms to fall below 10 % solvation. Given that these values are in the same order of magnitude as the drift times of the analyte ions, it is unlikely that this value can be reached before ion losses become significant and the peak width increases due to diffusion broadening. Indeed, over 1 ms (between PD 200 and 1,200 µs), the raw area of the Gaussian peaks corresponding to desolvated ions has already dropped by 61 %.

Furthermore, for PD $\approx t_d$, the diffusion in the ionization region during desolvation will be almost equal to the diffusion broadening of the ion cloud during its drift. This would translate into an increase of t_{diff} in the initial ion cloud width, approximated by t_g. According to equation 22, after a desolvation time $PD \approx t_d$, the increase in peak FWHM $\Delta\omega_h$ would thus be

$$\Delta\omega_h = \sqrt{t_{diff}^2 + \left(t_g + t_{diff}\right)^2} - \sqrt{t_{diff}^2 + t_g^2}. \tag{44}$$

If PD $\approx t_d$, for an infinitely narrow initial ion distribution, $t_g = 0$ and $\Delta\omega_h = 0.41 t_{diff}$, meaning a 41 % increase in peak broadening due to diffusion alone, no matter the initial ion. Figure 22 shows that if $t_g > 0$, the increase in FWHM will be a monotonously increasing function of t_g which reaches an asymptotic value.

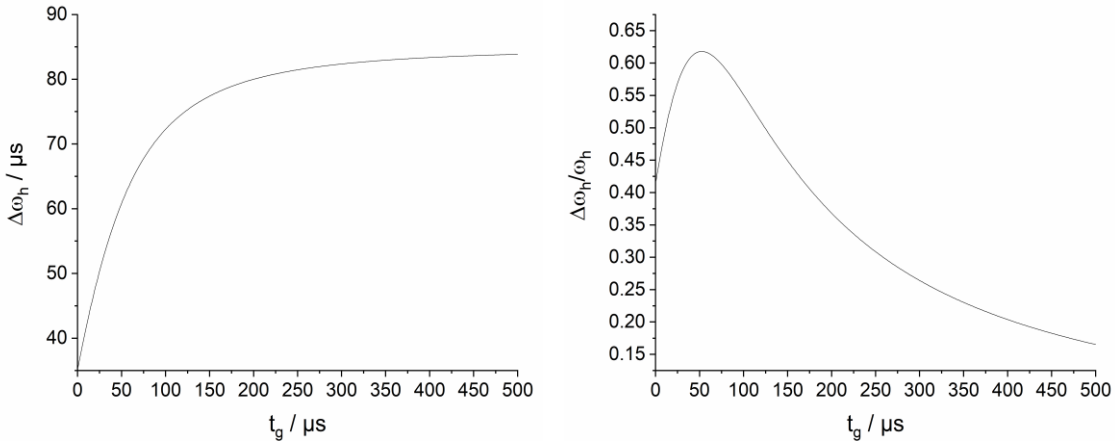

Figure 22: Absolute (left) and relative (right) increase in the FWHM of the TBA⁺ peak due to the pulse delay as a function of t_g when PD $\approx t_d$

However, the relative increase in FWHM, $\Delta\omega_h/\omega_h$ is a function of t_g which goes through a maximum for $t_g > 0$ and PD $\approx t_d > 0$, when

$$\frac{\partial(\Delta\omega_h/\omega_h)}{\partial t_g} = 0, \tag{45}$$

with

$$\frac{\partial(\Delta\omega_h/\omega)}{\partial t_g} = \frac{\left(t_{diff} - t_g\right)^3 + t_g\sqrt{t_{diff}^2 + t_g^2}\sqrt{\left(t_{diff} + t_g\right)^2 + t_{diff}^2} - 6\,t_{diff}\,t_g^2}{\left(t_{diff}^2 + t_g^2\right)^2\sqrt{t_{diff}^2 + \left(t_{diff} + t_g\right)^2}}. \quad (46)$$

Equation 45 was numerically solved for $t_g \approx 0.399\,t_{diff}$, where 0.399 is the only root of the polynome $4\,x^5 + 12\,x^4 + 14\,x^3 + x^2 - 6\,x + 1$ which satisfies the problem.

Equation 44 can be generalized to include the contribution of any PD to peak broadening, t_{PD}:

$$\Delta\omega_h = \sqrt{t_{diff}^2 + \left(t_g + t_{PD}\right)^2} - \sqrt{t_{diff}^2 + t_g^2}. \quad (47)$$

Both $\Delta\omega_h$ and $\Delta\omega_h/\omega_h$ were plotted as a function of PD and t_g in figure 23, where it is visible that the FWHM of the TBA⁺ peak will increase more slowly with increasing PD when t_g is low, i.e. when the initial ion cloud is more compact. For the 6.4 ± 0.9 ms PD needed to fall below 10 % solvation according to equation 43, an infinitely narrow ion cloud ($t_g = 0$) would already result in a peak that is 14 % (12 µs) broader.

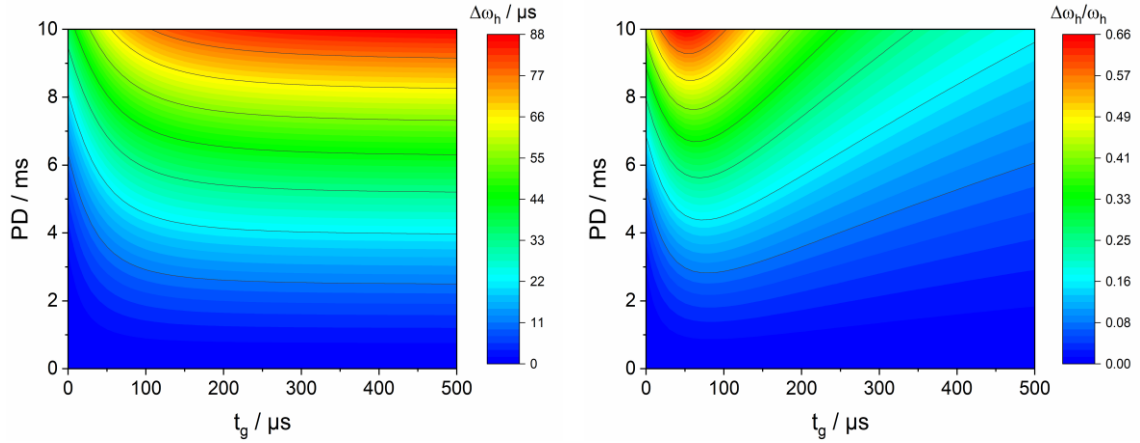

Figure 23: Absolute (left) and relative (right) increase in the FWHM of the TBA⁺ peak due to the pulse delay as a function of t_g and PD

IV.1.2 Transport mechanisms in IR-MALDI IM spectrometry

As discussed above, the product of a laser impact on a surface is an ablation plume which rises orthogonally to it. According to the specific spot on the droplet surface where the laser is focused, IM spectra can vary in shape and intensity. This means that it is not only the size distribution of the produced droplets that is relevant, but also their spatial distribution and velocity vector. With a round surface such as that of a droplet, the plume can actually take one of numerous orientations. Figure 24 shows a few examples of IM spectra obtained from different droplet surface regions, under static and pulsed ionization region voltages, and the corresponding droplet pictures at the tip of the capillary.

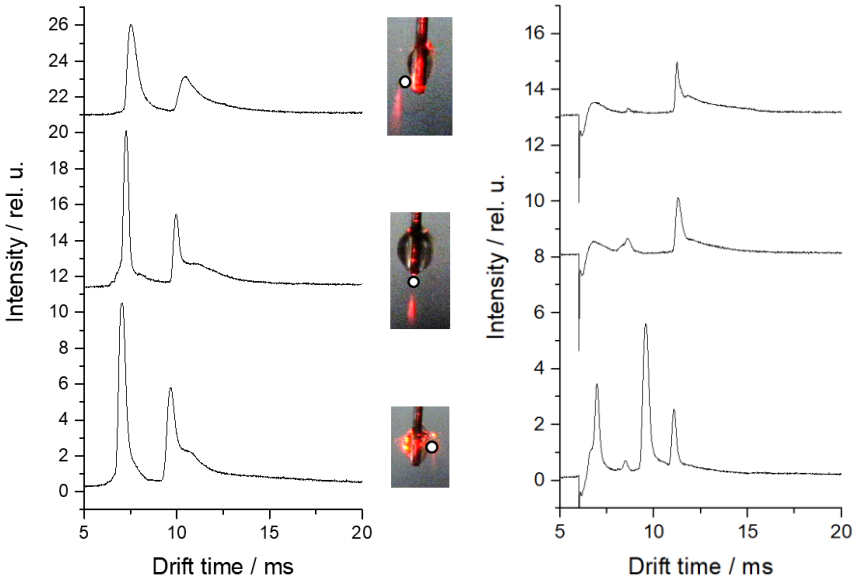

Figure 24: TBAB spectra from different regions on the droplet surface, taken at E = 500 V·cm^{-1} electric field. Left spectrum: static field. Right spectrum: pulsed ion injection, PD = 1.5 ms, PW = 4.5 ms. The negative peak at the beginning is an artifact of the electrical pulsing. The laser was shot from the front onto the spot marked in white and the drift tube inlet was located to the right of the pictures

The red color in the pictures comes from the adjustment diode of the IR laser. Near the impact spot, marked in white, some light scattering is observed. This is consistent with the presence of small droplets due to the liquid dispersion phenomenon. The inlet of the spectrometer was to the right of the capillary and the laser was shot from in front. The peaks in the spectra correspond to the cluster ion of acetonitrile and water at lower drift times and to TBA^+ at higher drift times. The spots correspond, from bottom to top, to a spot on the right of the droplet, one below it and one to the left.

Two trends were observed during the mapping of the droplet in a static field (Figure 24, left). On the one hand, the drift times show a slight shift with regard to each other, decreasing as the spot moves towards the right: as the ions are produced closer to the detector, the drift time shortens accordingly. On the other hand, as the spot moves to the left, the intensity and the area of the peaks decrease while their asymmetry becomes more pronounced.

Table 1: Parameters regarding the TBA^+ peak under static field conditions and at different laser spot positions corresponding to those in figure 24 under static field conditions

	Left	**Below**	**Right**
Drift time (ms)	10.45	9.96	9.66
Intensity (rel. u.)	1.96	3.82	5.21
Area (rel. u.)	3.03	3.78	7.17
A_S/A_T	0.56	0.69	0.69

The ratio A_S/A_T, calculated as above from the areas of normalized peaks, is lower for the left position while staying comparable for the other two, indicating that the peak shape is not actually a direct product of solvation alone. The rate of 69 % is lower than the above determined $(A_S/A_T)_0$ of 75 %. The difference might stem from ion losses and diffusion phenomena, which could partially

influence the solvation rate measured under pulsed conditions. The values remain, however, in good agreement. The summary of the different parameters is given in Table 1.

As for the drift time, the changes in peak shape could be partly related to the starting position of the ion cloud, through diffusion, but it seems unlikely that the effect would be so large. In fact, the pulsed experiments (Figure 24, right) hint towards a more complex phenomenon. The spectra on the right were taken with a pulse delay of 1.5 ms and a large pulse width (4.5 ms) but were not resynchronized with the electric pulse. Accordingly, the drift times appear to be ~1.5 ms longer than with a static field and the solvent peaks have largely disappeared through desolvation. However, when hitting from the right, two additional peaks appear. Two of them correspond to the same ions at their proper drift times (i.e. their drift times in the static field spectra on the left) and the other two to their delayed times (+1.5 ms): the broad peaks have actually split into two narrower ones, showing that there are two transport effects at play and that they have been effectively decoupled through electric pulsing. Shadowgraphy experiments (Figure 25) shed some light on this phenomenon by visualizing the ablation plume. As expected from the literature, the phase explosion projects ions and dispersed liquid droplets in a direction which is orthogonal to the droplet surface. Thus, when hitting the droplet on the right, the IR-MALDI process projects ions and droplets along the drift axis towards the drift tube, which is not the case for the other positions. This means that first, ions are transported by the momentum gained through the phase explosion process until they reach the drift tube and feel the influence of the electric field. There, they are already drifting towards the detector when a second set of ions, possibly stemming from a later stage in the dispersion process, is electrically pulsed into the drift tube. The fact that the peaks merge into one under static conditions is a first indication that both average transport velocities (electrical and phase explosion-induced) are in the same order of magnitude over the considered distance. The existence of these two separate ion transport mechanisms is the reason why peak splitting is only observed when hitting from the right and can also be the reason why the peak intensity and area at this position are much higher than the others: the main velocity components point towards the drift tube (along $\vec{z}$), enabling more droplets and ions to go into it. In the case of the left position, the main velocity component points toward the opposite direction (along $-\vec{z}$), resulting in a weaker signal. The lack of a narrow initial peak can be due to the ions starting out along $-\vec{z}$ because of the dispersion mechanism before being decelerated by the electric force and reversing direction, effectively "smearing" the peak over a wide range. This competition between dispersion velocity following $-\vec{z}$ and electric force along $\vec{z}$, concurrent with progressive desolvation of different droplet sizes, results in a broad, largely asymmetric peak. This position has a higher desolvation ratio value, but it should be noted that the calculation of the solvation ratio is based on the existence of a narrow peak followed by tailing only due to the late desolvation of larger droplets. Here, the peak obtained from the left position does not seem to fulfill these requirements due to the complexity of the initial conditions. Due to these conditions and to the weaker signal obtained in this position, the other two spots were favored in this work. The position on the right of the droplet – referred to as region 1 – was used to study the dispersion process, given that its influence is clearly visible on IM spectra in the form of doubled peaks. The bottom position, where the ablation plume had no component along $\vec{z}$, resulted in spectra with straightforward interpretation and good signal response, where static and pulsed experiments

could be directly compared. This is why the bottom position – referred to as region 2 – was chosen for spectrometer optimization and analytical applications. Both regions and their respective ablation plumes are shown in figure 25.

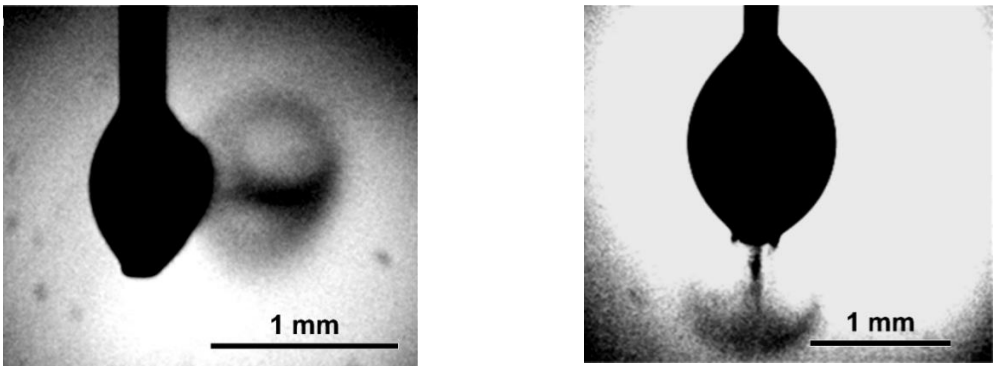

Figure 25: Shadowgraphy images illustrating the general direction of the IR-MALDI dispersion plume in region 1, 12 µs after the start of the phase explosion (left) and in region 2, 7 µs after the start of the phase explosion (right). The IM drift tube is to the right of the picture, the laser was shot from the front

The effect of laser power variations on the peak ratios is further evidence that the peak splitting is due to the decoupling of electrical and phase explosion transport. In figure 26, left, as the initial laser pulse power decreases, so do the intensity and area of the peak at lower drift times. As the power decreases, so does the transport efficiency of the phase explosion. Consequently, the earlier peak drops in intensity and area with the laser power. The peak originating from the electric pulse seems virtually unaffected, indicating that the desolvation rate of the corresponding droplets is only weakly dependent on the phase explosion conditions. A look at the right graph in figure 26 also suggests that the ion release process for the later peak is more efficient than for the first peak, which is concentration dependent. The concentration variation in this figure is only qualitative and stems from sample injection into the solvent flow with a valve. An elution profile is thus created through sample diffusion at its edges as it advances within a flow of solvent.

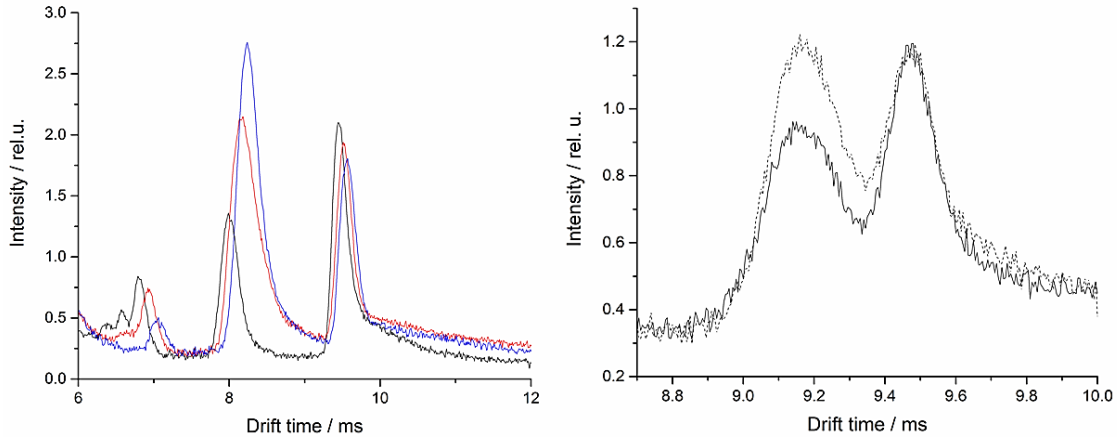

Figure 26: Left: IR-MALDI-IM spectra of 10 µM TBAB for different pulse energies (black: 3.04 mJ, red: 4.41 mJ, blue: 5.77 mJ), PD = 1.5 ms, PW = 4.5 ms. Right: IM spectra of 5 µM TBAB (dotted line: maximum of concentration, solid line: low concentration), PD = 420 µs, PW = 4 ms. Both spectra acquired from region 1 at E = 500 V·cm^{-1}

The plumes in figure 25 have a mushroom-like shape, which means that the laser fluence used in these experiments is close to the ablation threshold, as discussed in Section II.1.2.5. The fluence can be calculated by taking the spot size, the laser pulse energy and the minimum reflectivity and

transmissivity of the gold mirrors and the lens in the system. In the case of figure 25, at peak laser power (6 mJ), the laser fluence is about 1.8 J·cm^{-2}. The ablation threshold for ACN/H_2O 1-1 can be very roughly estimated to be between 0.6 and 0.9 J·cm^{-2} from the spectra at different laser pulse energies in figure 26, left, and the fact that there was a lack of signal at 2 mJ. This confirms that the laser fluence used in these experiments is close to the ablation threshold.

IV.1.3 Velocity measurements

IV.1.3.1 Shadowgraphy and initial velocity

Various experiments were used in order to measure the average velocity of the ions produced by the dispersion phenomenon at different time scales. The first was stroboscopic shadowgraphy, which makes it possible to see the dispersed droplets originating from the phase explosion process. A picture was taken at regular intervals by adjusting the delay between the laser pulse and the diode trigger signal. The distance between the origin of the plume and its front was then measured and reported as a function of the time since the beginning of the process (Figure 27, left).

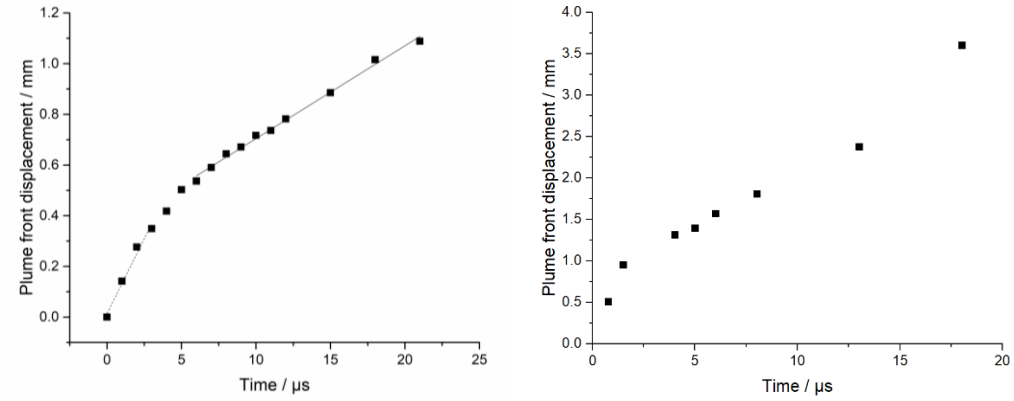

Figure 27: Left: displacement of the ablation plume front along the IM spectrometer axis as a function of the time since the beginning of the process. Solvent: ACN/H_2O 1-1. Laser fluence: 1.8 J·cm^{-2}. Laser pulse duration: 7 ns. Right: Plume front displacement extracted from image treatment of ref [79] *for 0.12 J·cm^{-2}, pure water and a 70 ns Er:YAG laser pulse*

A strong deceleration is immediately visible. In order to characterize it, the curve was fitted with two linear functions, the slope of which can give an estimation of the expansion velocity of the plume at different timescales. The initial velocity, averaged over the first 3 µs, is 118 ± 12 m·s^{-1}. After a rapid expansion, it quickly loses speed until it reaches a constant velocity of 37 ± 1 m·s^{-1} after 6 µs. The initial velocity value is in good agreement with other values obtained in our work group through high speed shadowgraphy [173]. The velocity of this plume front was determined in ACN/H_2O 1-1 at a fluence of 1.8 J·cm^{-2} and it is much lower than that of the plume obtained by Apitz and Vogel at 0.12 J·cm^{-2} for pure water in [79]. A quick image treatment of their data gives a rough estimate of the general trend: the velocity decays slightly faster (somewhere between 1.5 µs and 4 µs) but remains approximately up to four times higher (Figure 27, right). This is to be expected since a lower water fraction results in a less vigorous ablation. This was intuitively confirmed in the present work, given that the solvent ACN/H_2O 1-1 was chosen as a compromise between signal intensity and background noise in the form of droplets, a sign of a stronger

ablation process. After 25 µs, or about 1.1 mm away from the ablation spot, the dispersion plume thins out and a clear front is not visible on the images anymore. For this reason, the velocity could not be followed over a longer period of time. In order to access the velocity of the ions after this point in time and space, ion mobility measurements were used.

IV.1.3.2 Ion mobility spectrometry for the study of ion velocities

Two different ion mobility experiments were used to study the mean ion velocity at different time scales: a time-resolved experiment and a distance-resolved experiment.

In the time-resolved experiment, the objective was to measure the time that it takes the ions transported by the phase explosion to reach the inlet of the drift tube (more precisely the metal mesh placed on the first drift ring). In order to achieve this, the time that it takes for the TBA^+ peak to split, i.e. for the two transport phenomena to decouple, was measured. If a second peak is visible, it means that the first ion packet has already left the ionization region as the second one is pulsed towards the drift region. If only one is visible, it means that the two ion packets overlap, and thus that the first one was still crossing the ionization region as the electrical pulse was applied.

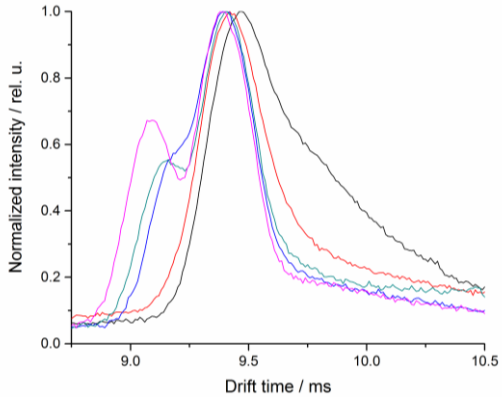

Figure 28: Time-resolved IM experiment. Normalized TBA^+ ion peaks for different pulse delays (black: 60 µs, red: 180 µs, blue: 300 µs, dark cyan: 340 µs, magenta: 420 µs) at PW = 400 µs (region 1), E = 500 V·cm^{-1}

The pulse delay was progressively incremented from 0 to 420 µs in figure 28 in order to determine the moment when the peaks split. At 340 µs, a second peak can be clearly observed but at 300 µs a shoulder is already visible. The distance between the capillary and the inlet mesh being 4.5 ± 0.5 mm, the average velocity can be estimated to be 15 ± 2 m·s^{-1} over the first 300 µs, or up to 4.5 mm away from the capillary tip.

The second velocity determination method was the distance-resolved experiment. The distance between the repeller plate and the inlet of the drift tube was set to 10 mm instead of 5 mm. The inlet mesh was 2 mm into the first drift ring, which results in the capillary-mesh distances presented in figure 29. The spectrometer was mounted on a translation stage for precise movement around the capillary. The optical path, the focus point, the droplet and the capillary itself all stayed static. This provided identical starting conditions for the ions, for every spectrum presented in figure 29, left. As the capillary moves further away from the inlet grid, there is a

progressive disappearance of the plume transport peak, which means more inefficient transport at higher distances, no doubt through ion losses and radial diffusion. There is also a systematic shift in drift times with varying distances. By plotting both peak positions as drift times (i.e. time since elapsed since the laser pulse for the first one and the time since the electric pulse for the second one), figure 29, right is obtained. The first interesting observation is that at a distance of around 4.5 mm, the drift time of the shockwave-transported ions (first peak, solid symbols) as well as those transported by the electrical pulse (second peak, open symbols) are the same. This explains why under static conditions, in the regular configuration of the spectrometer, both peaks merge into one: the average velocity of their respective ion clouds over the specific capillary-mesh distance used is the same. This also validates the approach in the time-resolved IM experiment, since the two ion clouds are moving with the same velocity at 4.5 mm away from the mesh.

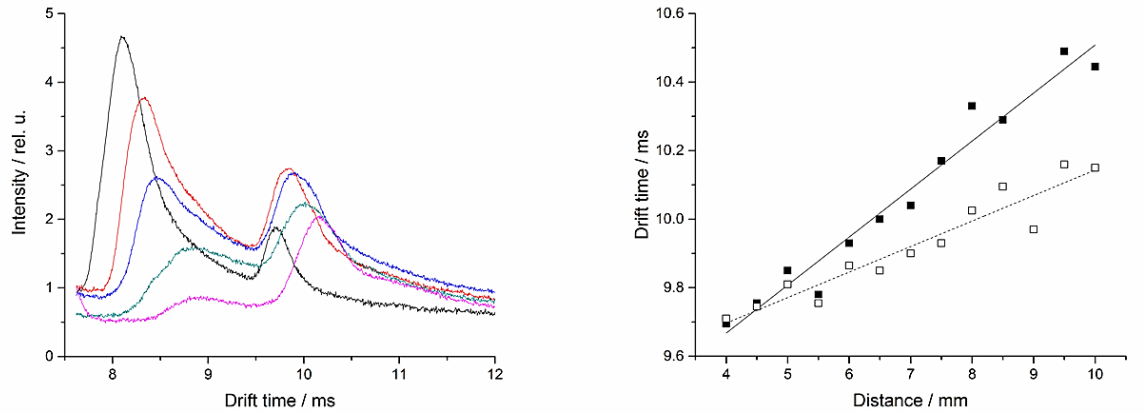

Figure 29: Distance-resolved IM experiment at 500 V·cm^{-1} Left: IM spectra for different net-capillary distances (black: 4 mm, red: 6 mm, blue: 7 mm, dark cyan: 8 mm, magenta: 10 mm), PD: 1.6 ms. Right: peak position as a function of the mesh-capillary distance for the shockwave induced peak (solid symbols and line), and the electrical transport peak (dotted line and open symbols, drift time corrected to account for PD)

What is measured here as the drift time t_{d} is the sum of the time the ions spent in the drift tube, t_{DT}, plus the time they spent in the ionization region t_{IR}. By writing t_{IR} as a function of the average ion velocity in the drift region, v_{IR}, and the distance between capillary and inlet grid, d, a simple relation can be established (48). Ions arriving at the inlet grid are assumed to move through the drift tube only through the effect of the electric field, thus making t_{DT} a constant.

$$t_{\mathrm{d}} = \frac{1}{v_{\mathrm{IR}}} d + t_{\mathrm{DT}} \tag{48}$$

A linear regression was applied to the drift times of each peak. Velocities of 7.1 ± 0.5 m·s^{-1} and 13.4 ± 1.3 m·s^{-1} were obtained for the shockwave and electrically transported ions, respectively. The expected drift velocity of TBA^+ ions at 443 K, atmospheric pressure and an electric field of 500 V·cm^{-1} is 10.8 m·s^{-1}. The velocity of the electrically transported ions is a bit higher than this theoretical value but still within an acceptable margin, considering the uncertainty regarding the measurement of the different system variables is only roughly estimated. The intercept of both curves is not in agreement, although it should correspond to t_{DT}, a constant. A linear regression was applied to the drift times of the plume transport peak, but it must not be forgotten that the drift velocity of the corresponding ions is indeed not a constant. As the experiments above showed, the velocity of the plume is a rapidly decaying physical quantity. For this reason, an

extrapolation to 0 mm cannot be carried out for the plume transport regression curve. In the considered range of 4-10 mm however, the velocity decay is small enough for the velocity to be approximated by a constant. The decrease in the magnitude of the velocity decay can be observed in figure 30, which summarizes the results of the different experiments.

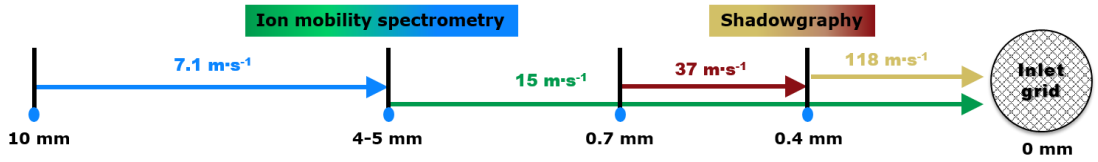

Figure 30: Summary of the average ion and droplet velocity measurements at different scales. The velocity rapidly decays with the distance from the capillary tip, represented with a droplet of solution

IV.1.4 Anatomy of the dispersion plume

The mechanism of the dispersion process is determined by the fact that the fluence is close to the ablation threshold. In this regime, first non-equilibrium mass transfer occurs (light vaporization), followed by phase explosion, which creates an audible shockwave. An ablation plume then projects droplets of various sizes through the ambient air. Its shape is that of a piston moving forward and rolling clouds around it, created by the friction with air. The last stage of the process is larger droplet emission through the recoil effect.

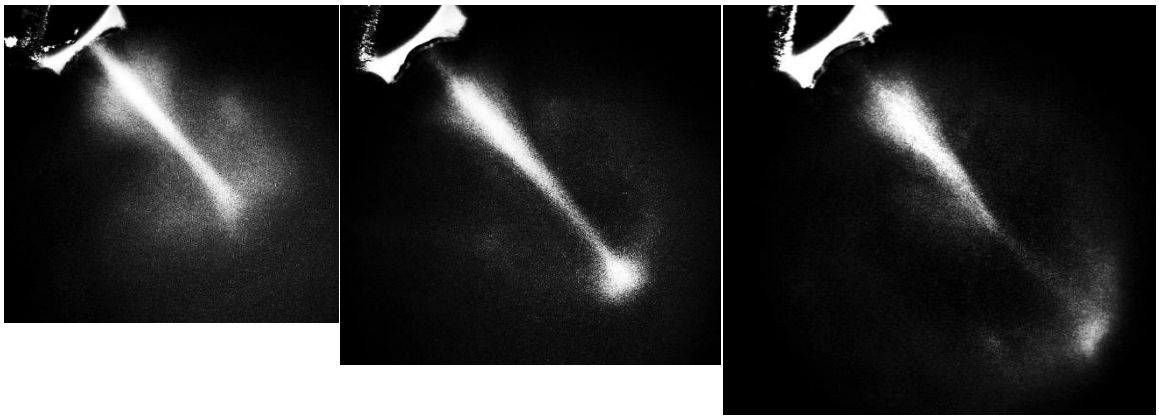

Figure 31: Inverted color shadowgraphy images of the dispersion plume for an ACN/H_2O 1:1 mixture. From left to right: 8.8, 13.9 and 22.7 µs after the beginning of phase explosion

Given 1) that phase explosion is a much more efficient transport mechanism than surface vaporization, especially near the ablation threshold [69], 2) that the fraction of ions in surface vaporization is small and 3) that the late stage ablation through the recoil effect produces mostly no ions and large droplets (which would desolvate poorly [174]), both peaks are proposed to stem from phase explosion. The plume created in these experiments has been observed to have a thick front followed by a rarefaction zone, corresponding to the formation of a toroidal cloud, and a trailing section with much lower velocities [79,173]. This can also be observed in figure 31, where the front of the ablation plume and the mushroom cloud is seen expanding in a forward direction and leaving behind a trailing cloud of droplets 8.8, 13.9 and 22.7 µs after the beginning of the phase explosion for a mixture of ACN/water 1:1. The shape of the trailing cloud is reminiscent of

a *bell* (also called *skirt*) which is a phenomenon occurring during the ascent of nuclear mushroom clouds. They originate when the column goes through a layer of air which is supersaturated with water. The lower pressure of the fireball following the overpressure of the advancing shockwave triggers condensation, forming droplets which are taken up by the ascending column. A layer of super saturated vapor is produced in the first stage of the ablation process, and condensation has been observed by Takamizawa et al. after 10 µs with a 10 ns laser pulse of 300 mJ at 1.9 µm, but the droplets produced are in the micrometer range [83]. The recoil effect can also be seen to play a role in the formation of larger droplets, seen as tendrils extending outwards from the crater in figure 32. It is however unlikely that large droplets would result in free gas phase ions.

Figure 32: Shadowgraphy images of the dispersion plume for an ACN/H_2O 1:1 mixture at 8 µs after the beginning of phase explosion

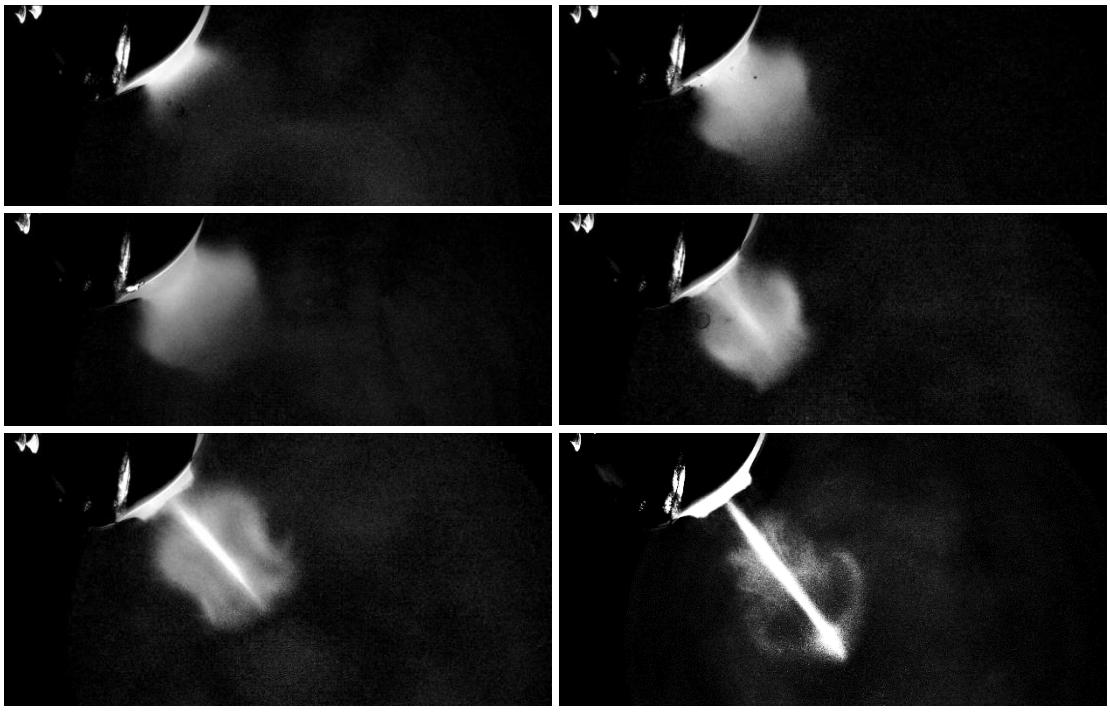

Figure 33: Inverted color shadowgraphy images of the dispersion plume for a 100 mM NaCl solution in ACN/H_2O 1:1. From left to right, top to bottom: 1, 2, 2.5, 4.5, 5.5, 8 µs after the beginning of phase explosion

What figure 33 shows is that the skirt results from fluid dynamics and the interaction with ambient air. Apitz and Vogel have previously described the early stages of plume expansion [79]. First, a spherical plume expands outwards. It collides against ambient air, causing a reflected shockwave in the opposite direction to the propagation direction, which momentarily suppresses the plume. This is seen as flattening of the plume at 2.5 µs in comparison to 2 µs. Then, the forward motion starts to dominate again, creating ring turbulences and a toroidal cloud. The transition from 4.5 µs to 8 µs shows that the rising column of vapor and droplets then advances through the initial cloud, piercing it at 5.5 µs and dragging its center along with it in the propagation direction. The skirt then forms out of this initial cloud and the new toroidal cloud resulting from further interaction with ambient air, as seen at 8 µs.

From the desolvation experiments, the observation of peak splitting and the peak ratios at different laser powers and concentrations, combined with shadowgraphy experiments and velocity measurements, it can be concluded that:

1. Phase explosion produces ions with enough momentum to transport them into the drift tube without the presence of an electric field.
2. These ions form their own compact cloud, as they result in a narrow peak: they have their own defined spatial distribution. This corresponds to the front of the plume separating from the tail.
3. The ions which result in the electrical pulse peak stem from slower droplets at the back of the ablation plume and follow first order desolvation kinetics. They do not possess enough momentum to make it into the drift tube on their own.
4. While the dispersion process itself is sensitive to laser energy, ion production from the slower droplets still leads to reproducible results, indicating a stable desolvation rate. For the droplets at the head of the plume, the desolvation process might not be as efficient, thus making the ion yield more sensitive to laser power and to concentration. This might be due simply to the fact that the droplets at the back of the plume have had more time to desolvate than those at the front, though a higher temperature cannot be excluded.

IV.2 Spectrometer optimization

IV.2.1 Atmospheric pressure IM spectrometer

The previous section focused on the dispersion phenomenon. It was shown that when using pulsed ion injection, the reproducibility of the peak stemming from electrical transport was high due to efficient desolvation. This section will focus on the improvement of the spectrometer through pulsing and on finding the optimal parameters for an analytical application. Through the desolvation kinetics experiments, the influence of the pulse delay was already partly shown. Optimal pulsing parameters (pulse amplitude, width and delay) can in fact lead to narrow peaks, ideal for analytical applications such as in figure 34. Particular attention will be given to peak shape and sensitivity. As was said above, region 2 on the droplet was chosen for this purpose and acetonitrile-water 1:1 was used as a solvent.

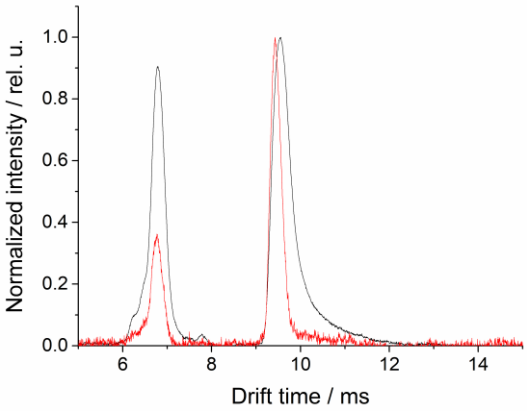

Figure 34: Normalized IM spectra of a 5 µM solution of promazine at 500 V·cm^{-1} under static conditions (black) and optimized pulsed conditions (red), PD = 500 µs, PW = 300 µs. Peaks from left to right: solvent peak and TBA$^+$ peak

The influence of pulse delay on the resolution of the spectrometer as well as on its overall response was studied with TBA$^+$ ions in figure 35. Although pulse delay helps with peak shape and resolution by improving desolvation and reducing tailing (see Section IV.1.1), the peak area steadily drops at higher delays. The mean values with their standard error in a series of three measurements are reported. The drop in signal response is due to increased ion losses through spatial dilution of the initial ion cloud by diffusion, which was previously discussed, and interaction with the heated bath gas in the ionization region. The latter also results in a drop in resolution at high pulse delays, overtaking the initial improvement due to higher desolvation. The resolution is defined as the drift time divided by the FWHM.

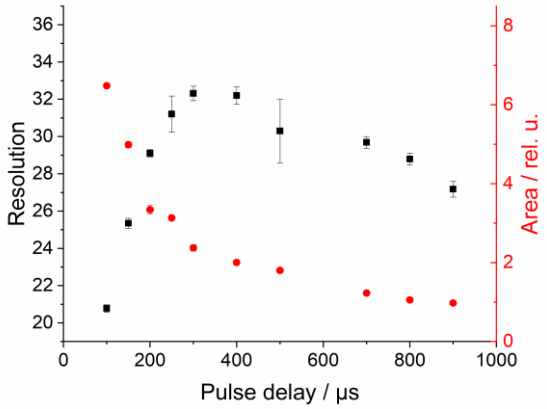

Figure 35: Influence of the pulse delay on the TBA$^+$ peak resolution and area for a 1 µM TBAB solution. E = 500 V·cm^{-1}, PW = 3.5 ms, PA = 2 kV·cm^{-1}

The influence of the pulse amplitude, which is in fact the strength of the electric field in the ionization region, was also studied in figure 36 with TBAB. The resolution first increases with the PA (graph on the left), and the solvation ratio A_S/A_T decreases (graph on the right). This is due to the narrowing of the initial ion cloud with increasing field strength and the reduction of tailing. However, after a resolution maximum, the solvation ratio begins to steadily increase once more (along with the FWHM, not shown) and the resolution drops. This is due to the more efficient extraction of larger charged nano droplets, which contribute to tailing. Furthermore, there is a visible drop in peak area with higher pulse amplitudes, which is due to a higher number of ions

getting discharged at the inlet grid. The same effect has been characterized in corona discharge ionization IM spectrometry [175] when the electric field in front of the grid, here in the ionization region, is much higher than behind it, i.e. in the drift region.

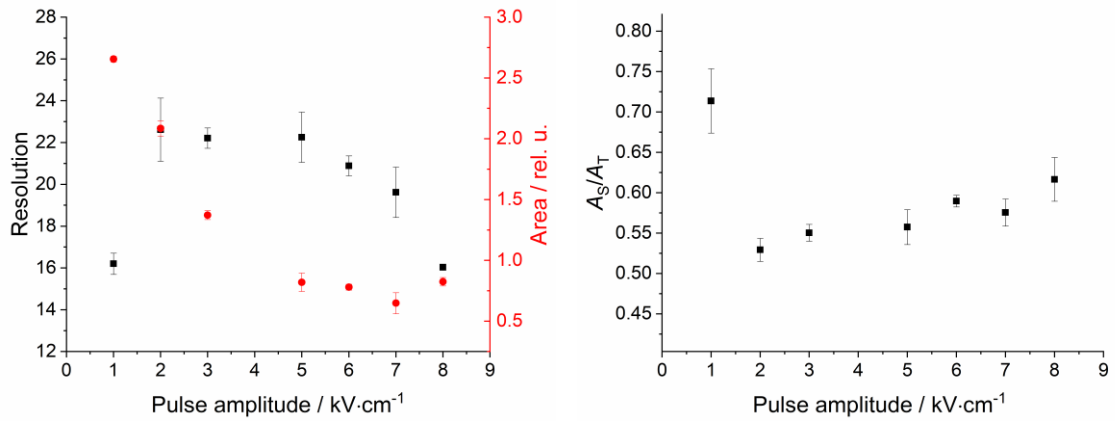

Figure 36: Influence of the pulse amplitude on the resolution and the raw area of the TBA⁺ peak (left) and on its solvation ratio (right) for a 1 µM TBAB solution. E = 500 V·cm^{-1}, PD = 300 µs, PW = 3 ms

Finally, the influence of the pulse width on the TBA$^+$ peak was also investigated. In this case, the peak area goes through a minimum with varying PW (Figure 37, left) which is unlike the monotonous decrease observed with increasing pulse delay and amplitude. Low resolution corresponding to high peak area is observed at the lowest pulse width, 150 µs, and corresponds to long tailing (Figure 37, right). At 4.0 kV·cm^{-1} PA, the voltage difference between capillary and inlet grid is 1 kV. At 443 K and atmospheric pressure, the theoretical drift velocity of TBA$^+$ ions (K_0 = 1.33 cm^2·V^{-1}·s^{-1} [176]) at that PA is 48.0 m·s^{-1}. It would thus take a TBA$^+$ ion 94 µs to cross the 4.5 mm between the capillary tip and the inlet grid. Given that the ion cloud has a certain spatial and temporal width, and that the PA switch from 0 to 4 kV·cm^{-1} is not instantaneous, 94 µs can be seen as the time it would take the front of the ion cloud (the fastest possible ions) to reach the drift tube. If PW < 94 µs, no ions can be detected.

Figure 37 (right) shows that both one of the highest peak resolutions and the most symmetrical peak shape are observed at 250 µs PW. This corresponds to a Gaussian ion density distribution (symmetric ion cloud), which means that the initially desolvated ion cloud would need between 94 µs for the first ions and 250 µs for the last ones to cross into the drift tube, resulting in a temporal ion cloud width of 156 µs. This means that if 94 µs < PW < 250 µs, the ion cloud will not have been entirely extracted by the time the electric pulse is over. When the PA switches from 4 to 0 kV·cm^{-1}, one fraction of the ion cloud is already in the drift tube. It will experience friction with the gas and a Coulomb force, resulting in a net force along $\vec{z}$ that will propel it towards the detector. The other fraction, still in the ionization region, continues to move towards the drift tube due to the momentum gained when PA = 4 kV·cm^{-1} but experiences a decreasing Coulomb force during the switch from 4 to 0 kV·cm^{-1} (which is not instantaneous). Finally, PA = 0 kV·cm^{-1} and the ion cloud fraction only experiences friction with the neutral gas, which results in a net force along $-\vec{z}$. This force leads to a progressive loss of momentum, i.e. to the deceleration of the ion cloud fraction as it transits into the drift region, which in turn leads to pronounced tailing through a slower, partial extraction. Since the ion could is spread thinner due to the competing net forces

on its opposite ends, its density becomes lower, thus increasing the Debye length through (1) and decreasing ion recombinations. This results in a higher total signal (peak area). For PW < 0, an increasing PW means that the fraction of the ion cloud which experiences a net force along $-\vec{z}$ is smaller, thus the thinning effect is lower and the area drops.

From the estimation of the initially desolvated ion cloud width and the FWHM of the Gaussian peak, the broadening by longitudinal diffusion can also be determined through equation 22. Since the spectrometer is operated in low field conditions, the Einstein relation (equation 14) is valid. It gives a diffusion coefficient $D = 8.7 \times 10^{-8}$ m^2·s^{-1}. Through equations 22 and 26, the expected FWHM of the TBA$^+$ peak at $t_\mathrm{d} = 9.68$ ms with an initial ion cloud width of 156 µs is 178 µs, which is significantly lower than the experimentally determined FWHM of 278 ± 11 µs. The latter is the mean experimental FWHM of the TBA$^+$ peak over three measurements at PW 250 µs. Fitting the Gaussian peak at PW 250 µs with equation 21 and $t_\mathrm{g} = 156$ µs leads to a calculated FWHM of $\omega_\mathrm{h} = 292$ µs which would seem to validate the fit. However, the corresponding longitudinal diffusion coefficient value is $D_\mathrm{L} = 7.3 \times 10^{-5}$ m^2·s^{-1}, which is an order of magnitude higher than the theoretical diffusion coefficient determined through the Einstein relation.

The fact that the experimental FWHM and the theoretical diffusion coefficient do not agree indicates that space charge effects are non-negligible in these experiments. Equation 49 is an extension of equation 22 based on [177] which then allows to estimate the broadening stemming from space charge effects, $t_\mathrm{SC} = 214$ µs.

$$\omega_\mathrm{h}^2 = t_\mathrm{diff}^2 + t_\mathrm{g}^2 + t_\mathrm{SC}^2 \tag{49}$$

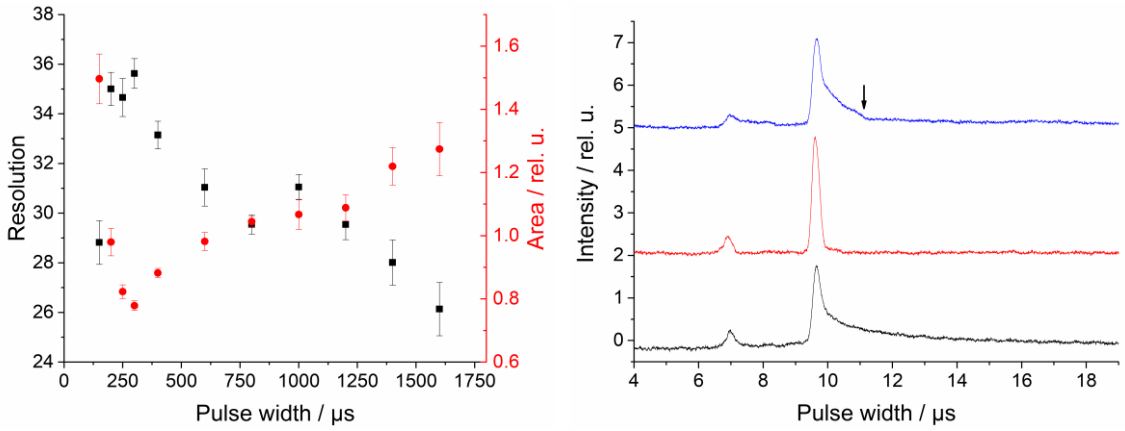

Figure 37: Influence of the pulse width on the TBA$^+$ peak on its resolution and area (left) and selected spectra at PW 150 (black), 250 (red) and 1,600 (blue) µs. 1 µM TBAB solution at E = 500 V·cm^{-1}, PD = 450 µs, PA = 4 kV·cm^{-1}

After the resolution maximum, a more straightforward decrease in resolution with increasing pulse width is observed: at very large opening times, tailing is high due to the extraction of ions stemming from the later desolvation of larger droplets and to the extraction of partially solvated ions which complete their desolvation during their drift. Decreasing the pulse width simply cuts off that tailing, as the decrease in area with decreasing PW in the left graph of figure 37 shows. This is also seen in the spectrum at 1.6 ms in the graph on the right. An arrow marks a sharp break in the peak shape which effectively shows the cut in the trailing part: only the ions which are

desolvated and already close to the grid are extracted. Charged droplets are quickly slowed down due to their size and don't make it into the drift region. The last ions to desolvate before the extraction pulse is switched off at best only partially experience PA and do not gain enough momentum to continue towards the drift region once PA = 0 kV·cm^{-1}. This is the difference with the tailing when PW < 250 µs. The possibility to simply cut off the tailing also shows that the signal intensity in the tailing region at a certain drift time directly relates to the number of ions introduced into the drift region at a given pulse time. In turn, that number depends on the desolvation rate, which is $1 - A_S/A_T$. The raw area of the peak tailing A'_S can thus be seen to depend on the integral of the desolvation rate as in equation 50, derived from 43. For an exact relation to be established, diffusion, ion losses and the initial desolvation through the pulse delay of 450 µs would need to be taken into account.

$$A'_S \propto 1 - \left(\frac{A_S}{A_T}\right)_0 \int_0^{PW} e^{-kt} dt \tag{50}$$

IV.2.2 Reduced pressure IM spectrometer optimization

IV.2.2.1 Reduced pressure IR-MALDI

A reduced pressure IM spectrometer was also developed in order to more efficiently analyze a broader range of substances. Larger masses mean a larger collision cross-section, and thus higher drift times, which would lead to lower resolution and ion losses as discussed before. The reduced pressure spectrometer allowed for better analytical conditions as will be discussed below.

The instrument was optimized with pulsed ion injection according to the parameters previously considered for atmospheric pressure. Both PD and PW follow the same trends as in the previous section, but PA required special consideration. Briefly, increasing the amplitude of the pulse relative to the drift voltage at atmospheric pressure results, up to a certain point, in better peak resolution through spatial contraction of the initial ion cloud. At reduced pressure, the upper PA limit is dictated by the breakdown voltage according to Paschen's law. The maximum voltage difference possible before discharges between the cup and the first drift ring was 700 V at 20 mbar. The carrier solution in the reduced pressure (RP) experiments contained a larger proportion of acetonitrile than at atmospheric pressure (AP) in order to obtain a more restrained dispersion process. Furthermore, its lower boiling point and higher vapor pressure promote desolvation and solvent evaporation, avoiding liquid deposition and accumulation in the cup, which facilitates discharges due to the initial lowering of the breakdown voltage according to Paschen's law.

While at atmospheric pressure pulsing consisted of producing ions in a field-free region and then injecting them into the drift region, at reduced pressure it was necessary to introduce a negative voltage difference. The reason for this is that with lower neutral gas density the pile-up effect becomes weaker [69], so the expansion of the plume stemming from the dispersion process of IR-MALDI isn't slowed down as much as at atmospheric pressure. This means that plume transport becomes more effective, sending ions and droplets into the drift tube even when no electric field

is applied. The transport takes place even when the main component of the plume is oriented away from the drift tube, which is why a "closing voltage" was applied. It results in an electric field along $-\vec{z}$ between the capillary and the inlet grid. The closing field influence on peak shape and resolution can be seen in figure 38. The pulse amplitude was kept constant for comparability. The closing voltage thus actively prevents charged droplets and ions from entering the drift tube before the delayed extraction pulse, giving them more time to desolvate.

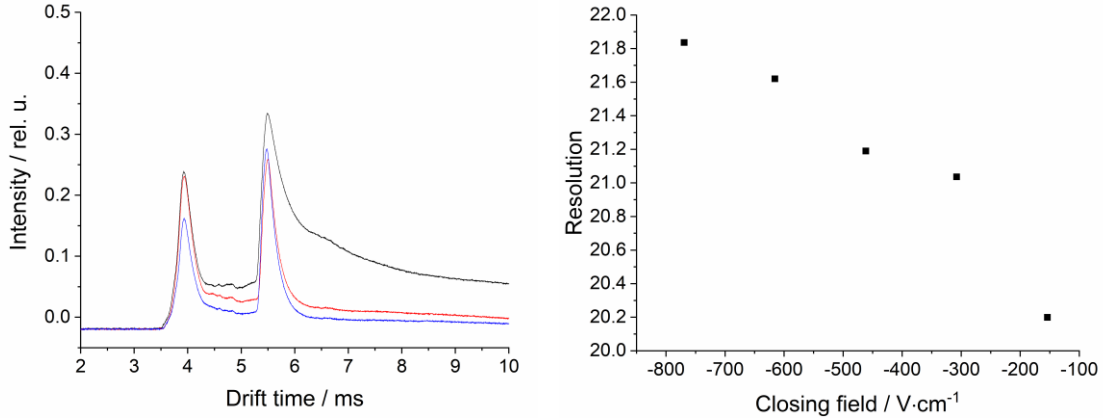

Figure 38: Left: Influence of different closing fields (black: 0 V·cm^{-1}, red: -308 V·cm^{-1}, blue: -615 V·cm^{-1}) on the peak shape and Right: on the analyte peak resolution of a 5 µM TBAB solution in ACN/H_2O 1:1 at E/N = 12.2 Td at 100 mbar. PD = 100 µs, PW = 200 µs, PA = 1.1 kV·cm^{-1}

At constant electric field, the effect of reduced pressure can be clearly seen: a linear shift towards lower drift times as well as higher signal (Figure 39). A monomer peak is seen at the highest intensity, followed by peaks of decreasing intensity. These correspond to multimeric species.

The lower the pressure, the fewer collisions with drift gas molecules. The ions move faster through the drift tube, which reduces the influence of the Coulomb repulsion of like-charged ions. Thus, the ion cloud has less time to expand and discharge at the wall, resulting in a higher signal. Less intense peaks such as those corresponding to multimer ions are thus more easily seen.

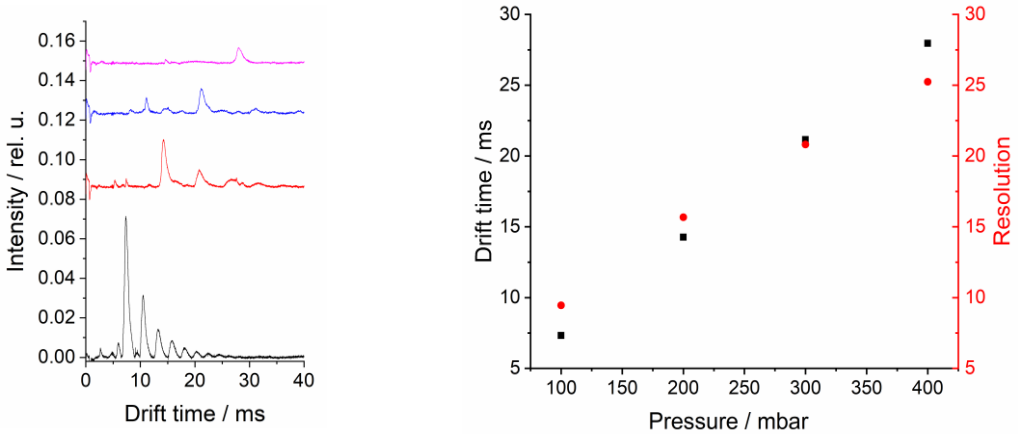

Figure 39: Influence on the pressure on a 500 µM Bradykinin + 1 µM TBAB solution in ACN/H_2O 1:1. Constant drift field E = 377 V·cm^{-1}, closing field -923 V·cm^{-1}. PA = 2 kV·cm^{-1}, PD = 0 µs. Left: spectra at different pressures, from bottom to top: 100, 200, 300 and 400 mbar with 600, 600, 700 and 700 µs PW respectively. Right: Drift time and resolution of the monomer analyte peak (most intense peak)

Under low field conditions, equations 13, 29 and the ideal gas law give

$$\frac{1}{t_d} = \frac{K_0 P_0}{L R T_0} \frac{E}{N}, \tag{51}$$

which means that the drift time t_d and the reduced field strength E/N have a linear inverse relationship, as observed on the right graph of figure 39. The reduced pressure IM spectrometer allows higher E/N values to be reached without having to apply very strong electric fields. This is of particular importance since the RP IM spectrometer is twice as long as the AP one, thus needing higher electric potential values to reach the same field values. A higher drift length and a lower drift time – through elevated E/N – should lead to better resolution for an infinitely narrow initial ion distribution as seen in equation 27. The smaller pulse widths at lower pressure should also lead to improved resolution. However, as the right graph in figure 39 shows, lower pressures (and thus higher E/N) were observed to result in a drop in resolution despite the lower drift time, the higher drift length and the smaller PW. This might be due to the fact that under low field conditions, lower pressure leads to a higher mobility through equation 29 and thus to a higher diffusion coefficient through equation 14. Furthermore, reduced pressure implies fewer ion-neutral collisions, so fewer opportunities for desolvation, which would lead to tailing and peak broadening.

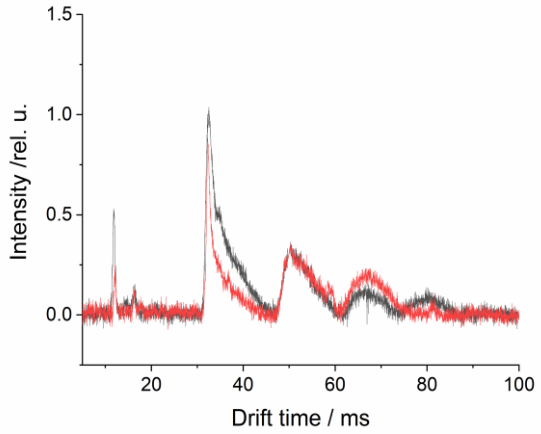

Figure 40: Bradykinin (100 µM) with TBAB (1 µM) in ACN/H_2O 1:1 at constant E/N (4.06 Td). No closing field. PA = 1.77 kV·cm^{-1}, PD = 400 µs, PW = 500 µs. Black: 100 mbar. Red: 300 mbar

Figure 40 shows Bradykinin spectra at two different pressures and voltages but at a constant reduced field strength E/N in order to independently study the effect of different pressures. As expected, the drift time is constant at constant E/N but the tailing looks different. The spectra were pulsed from a field-free value (without a closing field) in order to observe how desolvation is affected by the pressure. The different experimentally derived parameters of the Bradykinin singly charged monomer peak are given in table 2.

Table 2: Bradykinin peak properties at 4.06 Td, based on figure 40

P (mbar)	t_d (ms)	A_T (rel. u.)	FWHM (ms)	D (m^2·s^{-1})	t_{diff} (µs)	R	A_S/A_T
100	32.48	4.50	3.10	1.88×10^{-5}	398	10	0.70
300	32.34	2.26	1.37	6.29×10^{-6}	229	24	0.63

As already visible in Figure 40, the peak area is significantly higher at lower pressure, whereas the peak becomes broader (higher FWHM) and the resolution decreases. The diffusion coefficient D was determined through equations 13–14 and the drift time, which enabled to calculate t_{diff} through equation 26. Equation 14 in combination with equation 29 state that D(100 mbar) = 3 × D(300 mbar). Experimentally, as seen in table 2, D(100 mbar) = 2.99 × D(300 mbar), which is in excellent agreement. Approximating t_{g} by the pulse width of 500 µs, equation 49 gives t_{SC}(100 mbar) = 3.03 ms and t_{SC}(300 mbar) = 1.25 ms, which would mean that $t_{\mathrm{SC}} \cong \omega_{\mathrm{h}}$. This is clearly an overestimation when compared to the previous section, where $t_{\mathrm{SC}} = 214$ µs at atmospheric pressure. Reduced pressure and a higher diffusion coefficient should lead to a faster thinning out of the initial ion cloud. This would mean a lower ion number density and thus weaker space charge effects than at atmospheric pressure, if any at all. This is evidence that the FWHM, ω_{h}, depends on another factor, which is desolvation. As the ratio $A_{\mathrm{S}}/A_{\mathrm{T}}$ indicates, desolvation is more inefficient at lower pressures, resulting in broadening and tailing, which leads to lower resolution. In order to improve peak desolvation, an additional heated tube length was introduced into the setup, operating the IR-MALDI source at atmospheric pressure with the reduced pressure spectrometer.

IV.2.2.2 Atmospheric pressure ionization

In this version, the tip of the sample capillary was placed just before that of the ion transfer tube, where IR-MALDI took place at atmospheric pressure. The transmission of ions through transfer tubes is on average below 30 % [178], which means a loss of intensity is to be expected when compared to the reduced pressure ionization source. An efficient initial transport into the transfer tube is thus of importance, which is why a repeller electrode was used. When the source capillary was placed in front of the ion transfer tube, there was no clear droplet at its tip due to electrical point effects[8]. Once the repeller electrode was set in, a droplet was again visibly formed. Its shape was skewed towards the opening of the ion transfer tube due to the reduced pressure, which was not enough to overtake the electric field in the previous case (Figure 41).

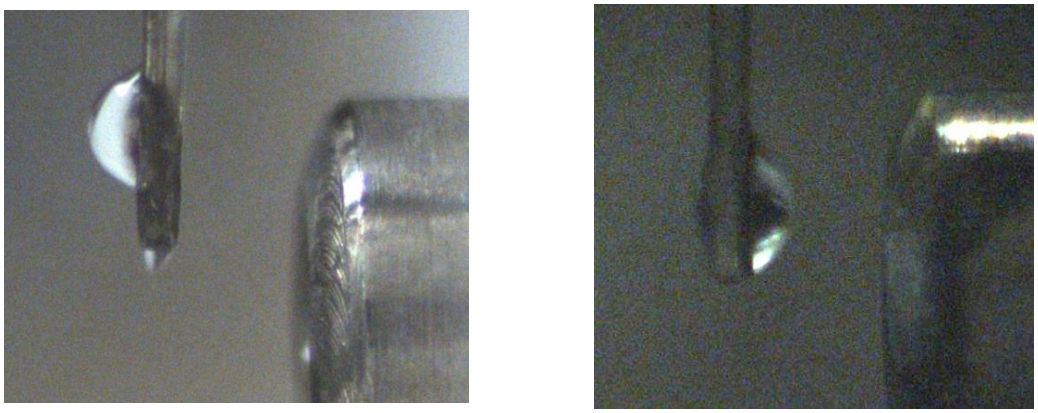

Figure 41: ACN/H_2O 1:1 droplet shape at 100 mbar and 900 V difference between capillary and ion transfer tube. Left: No repeller electrode. Right: With repeller electrode

[8] Accumulation of electrical charges which create a strong electric field on pointed surfaces of an electric conductor

With a well-shaped and stable droplet, the influence of different pulse injection parameters was checked, starting with the pulse delay. A large pulse width was used to decouple it from the PD. The first effect observed was on the drift time. At higher PD, the drift time decreases until it reaches a constant value (Figure 42, left). This reflects the fact that ions need a certain transfer time τ_t to go through the ion transfer tube: the apparent drift time t_d' actually depends on the drift time t_d, on τ_t and on PW as in (52), which is why the slope of the t_d' vs. PW plot in figure 42 is -1.

$$t_d' = t_d + \tau_t - \mathrm{PD} \tag{52}$$

If PD $< \tau_t$, the electric pulse has begun before the ions have reached the pre-drift region, so they are all immediately deflected into the drift region after a certain dead time. This is why the area is constant at its maximum value (Figure 42, right). When PD $> \tau_t$, the closing voltage keeps ions away from the drift tube until the pulse is applied, resulting in constant drift time. The area decreases since only a part of the ions is selected. For the same reason, the FWHM follows exactly the same trend as the area (not shown). It is the determining factor for the resolution, so the ~600 µs change in apparent drift time does not affect it in a significant way.

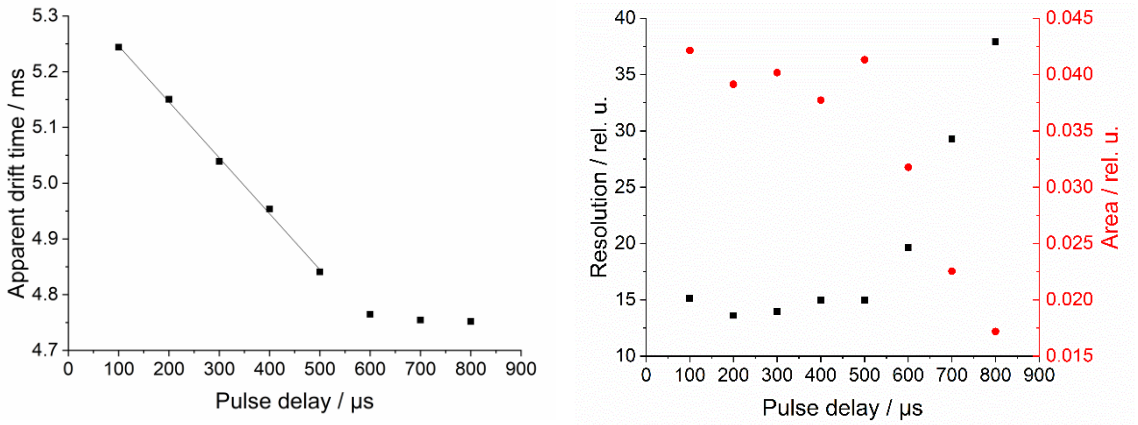

Figure 42: Influence of the pulse delay on the drift time (left) and on the resolution and area of the analyte peak (right) in a 750 nM TBAB solution in ACN/H_2O 1:1. 100 mbar, 14.2 Td, -153 V·cm^{-1} closing field, IF = 12.9 kV·cm^{-1}, PA = 1.38 kV·cm^{-1}, PW = 3 ms

τ_t is a constant of the system, given that the transport of the ions through the tube is governed by the maximum possible flow velocity stemming from a choked flow regime, i.e. the local speed of sound [179]. This occurs when the pressure difference between both ends of the tube is approximately 500 mbar, after which point the volume flow becomes almost independent from the pressure difference, approaching an asymptotic value [178]. Since cup, ion transfer tube and repeller are kept at the same voltage, there is no electric field which could influence the mobility of the ions during τ. Only the sample capillary is at a higher potential but this has no influence on τ_t, as the apparent drift time t_d' remains constant at all tested capillary voltages (Figure 43, left). The ion transfer tube opening is small enough to effectively shield the rest of the system from the ensuing electric field. Concerning the signal, the peak area slightly increases with the capillary voltage difference (Figure 43, right), no doubt due to improved ion transfer on the atmospheric

pressure side. The capillary voltage influence is studied through the inlet field (IF), defined as the difference with regard cup voltage while no ion extraction takes place over the distance to the ion transfer tube.

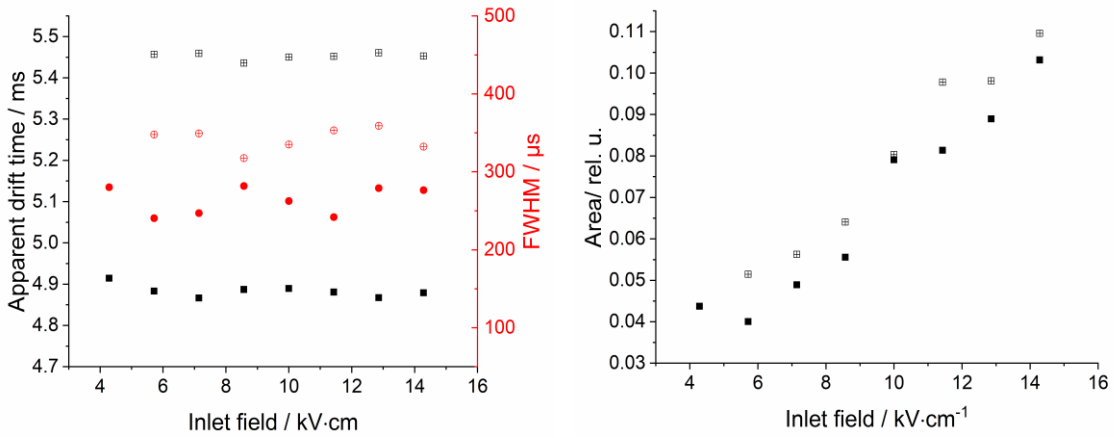

Figure 43: Influence of the inlet field on the drift time and FWHM (left) as well as on the area (right) of the TBA⁺ peak in a 750 nM TBAB solution in ACN/H_2O 1:1. 100 mbar, 14.2 Td, -153 V·cm^{-1} closing field, PA = 615 V·cm^{-1}, PW = 3 ms. Open plot: PD = 0 µs, Filled plot: PD = 600 µs

The increase in area is valid at different pulse delays, although a difference of 600 µs is visible in the drift time between 0 and 600 µs PD, in accordance with figure 42. The difference in FWHM and in area with varying PD are both also in agreement with the previously observed trends, showing little or no coupling of the inlet field and PD influences. In fact, coupling between all parameter effects was systematically checked. Substance dependence was also ruled out by using a more massive ammonium salt, tetraoctylammonium bromide (TOAB).

After cross-checking every parameter, only two important couplings were found. The first one is that of the pulse amplitude with the inlet field. A higher inlet field improves the signal with a more efficient ion transmission, but the effect is amplified by the use of an optimal pulse amplitude, which transmits the ions from the cup into the drift region. The peak parameters depend particularly on the PA but not on the IF.

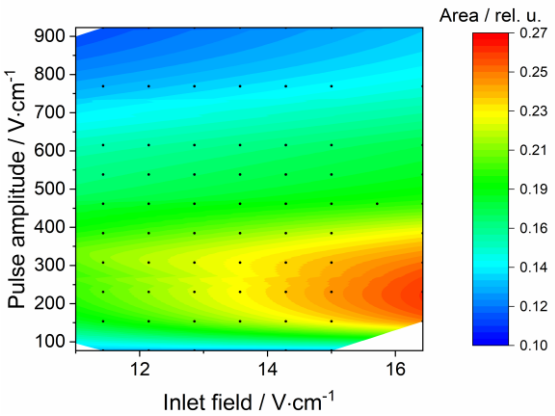

Figure 44: Coupling of the influences of the inlet field as well as the pulse amplitude on the area of the TOA⁺ peak for a 750 nM TOAB solution in ACN/H_2O 1:1. 100 mbar, 14.2 Td, varying closing fields, PD = 0 µs, PW = 3 ms

The second coupling between effects was that of the pulse width with the pulse delay due to the presence of the transfer time τ_t. At low pulse widths and delays, specifically if PD + PW $< \tau_t$, the

injection pulse takes place before the ions have reached the cup, so no signal is observed. If PD is high enough, the apparent drift time is constant (Figure 45, left). At 500 µs PD and 200 µs PW the drift time is already constant but the signal is weak (not shown). This can give a qualitative indication as to the temporal distribution of the ion cloud after the transit through the transfer tube. Let τ_t be the mean value for the transport time of the ions in the ion cloud. At 500 µs PD, PD $< \tau_t$ and PD $\approx \tau_t$. With 200 µs PW, both PD and PW are low enough that only the front of the ion cloud is probed. As the width of the pulse becomes larger, the probed ion cloud section becomes larger and larger and the peak center shifts towards higher values, where the ion density is higher. The signal response is directly proportional to the number of ions arriving at the detector at given time t, which in turn depends on the local number density of the extracted ions, $n(PD, PW)$. Thus, with varying PW, the peak shift is directly proportional to the variation in local ion density at the exit end of the ion transfer tube (relation 53).

$$\frac{\delta t'_d(PD, PW)}{\delta PW} \propto \frac{\delta n(PD, PW)}{\delta PW} \tag{53}$$

According to (53), differentiating the experimental t'_d data by PW can give an idea regarding the temporal distribution of the ions arriving into the cup at a given time PD + PW. What becomes clear in the right graph of figure 45 is that there are two waves of ions, which is consistent with the previously discussed two-step mechanism of ion transport. The pulse delay and width must thus be chosen so as to obtain a constant apparent drift time, so that $t'_d = t_d$. More conclusions cannot be drawn regarding the width of the initial ion cloud given that distortion through its path in the ion transfer tube and upon arrival into the cup cannot be accounted for. What can be said is that a slight variation in τ_t will be observed depending on the initial dispersion conditions, namely the spatial relation between the ion transfer tube inlet and the dispersion plume.

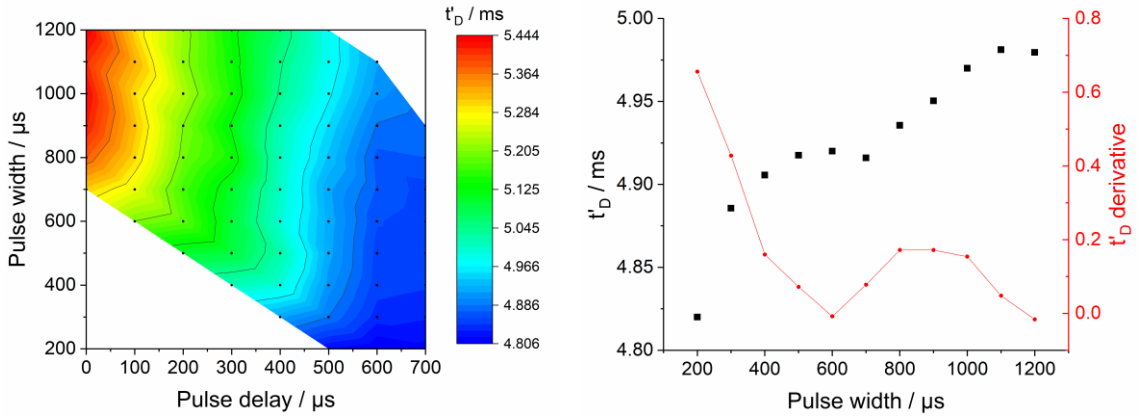

Figure 45: Apparent drift time of the analyte peak in a 750 nM TBAB solution in ACN/H_2O 1:1. 100 mbar, 14.2 Td, -615 V·cm^{-1} closing field, IF = 17.1 kV·cm^{-1}, PA = 462 V·cm^{-1}. Left: Coupled influences of PD and PW. Right: Influence of PW at PD = 500 µs

IV.3 Applications

IV.3.1 Analytical

IV.3.1.1 LOD and linear range

Once the atmospheric pressure spectrometer was optimized in terms of resolution and peak shape, its analytical performance was evaluated. Limits of detection (LOD) and linear ranges were determined for a number of substances. The results between static conditions and pulsed conditions were compared to insure that the partial loss of signal due to pulsing did not affect the analytical parameters.

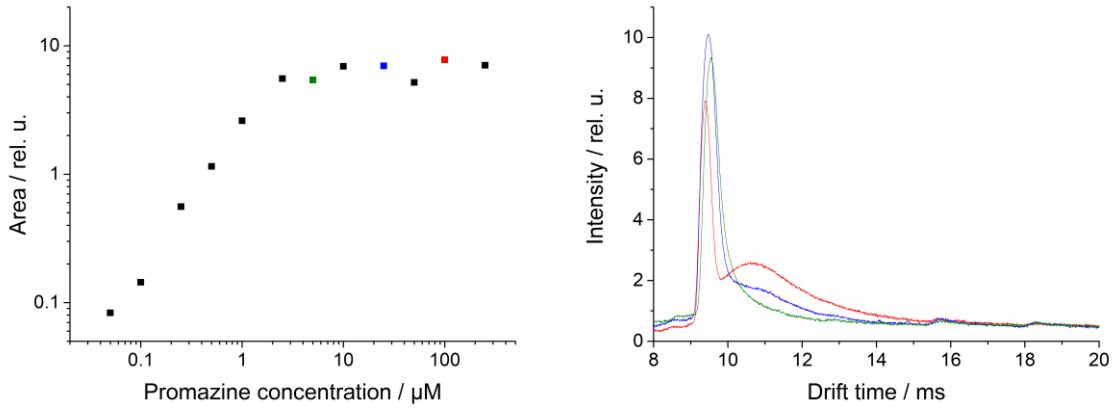

Figure 46: Left: Area vs. concentration plot for promazine under static conditions. Right: Selected IM spectra from the curve corresponding to concentrations of 5 µM (green), 25 µM (blue) and 100 µM (red). E = 500 V·cm^{-1}, E_{IR} = 1.5 kV·cm^{-1}

Figure 46, left, shows the signal response of promazine as a function of concentration for a static extraction. There is a clearly visible linear range which spans over two orders of magnitude followed by a plateau as the peak area stagnates after 5 µM. This curve shape is similar to that obtained by Wiederschein et al. [84] for their Poisson model of the charge distribution of NaCl. They propose that at high concentrations, interionic interactions become more relevant, thus decreasing ion yields and resulting in a plateau. In the case of the promazine calibration curve, figure 46, right, sheds some light on the origin of the plateau. Three spectra from that region were selected. Although their area is virtually constant, their shape is not. At 5 µM the promazine peak is only slightly asymmetric but as the concentration increases a shoulder starts to develop until the tailing finally emerges as a separate, very broad peak. The intensity of the main, Gaussian analyte peak slightly decreases with concentration as well. At very high concentration, Wiederschein et al. reported that the Poisson model (even with corrections for interionic interactions) did not fit the experimental data. They observed a decrease in ion yields due to strong charge recombination. This might explain the decrease in the Gaussian peak area and intensity, which is compensated by the increased tailing. The latter is due to a higher probability of ions being released from nano droplets in a heated bath gas when the total number of ions increases. This balance between the two trends could explain why a plateau is observed in the calibration curve of promazine as well as TBAB (Figure 47) at similar peak area values.

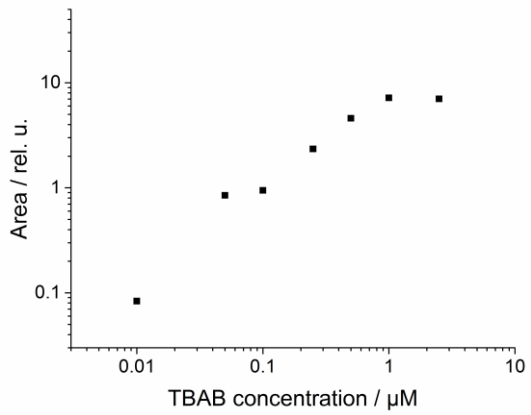

Figure 47: Area vs. concentration plot for TBAB under static conditions at E = 500 V·cm^{-1}, E_{IR} = 1.5 kV·cm^{-1}

Pulsed extraction conditions enable the suppression of the tailing area, thus only detecting the ions which give rise to the Gaussian peak, i.e. stemming from a definite ion cloud and not from larger droplets and late desolvation. Under optimal pulsed conditions, a decrease in the analyte peak area is observed. This is due to strong ion recombination at high concentrations (see above) and is observed in both TBAB and promazine (Figure 48).

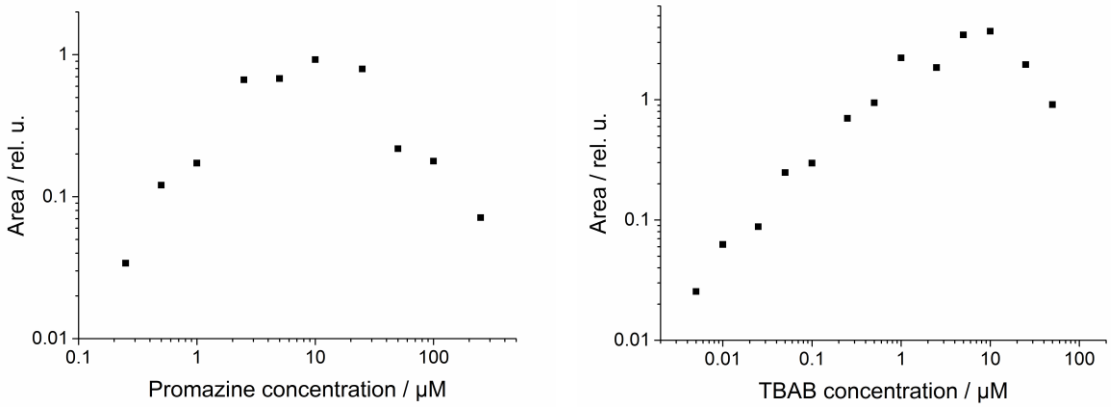

Figure 48: Peak area vs. concentration under pulsed extraction conditions, E = 500 V·cm^{-1}, PA = 1.5 kV·cm^{-1}. Left: Promazine, PD = 500 µs, PW = 300 µs. Right: TBAB, PD = 300 µs, PW = 400 µs

The limit of detection for both substances under pulsed conditions is either similar to or lower than under static conditions. While the LOD and the total response are comparable for both promazine and TBAB under static conditions, a higher pulse delay and lower pulse width for improved desolvation and peak shape in promazine also lead to more ion losses, slightly decreasing the LOD and the signal response in comparison to TBAB with lower PD and higher PW. This indicates that a compromise has to be made between resolution and sensitivity when employing pulsed extraction.

The limits of detection were determined for various substances in IR-MALDI IM spectrometry with static extraction and compared to IR-MALDI MS and ESI IM spectrometry. The results are given in Table 3. They show a good comparability to mass spectrometry, especially for small molecules, and are generally lower than for ESI IM spectrometry for a wide range of biologically relevant substances such as herbicides (atrazine, metazachlor), peptides (bradykinin), surfactants (TBAB) and psychopharmaceutic drugs (promazine, chlorprothixene, perphenazine, imipramine).

Table 3: Comparison of the limits of detection (LOD), in nM, for different biologically relevant substances in ESI and IR-MALDI-IM spectrometry as well as IR-MALDI-MS

	IMS		MS
	ESI	**IR-MALDI**	**IR-MALDI**
Atrazine	100	50	100
Metazachlor	200	100	50
Bradykinin	1000	2500	250
TBAB	100	5	10
Promazine	50	25	25
Chlorprothixene	100	25	10
Perphenazine	250	100	--
Imipramine	100	50	--

IV.3.1.2 Separation of mixtures

IR-MALDI produces mostly low charged states, which means that for most substances only one peak will be observed. This is a tremendous advantage when analyzing mixtures of substances, as the more peaks there are, the harder it will be to resolve them. With IR-MALDI, IM spectrometry can easily resolve simple mixtures of substances, as illustrated in figure 49 with a range of surfactants.

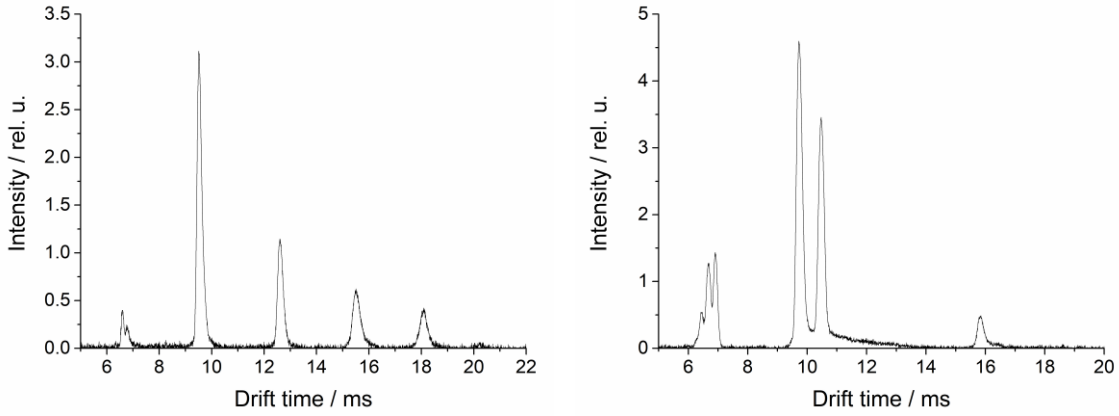

Figure 49: IM spectra of substance mixtures with the cluster ion peak around 7 ms. Left: A series of tetraalkylammonium ions: TBA^+, THA^+, TOA^+ and TDA^+. All in 10 µM concentration. Right: The isomers TBA^+ and $DEDMA^+$ (3 µM and 20 µM respectively). The TBA^+ dimer peak is seen around 16 ms

Baseline separation of the homologous series of tetrabutyl, tetrahexyl, tetraoctyl and tetradecyl ammonium bromides (graph on the left) is neatly achieved (TBA^+, THA^+, TOA^+ and TDA^+, respectively). The first peak corresponds to the solvent cluster peak and the rest are in order from the smallest to the largest molecular ion. The graph on the right shows the separation of two isomers, which is the strong suit of ion mobility spectrometry. Dodecylethyldimethyl ammonium ($DEDMA^+$) has a long tail when compared to the more compact isomer, TBA^+. This translates into a larger cross-section and a higher drift time, which enables baseline separation of these two isomers. At 16 ms, the $DEDMA^+$ dimer is seen. The baseline separation of neuroleptics and amino

acids is also possible, as the proof-of-principle measurements in figure 50 show. Further study, for example by MS, would be necessary to attribute each peak to a specific ion. In the case of the psychopharmaceutic drugs, it is interesting to note that three peaks are observed for perphenazine but only one for the other drugs (determined by comparison with single-substance spectra). This might be due to the presence of degradation products and intermediates stemming from sulfoxidation and hydroxylation of the substance [180].

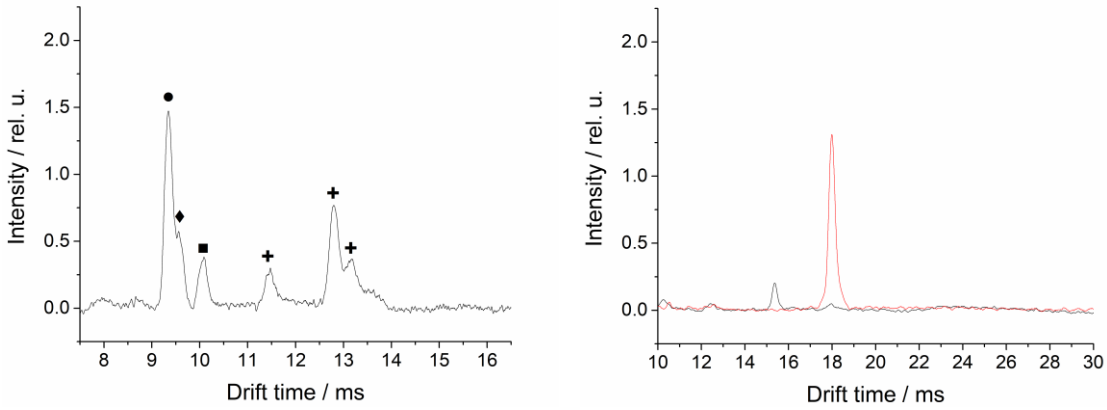

Figure 50: Left: Separation of a mixture of psychopharmaceutic drugs, all at 10 µM concentration, under pulsed extraction conditions, E = 500 V·cm^{-1}, PA = 2 kV·cm^{-1}, PD = 250 µs, PW = 200 µs. ● Promazine, ♦ Imipramine, ■ Chlorprothixene, ✚ Perphenazine. Right: Theoretical separation of an amino acid mixture, both at 100µM, E = 500 V·cm^{-1}, PA = 1.5 kV·cm^{-1}, PD = 500 µs, PW = 400 µM. Histidine (black) and arginine (red)

The advantage of IM spectrometry is its unique separation of ions through their cross-section. Since no other method provides this, it is ideally suited to complement other analytical techniques such as MS or chromatography. Specifically, IR-MALDI has been successfully coupled to HPLC and MS [50,58], which is why HPLC-IR-MALDI-IM spectrometry was also investigated here with the help of the microbeam source. The advantage of using a microbeam is that it can work at high flow rates such as the ones used in HPLC, so direct on-line coupling is possible between the techniques. Our group has already developed an orthogonal ESI-IM spectrometer as a detector for HPLC. Figure 51 shows that the same can be done with an IR-MALDI-IM spectrometer.

A mixture of pesticides was analyzed and separated by HPLC in the retention time axis as well as by IM in the drift time axis. The constant line at around 7 ms drift time corresponds to the solvent cluster ion peak of ACN/water. The spectrum was processed with a version of the OpenMS software which was adapted to IM spectrometry [181,182]. For peaks which are coeluted or poorly resolved with HPLC, such as methabenzthiazurone and chlortolurone, a baseline separation is obtained in the IM dimension (red trace). Likewise, most of these substances have very similar drift times, which means they would not be separated by ion mobility alone. The one-dimensional peak capacity n is defined as $\mathrm{n} = \Delta t/\omega_{\mathrm{h}}$, where ω_{h} is the mean FWHM of the peaks and Δt is the available drift time span in the ion mobility dimension or retention time span in the chromatography dimension. The two-dimensional peak capacity is simply the product of both one-dimensional values, such that ${}^{2\mathrm{D}}\mathrm{n} = \mathrm{n}_{\mathrm{drift}} \cdot \mathrm{n}_{\mathrm{retention}}$. The narrow drift time window between 7.67 and 10.22 ms leads to $\mathrm{n}_{\mathrm{drift}} = 10.51$ in the ion mobility dimension, whereas in the chromatographic dimension $\mathrm{n}_{\mathrm{retention}} = 36.50$. This leads to a 2D peak capacity of ${}^{2\mathrm{D}}\mathrm{n} = 383.53$.

Thus, the orthogonal nature of the separations in the retention time and drift time dimensions offers a higher peak capacity through the coupling of both techniques.

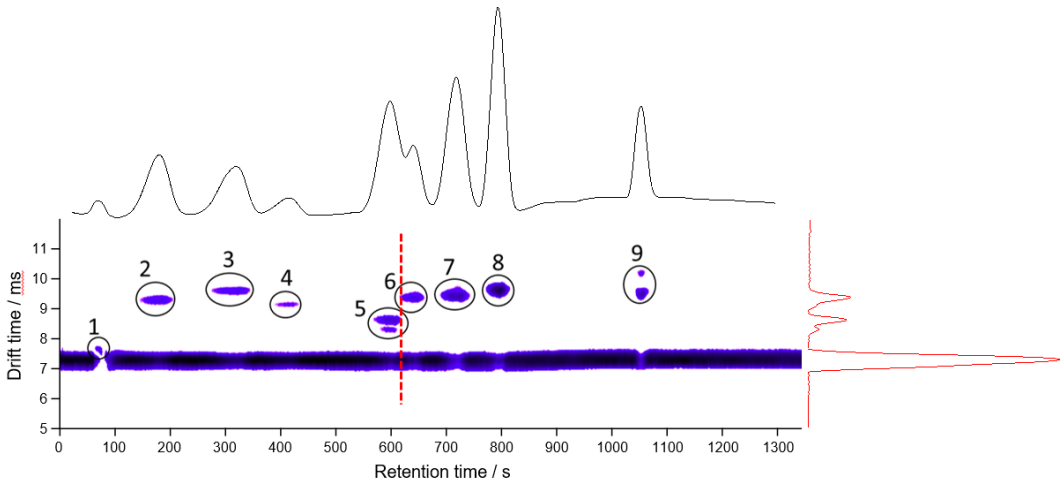

Figure 51: 2D spectrum of the separation of a mixture of pesticides by HPLC-IR-MALDI-IM spectrometry (E = 500 V·cm^{-1}, PA = 1.5 kV·cm^{-1}, PD = 100 µs, PW = 250 µs), 1: diquat monohydrate, 2: chloridazone, 3: metoxurone, 4: monurone, 5: methabenzthiazurone, 6: chlortolurone, 7: isoproturone, 8: metazachlor, 9: metolachlor. Black trace: Chromatogram, red trace: IM spectrum at a retention time of 618.4 s showing the baseline IM separation of poorly resolved peaks in the retention time dimension

IV.3.2 Fundamental: High-field mobility

The effects of high reduced field strength on ions can be various and complex, as briefly discussed in Section II.3.3. If the low-field condition is not valid, meaning K_0 is not a constant anymore, collision cross-sections cannot be determined by the Mason-Schamp equation 28. However, the change in K_0 can be used to separate species through Field Asymmetric Ion Mobility Spectrometry (FAIMS), also known as Differential Mobility Spectrometry (DMS). Even though the high field behavior of monoatomic ions in monoatomic gases is well understood and characterized, there is still work to be done in the case of polyatomic ions and polyatomic gases. The reduced pressure spectrometer can be operated under high field conditions, thus enabling the study of high field effects. A series of alkyl ammonium ions were used for this purpose: NH_4^+, methylammonium (MA^+), dimethylammonium (DMA^+) and tetramethylammonium (TMA^+). The RP spectrometer with AP ionization was employed.

The drift time t_d as defined in section IV.2.2.2 encompasses the time the ions spend in the drift tube t_DT as well as the time they spend in the ionization region t_IR. The temperature conditions in both regions are different, as well as the electric field due to the pulsed nature of the ion injection. Thus, the drift time can be expressed as $t_\mathrm{d} = t_\mathrm{DT} + t_\mathrm{IR}$, where both t_DT and t_IR are determined by different drift conditions. In order to specifically study the influence of the reduced field strength on the drift time, and thus the mobility, accurate drift time determination is necessary. For that purpose, t_DT is isolated by using different injection voltages with the same drift field, resulting in varying t_IR and a constant t_DT. This is reflected in the following t_d expression, where L_IR, T_IR and E_IR are L, T and E values related to the ionization region:

$$t_{\mathrm{d}} = t_{\mathrm{DT}} + \frac{T_0}{K_0\, T_{\mathrm{IR}}\, P_0} \frac{P\, L_{\mathrm{IR}}}{E_{\mathrm{IR}}}. \tag{54}$$

At a given drift voltage, using different ion injection voltages ($L_{\mathrm{IR}}/E_{\mathrm{IR}}$) which are low enough to keep the low field condition valid makes it possible to determine t_{DT} by plotting t_{d} as a function of $P \cdot L_{IR}/E_{\mathrm{IR}}$ according to (54). In this way, the influence of a specific E/N on the mobility of different ions is studied by isolating t_{DT} from t_{IR}. When the drift voltage results in high field conditions, these will be reflected in t_{DT}.

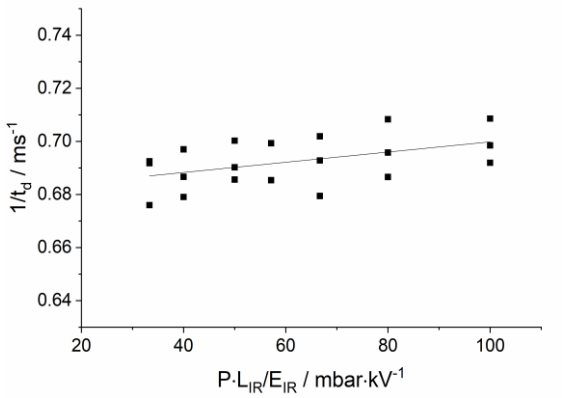

Figure 52: Determination of t_{DT} by equation 54 for a 100 µM solution of MAB in ACN/H_2O 1:1 at 20 mbar and 73 Td

Figure 52 shows an example of t_{DT} determination as the intercept of the linear regression of three measurement series corresponding to low field conditions in the ionization region. With t_{DT} and equations 13 and 29 it was possible to determine K_0 at different E/N values for a series of ammonium salts. The resulting mobilities as a function of the reduced field strength are shown in figure 53. Pressures used were 18, 20 and 30 mbar. Control points between the measurement series at different pressures were done by measuring at the same E/N values, at 40.56 Td (all three pressures), 50.70 Td (20 and 30 mbar) and 76.05 Td (20 and 18 mbar). These verify the continuity between different measurement series. The error bars represent the standard error with a 95 % confidence interval.

The first observation is that K_0 deviates from linearity at higher E/N values for three out of four ammonium ions (K_0 is considered constant for TMA^+). A linear fit of the low field K_0 values was carried out for every ammonium ion. The K_0 values were then corrected by the mobility of the TBA^+ ion, determined in separate measurements but in the same way and over the same range of conditions. A correction factor of 1.15 was thus determined by dividing the literature TBA^+ K_0 value (1.33 $cm^2 \cdot V^{-1} \cdot s^{-1}$) by the experimental value (1.13 $cm^2 \cdot V^{-1} \cdot s^{-1}$). For the ammonium ions showing a strong deviation from the low field behavior (NH_4^+, MA^+, DMA^+) a second linear regression was carried out over the highest reduced field strengths. This served to approximate the $(E/N)_{\mathrm{c}}$ value as defined in section II.3.3, i.e. the critical reduced field strength after which K_0 stops being a constant, as the intersection point of both regression curves.

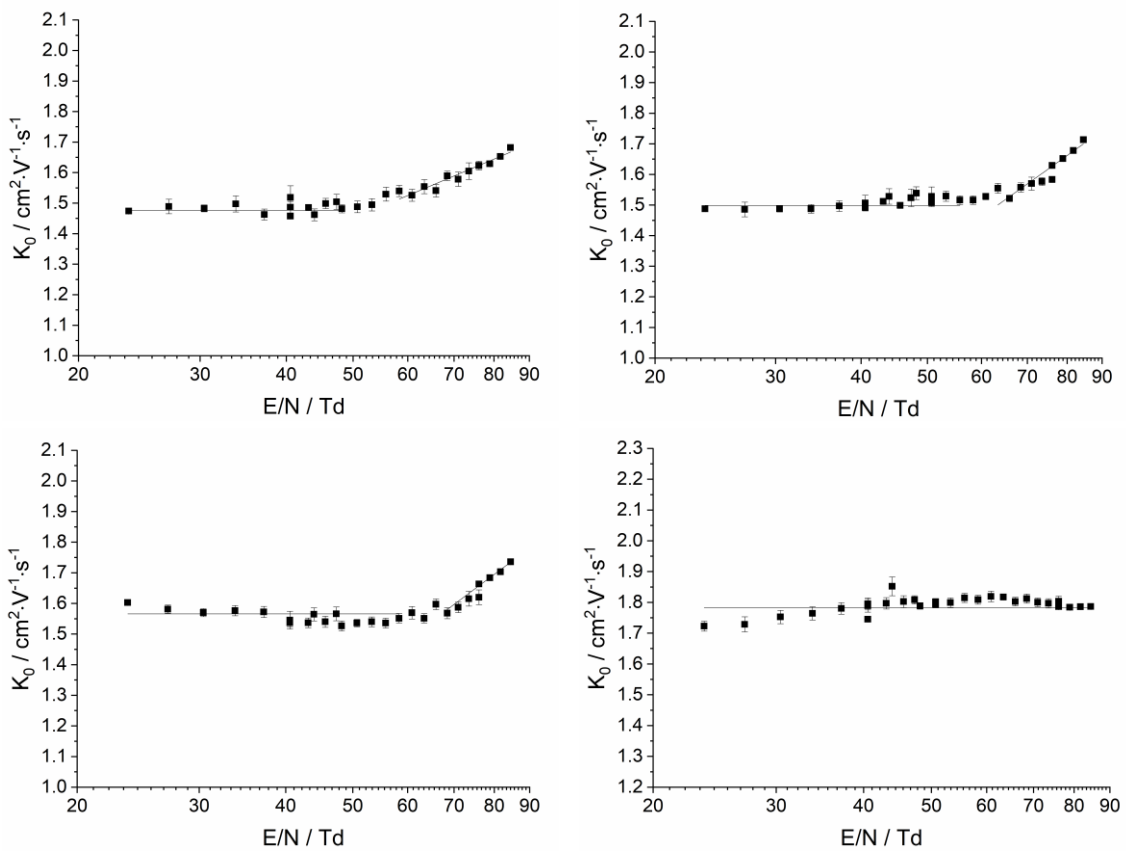

Figure 53: Reduced mobility of ammonium ions as a function of E/N (from left to right, top to bottom: ammonium, methylammonium, dimethylammonium, tetramethylammonium)

As the choice of points for the high field regression has an influence on the thus determined $(E/N)_c$ values, it was attempted to take points not directly at the start of the high field effects but rather after a certain distance, so as to not "manually select" $(E/N)_c$. The results are given in table 4 and compared to the theoretical K_0 values for the naked ions, obtained through collision cross-sections determined in the nitrogen version of MOBCAL.

Table 4: Comparison of theoretical and corrected experimental reduced mobilities as well as experimentally approximated $(E/N)_c$ for the ammonium ions

		Theoretical	**Experimental**	
	Mass (Da)	**K_0 ($cm^2 \cdot V^{-1} \cdot s^{-1}$)**	**K_0 ($cm^2 \cdot V^{-1} \cdot s^{-1}$)**	**$(E/N)_c$ (Td)**
NH_4^+	18.04	3.18	1.738 ± 0.004	51.09 ± 9.86
MAB^+	32.07	2.76	1.764 ± 0.004	62.58 ± 15.26
DMA^+	46.10	2.58	1.843 ± 0.008	66.26 ± 14.94
TMA^+	74.15	2.33	2.099 ± 0.004	-----

What can be seen is that the experimental low field K_0 values are systematically below the theoretical values. Furthermore, they do not follow the alkylation order. As the ion gets larger, its reduced mobility should decrease, as the theoretical K_0 values show. Instead, the opposite has been observed. This is the first indication that the low field values which are observed do not correspond to the naked ions but to clusters with the solvent. In fact, it is well known that ammonium ions readily cluster with water [94,183], but the desolvation in the heated ion transfer tube (to 200 °C) was thought to be enough to obtain naked ions. However, the change in mobility

at higher reduced field strengths might stem from the loss of one or more water molecules, signaling incomplete desolvation and clustering. Given that TMA^+ is a quaternary ammonium ion, it can be assumed that it will not as easily form clusters with water molecules through hydrogen bonding. This is confirmed by the fact that the experimental and the theoretical reduced mobilities of TMA^+ are relatively close. Nonetheless, the 10 % deviation between the two probably indicates some form of clustering. MS analysis of the substances did not reveal any ammonium ion clusters, which probably dissociated in the ion optics at the entrance of the instrument and in the high vacuum.

Equations 38 and 39 both contain a parameter y which is unknown and depends on the relative measurement accuracy. The individual $(E/N)_{\mathrm{c}}$ values can thus not be directly calculated, but if y is constant between measurement series, ratios of $(E/N)_{\mathrm{c}}$ can be determined. The ratio in equation 55 was determined through (38) and the ratio in equation 56 was determined through (39).

$$\frac{(E/N)_{\mathrm{c},1}}{(E/N)_{\mathrm{c},2}} = \frac{\Omega_{\mathrm{D}.1}}{\Omega_{\mathrm{D}.2}} \sqrt{\frac{m_{\mathrm{I},1}}{m_{\mathrm{I},2}}} \sqrt{\frac{(m_{\mathrm{I},1} + m_{\mathrm{G}})}{(m_{\mathrm{I},2} + m_{\mathrm{G}})}} \tag{55}$$

$$\frac{(E/N)_{\mathrm{c},1}}{(E/N)_{\mathrm{c},2}} = \frac{K_{0,2}}{K_{0,1}} \tag{56}$$

Through these two expressions, the $(E/N)_{\mathrm{c}}$ ratios of every naked substituted ammonium ion to the naked ammonium ion were calculated with (55) and the theoretical cross-section values (column I in table 5) as well as with (56) and the experimental low field mobility values (column II). These two calculated ratios were then compared to the ratios obtained from the graphically approximated $(E/N)_{\mathrm{c}}$ in table 4 (column III).

Table 5: Ion $(E/N)_c$ ratios calculated through theoretical cross section values (I), experimental low-field mobility values (II) and graphically approximated $(E/N)_c$ values (III)

	I	II	III
MA^+ / NH_4^+	1.15	0.985 ± 0.003	1.2 ± 0.5
DMA^+ / NH_4^+	1.23	0.943 ± 0.004	1.3 ± 0.5
TMA^+ / NH_4^+	1.36	0.828 ± 0.002	----

For the naked ions, the standard high field effect in the case of MA^+ should thus start at an E/N value which is 1.15 times higher than that for NH_4^+ and so on, obtaining higher $(E/N)_{\mathrm{c}}$ values for larger ions. Since the observed low field K_0 values decrease with increasing naked ion size, it is not surprising that the $(E/N)_{\mathrm{c}}$ values determined from them would also progressively decrease, as the ratios in column II show. The precision on the graphically determined $(E/N)_{\mathrm{c}}$ is unfortunately not good enough to reliably establish a trend, neither as standalone values nor as ratios. The only thing that can be said is that the $(E/N)_{\mathrm{c}}$ ratios are larger than unity, seemingly not fitting the corresponding experimental K_0 values. The lack of an apparent high field effect for TMA^+ is interesting given that according to column I, if what is observed corresponds to the standard effect, then $(E/N)_{\mathrm{c}}$ for TMA^+ should be 1.36 times that of NH_4^+. This means that at the

latest, the high field effect should appear at around 82.90 Td for tetramethylammonium. Even though this value is at the end of the examined E/N range, the lack of change in K_0 is clear. This would confirm that the behavior observed for NH_4^+, MA^+ and DMA^+ is not due to the standard high field effect but to another effect, here attributed to increased clustering with decreasing methylation.

IV.4 Peptide characterization

IV.4.1 Collision cross-section and mobility of peptide ions

Peptide data acquired in our group with ESI-IM spectrometry was used here for molecular dynamics studies in order to characterize them but as well to establish a semi-automated collision cross-section estimation method. Instead of selecting amongst several candidate CCS values for one peptide, the novel approach here results in a single averaged collision cross-section value obtained by thermodynamic reweighting. The ISP collision cross-section prediction method was also applied to the peptide data set in order to verify its transferability to peptides not stemming from tryptic digestion, as in the original ISP method work, and as a comparison for the MD CCS values. The methods were then applied to peptides analyzed with IR-MALDI IM spectrometry. Mobility and collision cross-section values are given in table 6. The precision of the estimated values was arbitrarily chosen to match the experimental precision for comparison purposes.

Table 6: Experimentally determined reduced ion mobilities K_0 and collision cross-sections of the peptides compared to estimated CCS according to the intrinsic size parameter (Ω_{ISP}) and theoretical (Ω_{MD}) methods. Also given are the deviations from experimental and calculated collision cross-sections $\Delta\Omega_{exp-ISP} = |(\Omega_{exp} - \Omega_{ISP})/\Omega_{exp}|$ and $\Delta\Omega_{exp-MD} = |(\Omega_{exp} - \Omega_{MD})/\Omega_{exp}|$, respectively. Peptides are sorted according to their charge z. The intrinsic size parameter method is only valid up to a charge state of +3 so no Ω_{ISP} values could be determined for the peptide LLHLAVIGALLAVGATKVPRNQDWLGVSRQL.

z	Peptides	K_0 ($cm^2 \cdot V^{-1} \cdot s^{-1}$)	Ω_{exp} ($Å^2$)	Ω_{ISP} ($Å^2$)	$\Delta\Omega_{exp-ISP}$ (%)	Ω_{MD} ($Å^2$)	$\Delta\Omega_{exp-MD}$ (%)
1	DNDAN-NH_2	0.967 ± 0.002	216.64 ± 0.25	205.43	5.2	211.73	2.3
1	DNDPN-NH_2	0.937 ± 0.001	223.33 ± 0.52	206.85	7.4	219.16	1.9
1	NALPE	0.934 ± 0.008	224.23 ± 2.03	221.09	1.4	218.81	2.4
1	GRGDSP	0.907 ± 0.004	230.60 ± 0.97	229.85	0.3	226.87	1.6
1	GRADSP	0.905 ± 0.002	230.91 ± 0.56	236.15	2.3	231.96	0.5
1	GRGDNP	0.901 ± 0.001	231.86 ± 0.38	233.49	0.7	230.01	0.8
1	DNDRN-NH_2	0.888 ± 0.006	235.17 ± 1.63	230.56	1.8	245.63	4.4
1	ADLKIESS	0.714 ± 0.001	290.94 ± 0.38	294.55	1.2	286.90	1.4
1	VLDFAPPGA	0.707 ± 0.001	293.32 ± 0.34	296.42	1.1	293.65	0.1
1	AIENPADVS-NH_2	0.700 ± 0.001	296.49 ± 0.38	293.89	0.9	302.46	2.0
1	IVAIENPAD-NH_2	0.696 ± 0.001	298.09 ± 0.44	303.80	1.9	315.88	6.0
1	SIINFEKL-NH_2	0.650 ± 0.001	318.93 ± 0.44	321.74	0.9	311.56	2.3

1	GILGFVFTL-NH_2	0.640 ± 0.001	323.60 ± 0.38	323.37	0.1	311.77	3.7
1	GILGFVTFTL	0.639 ± 0.001	323.76 ± 0.38	343.05	6.0	321.58	0.7
1	EMGRAPLDL	0.636 ± 0.003	325.52 ± 1.59	327.37	0.6	324.03	0.5
2	AFFRHD-NH_2	1.525 ± 0.007	272.72 ± 1.34	298.51	9.5	301.77	10.7
2	GRGDSP	1.516 ± 0.013	275.89 ± 2.36	253.71	8.0	261.65	5.2
2	GRGDNP	1.498 ± 0.014	278.97 ± 2.54	256.18	8.2	263.39	5.6
2	GRADSP	1.491 ± 0.009	280.39 ± 1.66	258.13	7.9	255.92	8.7
2	KKGSKK-NH_2	1.441 ± 0.008	289.30 ± 1.65	268.65	7.1	298.84	3.3
2	ADLKIESS	1.396 ± 0.003	297.36 ± 0.69	305.83	2.8	315.28	6.0
2	RPKPQQ	1.381 ± 0.012	301.41 ± 2.59	287.44	4.6	304.83	1.1
2	KRHRK-NH_2	1.363 ± 0.009	305.58 ± 2.00	294.01	3.8	306.92	0.4
2	RLRSGRS-NH_2	1.224 ± 0.006	339.55 ± 1.60	309.85	8.7	326.12	4.0
2	SIINFEKL-NH_2	1.210 ± 0.015	342.49 ± 1.91	328.54	4.1	341.52	0.3
2	EMGRAPLDL	1.172 ± 0.027	353.56 ± 4.42	339.67	3.9	335.78	5.0
2	RAKFKQLL	1.156 ± 0.002	358.50 ± 0.61	340.72	5.0	372.40	3.9
3	KKGSKK-NH_2	1.612 ± 0.010	388.11 ± 2.42	385.01	0.8	411.31	11.7
3	KRHRK-NH_2	1.625 ± 0.018	384.30 ± 4.27	410.65	6.9	414.85	10.1
3	RLRSGRS-NH_2	1.477 ± 0.007	421.95 ± 1.89	414.49	1.8	441.55	13.1
3	RAKFKQLL	1.408 ± 0.003	441.43 ± 0.91	448.48	1.6	484.68	9.1
3	Ac-YGDSMDRIEKD RLQGMA-NH_2	1.082 ± 0.002	570.12 ± 0.90	627.60	10.1	652.04	6.2
4	LLHLAVIGALLAVGATKV PRNQDWLGVSRQL	0.781 ± 0.007	1,050.23 ± 9.13	Not available		1,138.10	12.1
5	LLHLAVIGALLAVGATKV PRNQDWLGVSRQL	0.943 ± 0.011	1,088.40 ± 12.31			1,189.15	11.5

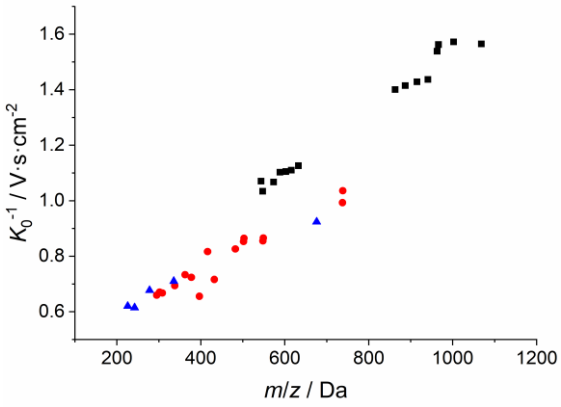

Figure 54: $1/K_0$ to m/z correlation of peptide ions. Black: z = 1, red: z = 2, blue: z = 3

The first observation to be made is that the inverse mobility K_0^{-1} linearly correlates with the mass-to-charge ratio m/z (Figure 54). Numerous studies have observed analogous trends for homologous series of low molecular weight substances [184]. At the same mass, significant deviations between charge states z can be seen. Through the Mason equation, K_0 depends on the charge state, but as well on the collision cross-section. Thus, at a given mass, double the charge does not result in half the K_0^{-1} due to the variation in collision cross-section.

The CCS of peptide ions depends on their mass, as a more massive ion should occupy more volume. In other words, a squared length dimension (CCS) correlates to a cubed length dimension (volume), which depends on the mass through the density [185]. The latter will depend on the substance class and structure. This implies that the CCS of the peptides will not follow the same rate of increase as the mass. In fact, an increase in mass doesn't even necessarily mean an increase in CCS, as shown below. In order to study the relation of the CCS and the mass, two plots were drawn up in figure 55. First, Ω_{exp} was potted against the mass of the corresponding peptide (left), then the relative CCS difference $\Delta\mathrm{CCS} = (\Omega_{\mathrm{exp},1} - \Omega_{\mathrm{exp},2})/\Omega_{\mathrm{exp},2}$ as a function of the relative mass difference $\Delta m = (m_1 - m_2)/m_2$ between every peptide was evaluated (right). Color coding according to the charge state difference $\Delta z = z_1 - z_2$ was added.

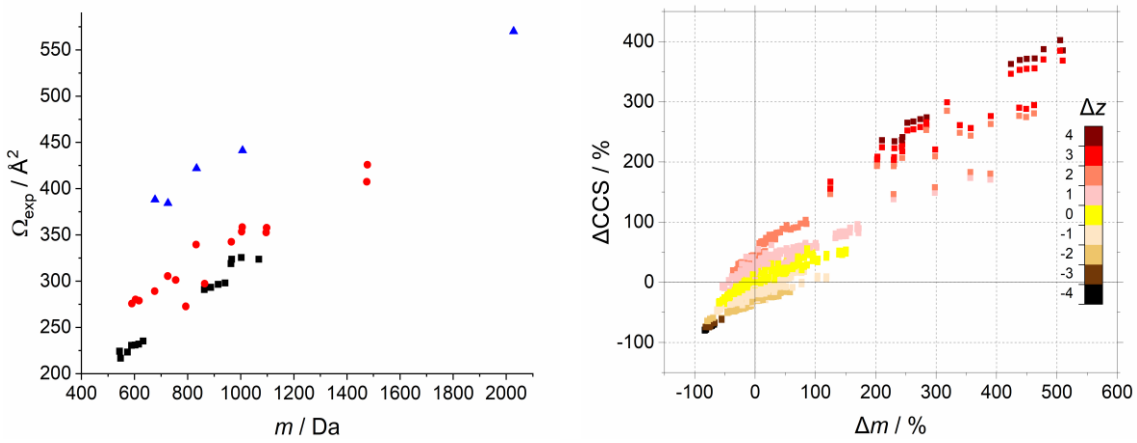

Figure 55: Left: Ω_{exp} vs m. Black: $z = 1$, red: $z = 2$, blue: $z = 3$. $z = 4$ and $z = 5$ excluded for clarity. Right: ΔCCS vs. Δm. The color map refers to the difference in charge states between the considered peptides $\Delta z = z_1 - z_2$

The graph on the left shows two trends. First, that the CCS seems to linearly increase with the mass for a given charge state. As mentioned above, the expected behavior should be that of a logarithmic function which describes the correlation of a squared length dimension with a cubed one [185]. The observed linearity is thus assumed to stem from the limited mass range of the available data set. The second trend is that for the same mass, a higher charge state leads to a higher observed CCS. This effect will be discussed later on. On the graph on the right, the relative mass and charge variations between every peptide are given in order to compare specific mass increases to their respective CCS increase. A general trend that ensues from the Ω_{exp} vs m correlation is that the higher the relative mass variation, the higher the relative CCS variation. Here, the logarithmic model seems to be valid as well, even though both ΔCCS and Δm are dimensionless quantities. An interesting area is where the signs of ΔCCS and Δm are opposite, which implies that sometimes a variation in mass (increase or decrease) can lead to the opposite variation in CCS (decrease or increase). Furthermore, the peptides seem to be clustered according to a given charge state difference Δz. Even for the zones of opposite variation between ΔCCS and

Δm, it seems that at the same Δm, a variation in charge state (increase or decrease) brings about the same type of variation in ΔCCS (increase or decrease), which echoes the trend in Ω_{exp} vs m.

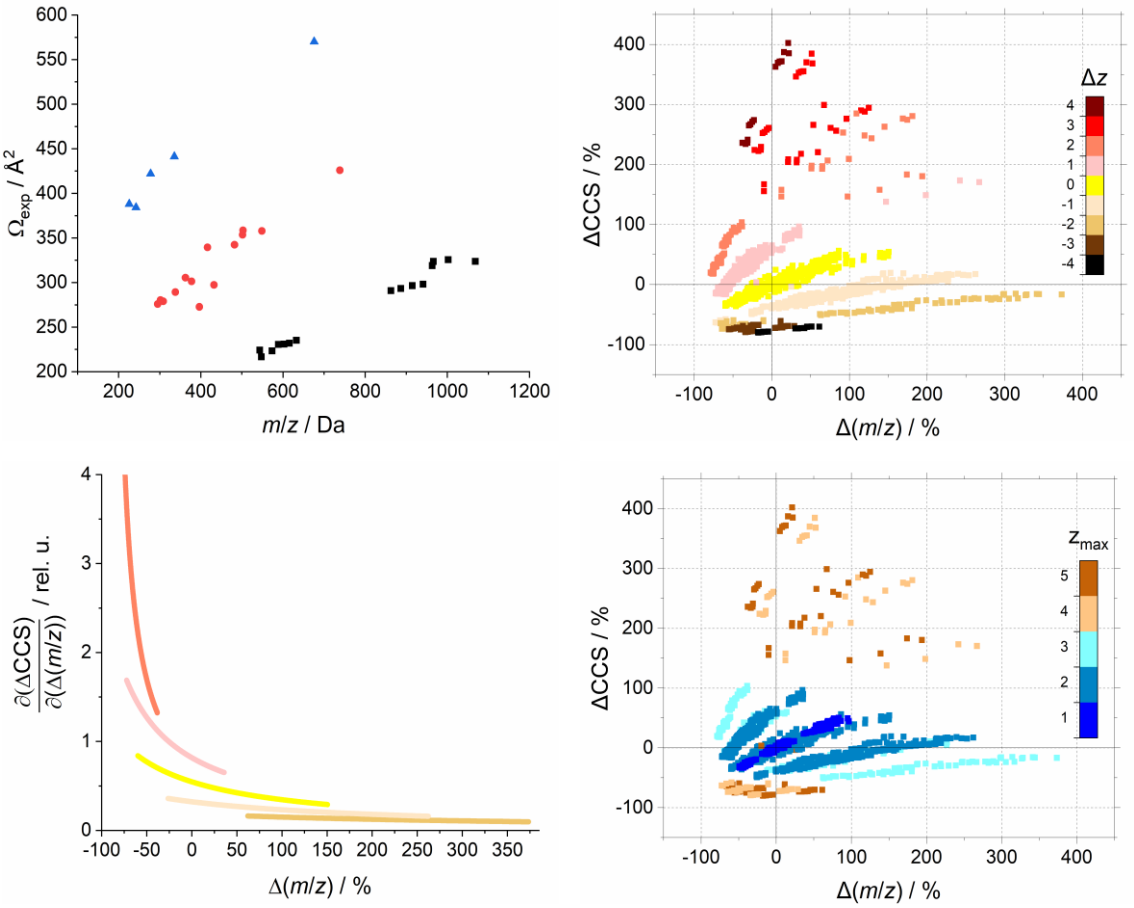

Figure 56: Top left: Ω_{exp} vs m/z Black: $z = 1$, red: $z = 2$, blue: $z = 3$. $z = 4$ and $z = 5$ excluded for clarity. Top right: ΔCCS vs. $\Delta(m/z)$. The color map refers to the difference in charge states between the considered peptides $\Delta z = z_1 - z_2$. Bottom Left: Derivatives of the logarithmic fits corresponding to Δz of -2 to +2 data sets, peptides with charge states $z = 4$ and $z = 5$ are exluded. Bottom right: Same as top right but color coded according to the maximum considered charge state in $\Delta(m/z)$ such that $z_{max} = max(z_1, z_2)$

If Ω_{exp} is plotted against m/z, the difference in charge states is immediately visible (Figure 56, top left). Such plots are common practice in IM-MS and enable the separation of charge states but as well of substance classes [186]. In the top right-hand graph of figure 56, the relative CCS variation, Δ CCS, is also plotted against the relative difference in mass-to-charge ratios $\Delta(m/z) = ((m/z)_1 - (m/z)_2)/(m/z)_2$. Here as well, an increase in $\Delta(m/z)$ will result in an increase in ΔCCS. This plot is identical to the bottom right one, except there the color code refers to the maximum peptide charge state considered in $\Delta(m/z)$. The scattered data on the top of the plot as well as the grouped data at the very bottom (both in brown) correspond to the relative mass-to-charge and CCS variations with the +4 and +5 peptide charge states. Since there was only the peptide LLHLAVIGALLAVGATKVPRNQDWLGVSRQL that was in either charge state, the sparse data is not enough to establish a trend. That's why LLHLAVIGALLAVGATKVPRNQDWLGVSRQL was excluded from the following discussion.

The ΔCCS vs $\Delta(m/z)$ data in the right-hand plots of figure 56 was fitted with a general logarithmic function of the form

$$y = a - b\ln(x + c) \tag{57}$$

for charge state differences Δz from -2 to +2. Data points relating to the +4/+5 charged peptide were excluded. The fit parameters, as well as the $\Delta(m/z)$ intervals containing the data points used for the fits are given in table 7.

Table 7: Fit parameters for the ΔCCS vs $\Delta(m/z)$ data grouped according to Δz with their respective $\Delta(m/z)$ intervals

	a	***b***	***c***	**Interval**
-2	-522.51	-76.50	407.89	[63;374]
-1	-498.00	-82.90	256.72	[-27;263]
0	-483.64	-94.07	171.99	[-61;151]
+1	-503.92	-114.68	140.29	[-73;36]
+2	-178.23	-70.85	91.85	[-79;-39]

The derivative of (57) is

$$\frac{\mathrm{d}y}{\mathrm{d}x} = -\frac{b}{x + c}\ , \tag{58}$$

which is the form used in the bottom left plot of figure 56. Over the corresponding data intervals, the derivative of $\Delta z = 2$ is always larger than that of $\Delta z = 1$, which is in turn larger than that of $\Delta z = 0$ and so on. This confirms the trend that was already visible in the top right plot of figure 56: the larger Δz, the larger the variation in ΔCCS will be with the same variation in $\Delta(m/z)$. This means that the cross-section difference between two peptides increases at a higher rate the more their charge states differ. One important point is that if the derivative curves are extrapolated beyond the intervals of the data that was fitted, it seems that charge state differences from -2 to +1 stay in the same order but that +2 is overtaken by the others. This is however thought to be due to the narrow $\Delta(m/z)$ interval over which the data was fitted and could be potentially corrected with more data points.

A few examples of relative collision cross-section and mass differences are given in figure 57 for selected peptide pairs with equal charge, where $\Delta m = \Delta(m/z)$. The section labeled singly charged corresponds to the intersect of $\Delta z = 0$ with $z_{\max} = 1$ and doubly charged to $\Delta z = 0$ and $z_{\max} = 2$. As is visible from the right-hand plots in figure 56 as well, the singly charged peptides usually differ more in mass than in cross sections. Various examples are visible in figure 57. A typical case is that of GRGDSP/GRADSP, which vary only in one amino acid: alanine (A) instead of glycine (G). The difference between the two is a $–CH_3$ substitution of the C_α, which translates into a simple mass increase with a straightforward increase in CCS. An interesting pair is SIINFEKL-NH_2/GILGFVFTL-NH_2, where the mass varies less than the cross-section. The two have in fact very similar masses but different structures. To begin with, GILGFVFTL-NH_2 has one more amino acid, which means that it will have a longer backbone and thus a more linear structure.

Furthermore, SIINFEKL-NH_2 has more linear amino acid side chains (S, N, E, K), with only one quarter branched amino acids (I, L), whereas in GILGFVFTL-NH_2 more than half the amino acids are branched (I, L, T, V). GILGFVFTL-NH_2 also has two amino acids with an aromatic ring in their side chain (F), whereas SIINFEKL-NH_2 only has one (F). The increased branching and the additional aromatic ring would thus result in steric hindrances in GILGFVFTL-NH_2, extending the backbone and leading to a larger cross section. The peptide pair NALPE/DNDAN-NH_2 belongs to the case where $\Delta m > 0$ and $\Delta CCS < 0$. The mass of NALPE is 4 Da lower than that of DNDAN-NH_2 but its cross section is 7.6 $Å^2$ larger. An explanation can be that DNDAN-NH_2 has side chains with more heteroatoms, which results in more hydrogen bonding, leading to a more compact structure. This was studied with the hydrogen bond tool in GROMACS 5.1.1. The high temperature trajectories showed that DNDAN-NH_2 forms 57.5 % more hydrogen bonds than NALPE. Thus, in this case hydrogen bonding has a larger influence on the CCS than the increasing mass. A similar reasoning might be applied in the case of the GRADSP/GRGDNP peptide pair when comparing the doubly to the singly charged. The CCS of both peptides increases with the additional charge, but by a different amount. This results in in a trend inversion for ΔCCS with regard to Δm when moving from the singly to the doubly charged peptides. The relative difference is however quite low, as the peptides are small and have very similar structures.

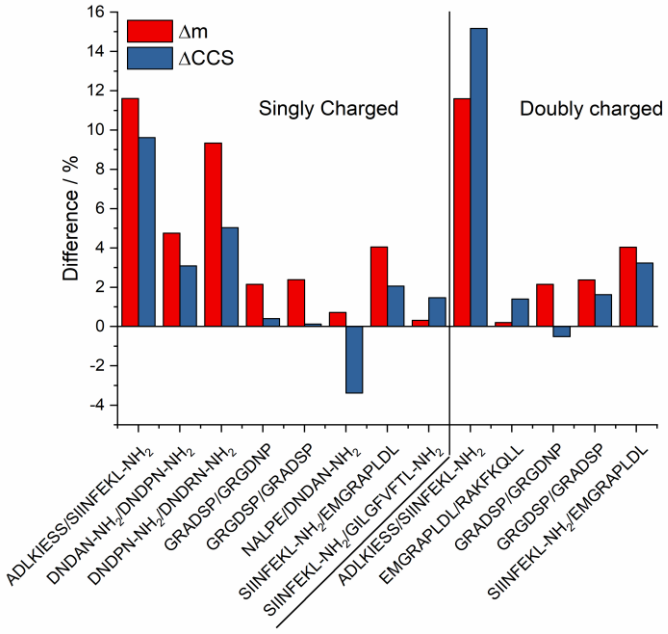

Figure 57: Relative differences (in %) of the masses (Δm, red bars) and CCS (ΔCCS, blue bars) of selected peptide pairs

Otherwise, when the same peptide pairs are compared between the singly and doubly charged states, a mass increase which is virtually identical leads to a larger collision cross-section increase in the case of the doubly charged peptides. This is observed for ADLKIESS/SIINFEKL-NH_2, GRGDSP/GRADSP and SIINFEKL-NH_2/EMGRAPLDL. The reasoning is that the additional charge leads to the stretching of peptide through Coulomb repulsion on the one hand and on the other hand more charges also mean stronger interactions between the ion and the nitrogen drift gas through the potentials as described in equations 35 and 36. Both effects lead to larger cross sections for peptides with a higher charge state. The difference between the increase in cross

section for each peptide would then stem from the structure. For example, the CCS of ADLKIESS changes from 290.94 Å² to 297.36 Å² (2.2 % increase) and that of SIINFEKL-NH_2 increases from 318.93 Å² to 342.49 Å² (7.4 % increase). However, singly charged SIINFEKL-NH_2 has an 8.8 % larger CCS than singly charged ADLKIESS and doubly charged SIINFEKL-NH_2 has a 13.2 % larger CCS than doubly charged ADLKIESS. This can be explained by the fact that the charge centers are further apart in SIINFEKL-NH_2 than in ADLKIESS, so the stretching by Coulomb repulsion would be able to be larger in the former than the latter. Of course, for larger peptides if the charges are too far apart then no interaction takes place, due to the fact that the Coulomb potential scales as $1/r$ (Equation 8).

IV.4.2 Comparison of ISP and MD-based methods

What is visible through all of the previous discussion is that the structure of the peptide, and thus its sequence of amino acids, is a determining factor in the collision cross-section. This principle is what the empirical intrinsic size parameter (ISP) method is based on, whereas molecular dynamics (MD) preserves structural information. Both methods were used in order to estimate the collision cross-section of the analyzed peptides. The results of the ISP-derived CCS, Ω_{ISP}, and of the MD-derived CCS, Ω_{MD}, are given in table 6, as well as the respective deviations with regard to the experimental cross section, $\Delta\Omega_{\mathrm{exp-ISP}}$ and $\Delta\Omega_{\mathrm{exp-MD}}$. If the deviations fall below 2 % then the estimated value is deemed to be in good agreement for most experiments. The only exception are high-resolution drift tubes. If they are above 5 % then they cannot be reliably used for CCS prediction. The proportion of peptides for which $\Delta\Omega_{\mathrm{exp-ISP}}$ and $\Delta\Omega_{\mathrm{exp-MD}}$ fall into the respective criteria is given in table 8. Note that despite the numerous papers on the ISP method, a set of parameters for charge states over +3 is yet to be derived. Thus, the ISP method as it is can only be applied to charge states of +3 and under.

Table 8: Percentage of peptides for which the deviation between the estimated and the experimentally-derived collision cross-section values lie below or above certain threshold values for what is considered a good approximation (≤ 2 %) and a deviation which is too high (> 5 %)

	$\leq \mathbf{2}$ %		$> \mathbf{5}$ %	
	$\boldsymbol{\Delta\Omega_{\mathrm{exp-ISP}}}$	$\boldsymbol{\Delta\Omega_{\mathrm{exp-MD}}}$	$\boldsymbol{\Delta\Omega_{\mathrm{exp-ISP}}}$	$\boldsymbol{\Delta\Omega_{\mathrm{exp-MD}}}$
+1	73 %	60 %	25 %	8 %
+2	0 %	25 %	58 %	50 %
+3	60 %	0 %	40 %	100 %
+4, +5	--	0 %	--	100 %

In the case of $\Delta\Omega_{\mathrm{exp-MD}}$ for charge states +3 and higher, all estimated peptide cross sections show a deviation over 5 % due to the fact that the correction factor applied to the MD values (Figure 19) was based only on +1 and +2 charge states. Only five triply charged peptides and one other peptide which presented both charge states of +4 and +5 were analyzed in these experiments, which was not enough to establish a correction. More data would be needed, either to refine the correction or to establish a separate one for higher charge states. Furthermore, the initial systematic overestimation of Ω'_{MD} with regard to Ω_{exp} might be tracked back to a few factors.

One of them would be the use of the N_2 version of MOBCAL, which was parametrized for small drug-like molecules in the CCS range 107.4–231.4 Å^2 [127]. These were mostly small aromatic molecules (rigid) or small ammonium ions (flexible) and their dimers. The largest cross sections ($\Omega > 186$ Å^2) correspond to fullerenes. The parametrization might then perhaps not entirely fit larger, flexible biopolymers such as peptides, composed of a rather rigid backbone and more flexible side chains. Although the interactions with He have been successfully modelled, the interactions with nitrogen are more complex and still in need of refinement. The other source of error might be the use of the partial charges corresponding to the semi-empirical MD force field charges in MOBCAL as well. These are highly dependent on the force field family and will influence the interaction with the drift gas. Ab-initio charge calculations should be performed, but for large molecules the calculation becomes too expensive, especially considering the case of a large data set. Further improvements would also be possible by precisely determining the most frequent protonation site of peptides in undefined cases instead of using an average. Finally, more data might be needed to establish a good correlation, which should then be ideally evaluated on a second, independent data set.

For the ISP-derived CCS values, a few sources of error may exist. First, the error might stem from the polyalanine regression curve or from variation in the ISP. Furthermore, the transfer of cross-section values from one spectrometer to another, under different conditions, might lead to error (one source for the polyalanine regression and two other sources for the different ISP sets). Various ISP sets were obtained by the Clemmer group for different collections of peptides obtained by tryptic digestion of proteins [166,169,171,172,187]. This means that their terminal amino acid was always either lysine or arginine, both groups having a different set of ISP. In the case of synthetically produced peptides, the structural variability of the end groups is much higher. A generalized set of ISP, or perhaps a series of subsets would probably need to be derived. Furthermore, although the ISP data set from Valentine et al. [166] is suitable for a large part of the peptides under investigation, it was not possible to find an ISP data set for doubly charged peptides which led to good agreement between Ω_{ISP} and Ω_{exp}. This might be due to sequence-dependent effects which influence the 3D structure of the peptides. Hydrogen bonding, the number of heteroatoms, the partial charges and the relative position of the different amino acids with regard to each other might thus play a role. That being said, even though the ISP method is coarser in nature than the MD method, it has proven to still be robust. This is no doubt due to the large datasets on which it is based, with hundreds of peptides at a time. With enough data, a robust MD method could be established as well, with the added benefit of structural information which could then be incorporated into a more nuanced model.

One example of the advantage of the structural information provided by an MD-based method over the ISP method is in the case of peptide isomers. The ISP are derived only for a given sequence of amino acids, and thus would give the same cross section value for two isomeric peptides, even though IM spectrometry would distinguish between them. Another example is cyclization, which takes place for cysteine-containing peptides in the presence of oxygen. Very similar masses result in very different structures, which the ISP method does not account for. Two peptides were used to illustrate cyclization, CRRETAWAC and Ac-ACTERMAAHNLCGG-NH_2. Each contains two

cysteines, with seven and nine amino acids between them, respectively. The mobility and collision cross-section values for each isomer form are given in table 9. The cyclic peptides have higher mobilities, which stem from a smaller collision cross-section as the cyclization leads to a more compact structure.

Table 9: Ion mobilities of CRRETAWAC and Ac-ACTERMAAHNLCGG-NH_2 in the cyclic and linear state; experimentally determined cross sections Ω_{exp} of the peptides compared to estimations by the increment method Ω_{ISP} and the molecular dynamics method Ω_{MD}

z	Peptide	Form	K_0 ($cm^2 \cdot V^{-1} \cdot s^{-1}$)	Ω_{exp} ($Å^2$)	Ω_{ISP} ($Å^2$)	$\Delta\Omega_{exp-ISP}$ (%)	Ω_{MD} ($Å^2$)	$\Delta\Omega_{exp-MD}$ (%)
2	Ac-ACTERMAA-HNLCGG-NH_2	cyclic	1.007 ± 0.003	407.50 ± 1.63	399.11	2.1	409.04	0.4
2	Ac-ACTERMAA-HNLCGG-NH_2	linear	0.965 ± 0.003	425.90 ± 1.65	399.11	6.3	426.59	0.2
2	CRRETAWAC	cyclic	1.169 ± 0.005	352.60 ± 2.26	338.50	4.0	342.80	2.8
2	CRRETAWAC	linear	1.155 ± 0.005	357.90 ± 1.62	338.50	5.4	357.59	0.1

The experimentally-determined collision cross-sections of the peptide CRRETAWAC in its linear and cyclic form differ only by 5.3 ± 3.88 $Å^2$, as opposed to 18.4 ± 3.28 $Å^2$ for Ac-ACTERMAAHNLCGG-NH_2. While the difference in the case of the latter is enough to see a clear separation between the doubly charged ion peaks of the linear and cyclic forms (Figure 58, left), the small difference in the case of CRRETAWAC can only be seen as a slight shift in the doubly charged ion peak center (Figure 58, right).

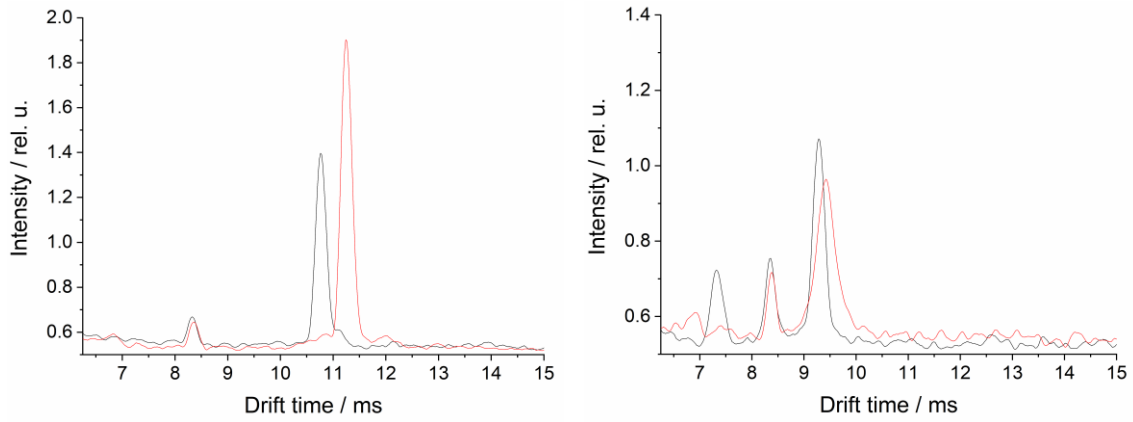

Figure 58: IM spectra of the linear (red) and cyclic (black) peptide variants of Ac-ACTERMAAHNLCGG-NH_2 (left) and CRRETAWAC (right). Solvent cluster ion peak not shown

The significance of the shift is however verified by the constant drift time of the TBA^+ peak in both spectra. As discussed above, the presence of two charges leads to a stretching of the peptide through Coulomb repulsion. Cyclization would work against this effect. However, In the case of CREETAWAC, the two charges would be on the contiguous arginine residues, which cannot lead to stretching. Thus, the lack of a strong difference between the linear and cyclic doubly charged CRRETAWAC peptide peaks is due to a lack of electrostatic repulsion stretching in the linear form. This is not the case for Ac-ACTERMAAHNLCGG-NH_2. Furthermore, in the case of CRRETAWAC the

linear peptide peak is noticeably broader (about 50 % broader) than the cyclic peptide peak. This might be due to the larger freedom of movement of the linear forms, and thus to a larger conformational space, which would in turn translate as a larger CCS variation. The RMSD and RMSF of both forms throughout their high temperature simulations were examined. The results are given in table 10. The RMSD corresponds to the comparison of each frame in the high temperature simulation against every other. The mean RMSD value of the linear form exceeds that of the cyclic form, which means that the frames in the linear structure simulation of CRRETAWAC differ more from each other, on average, than in that of the cyclic form. This higher conformational variability could then result in a larger cross-section variability and a broader peak in IM spectrometry. This is supported by the fact that the average atomic RMSF for the linear form is also higher. This means that the atoms of the linear peptide, in general, move about their average position more than those of the cyclic form.

Table 10: Mean RMSD and RMSF for the cyclic and linear forms of the peptides CRRETAWAC and Ac-ACTERMAAHNLCGG-NH_2

		Mean RMSD (nm)	**Mean RMSF (nm)**
CRRETAWAC	*Cyclic*	0.493	0.354
	Linear	0.566	0.419
Ac-ACTERMAAHNLCGG-NH_2	*Cyclic*	0.556	0.407
	Linear	0.608	0.506

The average RMSF values for Ac-ACTERMAAHNLCGG-NH_2 were higher than for CRRETAWAC, no doubt due to its larger size resulting in more degrees of freedom. Both the mean RMSD and the average RMSF were higher for its linear form. However, the RMSD was increased by 15 % in the case of CRRETAWAC from the cyclic to the linear form, whereas for Ac-ACTERMAAHNLCGG-NH_2 the increase was only of 9 %. This might be the reason why the peak broadening is more pronounced for CRRETAWAC.

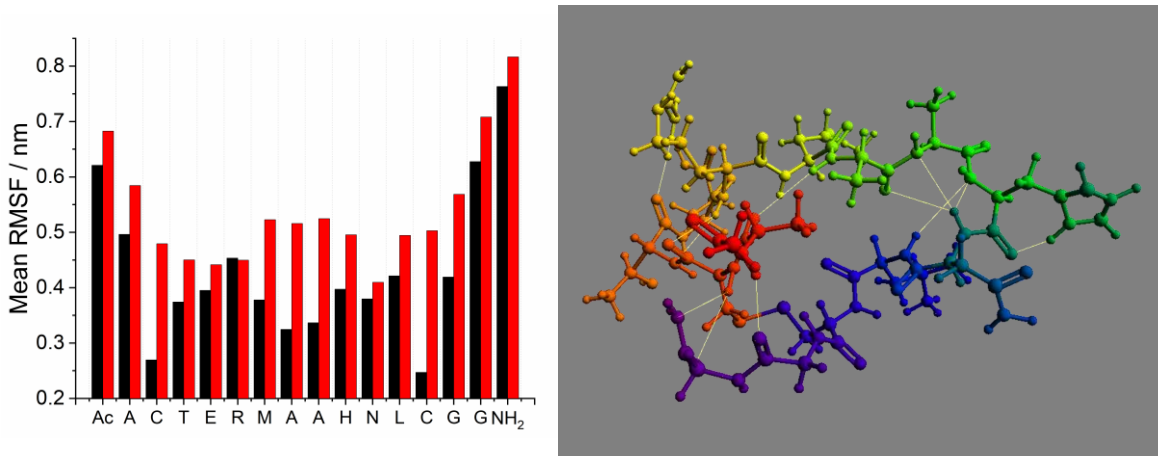

Figure 59: Left: Average RMSF values for each residue in Ac-ACTERMAAHNLCGG-NH_2 for the linear (red) and cyclic (black) forms of the peptide. Right: Cyclic Ac-ACTERMAAHNLCGG-NH_2 structure showing hydrogen bonds in yellow. Color coded according to residue number, from Ac- (red) to -NH_2 (purple)

A breakdown of the average RMSF per amino acid of Ac-ACTERMAAHNLCGG-NH_2 in figure 59 shows how cyclization greatly restrains the movement of the cysteines, but also of the alanines at the opposite end of the ring, followed by histidine and methionine on each side. The tension due to the formation of the cyclic structure must then be on these two points, the rest of the peptide

retaining some freedom of movement. The hydrogen bond analysis of the linear and cyclic forms of Ac-ACTERMAAHNLCGG-NH_2 showed that there are 3.6 % more hydrogen bonds formed in the cyclic than in the linear form, which also contributes to its stabilization. These hydrogen bonds are visible as yellow lines in the cyclic Ac-ACTERMAAHNLCGG-NH_2 structure in figure 59. The amino acids are color coded from red to purple according to their position in the peptide chain. The orange-violet covalent bond corresponds to the disulfide bond and the bright green residues on the opposite end to the alanines, with methionine and histidine (with its 5-atom ring) on each side. What is clear is that hydrogen bonding between opposite ends of the peptide (warm and cold colors) occurs in the cyclic form due to the proximity of the respective residues, which is due to the disulfide bond and would not occur for the linear form. Thus, the cyclic form is stabilized with regard to linear one.

IV.4.3 IR-MALDI of peptides

The reduced pressure IM spectrometer was employed for the analysis of peptide ions with IR-MALDI. With this spectrometer, high signal intensities with good resolution were obtained, making it possible to determine the reduced mobility of various peptide ions through the mobility standard TBAB. Various peptide solutions, doped with TBAB, were analyzed with the two variations of the RP spectrometer under conditions ranging from 50 to 250 mbar and 6.49 to 20.28 Td. Figure 60 shows an example of a peptide spectrum at reduced pressure using the RP ionization RP spectrometer for the analysis of KRHRK-NH_2. A spectrum of pure TBAB measured under the same conditions is also given as reference.

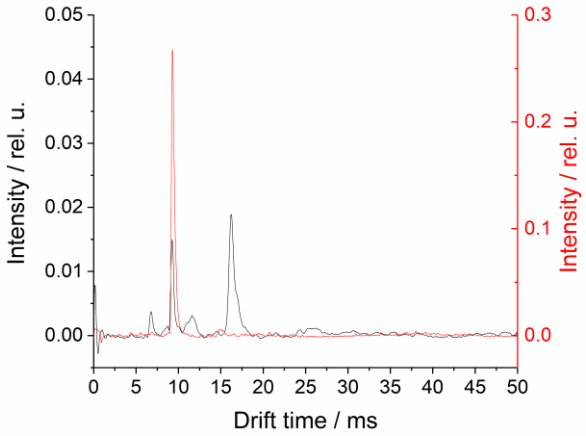

Figure 60: 500 µM KRHRK-NH_2 with 1µM TBAB (black) and pure 10 µM TBAB (red) for comparison. Solvent ACN/H_2O 1:1. Pressure 250 mbar. E/N = 6.49 Td. -923 V·cm^{-1} closing field, PA = 2 kV·cm^{-1}, PD = 0 µs. PW peptide: 300 µs, PW TBAB: 800 µs

The resulting peptide mobility values were then compared to the ESI results in table 6 at atmospheric pressure and given in table 11. The K_0 values are in good agreement between both ionization techniques, which are in fact complementary in many cases. Furthermore, the observed values clearly show that no matter the peptide, IR-MALDI produces mostly singly charged species. This would facilitate spectral analysis in the case of complex mixtures through simplified peak attribution (one peak per substance).

Table 11: Mobility values in $cm^2 \cdot V^{-1} \cdot s^{-1}$ for different peptides. In IR-MALDI values determined at E = 375 $V \cdot cm^{-1}$ and 250 mbar. Between two and three values averaged for each peptide. For ESI, values determined at atmospheric pressure

	K_0 IR-MALDI ($cm^2 \cdot V^{-1} \cdot s^{-1}$)	K_0 ESI ($cm^2 \cdot V^{-1} \cdot s^{-1}$)		
	M^+	M^+	M_2^+	M_3^+
ADLKIESS	0.763 ± 0.019	0.714 ± 0.001	1.396 ± 0.003	
AFFRHD-NH_2	0.793 ± 0.003		1.525 ± 0.007	
AIENPADVS-NH_2	0.701 ± 0.001	0.700 ± 0.001		
GRGDNP	0.913 ± 0.009	0.901 ± 0.001	1.498 ± 0.014	
KRHRK-NH_2	0.751 ± 0.004		1.363 ± 0.009	1.625 ± 0.018
NALPE	0.923 ± 0.003	0.934 ± 0.008		
RLRSGRS-NH_2	0.693 ± 0.013		1.224 ± 0.006	1.477 ± 0.007
RPKPQQ	0.780 ± 0.018		1.381 ± 0.012	
SIINFEKL-NH_2	0.688 ± 0.013	0.650 ± 0.001	1.210 ± 0.015	
VLDFAPPGA	0.716 ± 0.006	0.707 ± 0.001		

Table 12: Experimentally determined reduced ion mobilities K_0 and collision cross-sections of the peptides analyzed with IR-MALDI and comparison to estimated CCS according to the intrinsic size parameter (Ω_{ISP}) and molecular dynamics-based (Ω_{MD}) methods. Also given are the deviations from experimental and calculated collision cross-sections $\Delta\Omega_{exp-ISP} = \left|(\Omega_{exp} - \Omega_{ISP})/\Omega_{exp}\right|$ and $\Delta\Omega_{exp-MD} = \left|(\Omega_{exp} - \Omega_{MD})/\Omega_{exp}\right|$, respectively

z	Peptides	K_0 ($cm^2 \cdot V^{-1} \cdot s^{-1}$)	Ω_{exp} (Å²)	Ω_{ISP} (Å²)	$\Delta\Omega_{exp-ISP}$ (%)	Ω_{MD} (Å²)	$\Delta\Omega_{exp-MD}$ (%)
1	ADLKIESS	0.763 ± 0.019	278.37 ± 6.91	294.87	5.9	286.90	3.1
1	AFFRHD-NH_2	0.793 ± 0.003	268.07 ± 1.04	278.18	3.8	281.15	4.9
1	AIENPADVS-NH_2	0.701 ± 0.001	302.76 ± 0.58	294.00	2.9	302.46	0.1
1	GRGDNP	0.913 ± 0.009	234.00 ± 2.33	233.49	0.2	230.01	1.7
1	KRHRK-NH_2	0.751 ± 0.004	283.57 ± 1.35	299.86	5.7	276.54	2.5
1	NALPE	0.923 ± 0.003	232.25 ± 0.65	221.15	4.8	218.81	5.8
1	RLRSGRS-NH_2	0.693 ± 0.013	306.82 ± 5.62	311.57	1.5	295.71	3.6
1	RPKPQQ	0.780 ± 0.018	273.13 ± 6.55	277.91	1.8	266.23	2.5
1	SIINFEKL-NH_2	0.688 ± 0.013	308.14 ± 5.86	321.88	4.5	311.56	1.1
1	VLDFAPPGA	0.716 ± 0.006	296.52 ± 2.29	296.55	0.0	293.65	1.0
1	RPPGFSPFR	0.6700 ± 0.0006	309.02 ± 0.26	342.51	10.8	312.04	1.0
2	RPPGFSPFR	1.176 ± 0.002	351.98 ± 0.68	340.92	3.1	344.73	2.1

The collision cross-section of the peptides was then theoretically calculated through the ISP method as well as the MD-based method as above, giving the results in table 12. The deviations with regard to the experimental values are similar to those in table 7. Thus, the combination of IR-MALDI with ion mobility spectrometry and a molecular dynamics-based approach for the analysis of peptides has been successful. External validation with bradykinin (RPPGFSPFR), a peptide not present in the original data set, was also carried out with good results. The structures

taken for the given Ω_{MD} values of bradykinin were the zwitterions[9], according to the literature [188,189]. These were also the structures which were in best agreement with the experimental collision cross-sections.

Indeed, the collision cross-sections of the non-zwitterionic isomers of the singly and doubly-charged bradykinin peptide were also calculated with the MD method, with deviations with regard to the experimental CCS which were +6.7 % for the doubly charged peptide and +6.4 % and +10.7 % for the singly charged peptide, protonated at the C-terminal and N-terminal arginine, respectively. That the Ω_{MD} values for the non-zwitterionic isomers are larger than those of the zwitterions is explained by the tendency of the bradykinin zwitterions to fold around the charge centers into a globular structure, as ab initio studies have shown [188,189]. The extra charge in the zwitterions promotes hydrogen bonding, as seen in figure 61, thus leading to a more compact structure. Indeed, in both singly and doubly charged peptides, the non-zwitterionic forms appear as extended chains, while interactions between the terminal amino acids in the zwitterions lead to a backbone that folds back around itself, and thus ultimately to a smaller collision cross section.

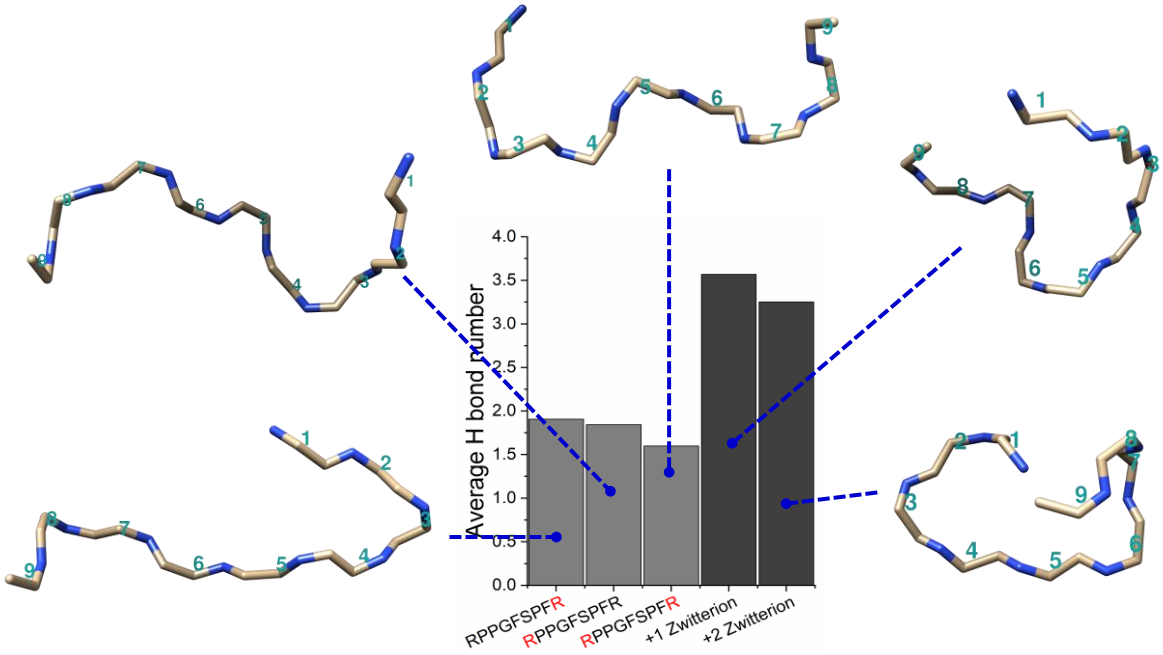

Figure 61: Average hydrogen bond number per bradykinin structure, represented only through the backbone atoms. The residues in RPPGFSPFR are numbered from 1 to 9. In the non-zwitterionic isomers, the charged arginine is marked in red. The charge was placed on the guanidinium group

While the experimental collision cross-section of bradykinin increases with the charge by 13.9 %, it is worth noting that the ISP predicts CCS values which are very similar to each other, with a decrease of 0.5 %. The MD method, on the other hand, predicts and increase of 10.5 % with the additional charge, which is in much better agreement with the experimental data. These observations suggest that it could be possible to carry out structure attribution with the method, at least in the present case. Ideally, structural changes could be systematically correlated to

[9] A zwitterion is a molecule or ion with two or more functional groups out of which at least one is negatively charged and at least one is positively charged

changes in collision cross-section and mass. This is partly what the ISP method has tried to do, but it remains a coarse approach. Based on hundreds and hundreds of peptides, it has become mostly reliable through pure statistics. It cannot, however, account for the specific effect of structural changes or sequence-specific variations on the collision cross-section, which is what an MD-based approach could potentially achieve.

V. Outlook

The characterization of the ionization source and of the dispersion process in IR-MALDI enabled the methodical optimization of the spectrometer for analytical purposes. Understanding how the variation of different analytical parameters affected the end spectra was only possible in the context of a well-defined ionization process. Integrating information from both analytical optimization and dispersion process also shed some light on the transport of ions from the ionization source to the drift tube. Now, three spectrometer variations have been established: a well-rounded and robust analytical technique at atmospheric pressure and two variations of a reduced pressure technique which are complementary in terms of resolution and sensitivity. Nonetheless, they can both be used analytically as well as for fundamental high field mobility studies. In the case of peptides, a molecular dynamics-based approach for the determination of their collision cross-sections was established with an independent data set, based on ESI-IM analyses. Its validation with the IR-MALDI-IM techniques developed in this work was successfully carried out, showing good accuracy but also the advantage of structural information with regard to data interpretation.

Now that the specifics of the coupling of IR-MALDI with ion mobility spectrometry, such as desolvation and ion transfer problematics, have been pinned down, work in our group has been focusing on the coupling of IR-MALDI to differential mobility analysis (DMA). The latter is a technique for the separation of charged aerosol particles in the nanometer range according to their mobility in an electric field and a perpendicular gas stream. The IR-MALDI-DMA analysis of saccharose solutions can be used to determine the initial size distribution of the droplets stemming from the dispersion process, which is crucial for desolvation, ion release and the ionization process.

Preliminary data on the high field mobility of bradykinin in nitrogen has also been acquired, possibly showing a different high field behavior between the singly and doubly charged species. Work has also begun on the high field mobility of the ammonium ions in helium. Thus, the collision cross-section of various clusters can be calculated and compared to the experimental results. Calculations of binding energies with ab-initio methods could also shed some light on the observed declustering under high field conditions.

In the future, the analysis of peptides could be extended to mixtures by coupling IR-MALDI-IM spectrometry to HPLC. Thus, the combination of the experimental techniques and the MD-based collision cross-section prediction method could be used for routine analysis and quality control of synthesized peptides.

Further work on the MD-based CCS prediction method could focus on employing the reweighting approach with helium CCS calculations, which is more accurate than nitrogen. Comparing the thermodynamically reweighted CCS to helium data would thus enable the independent validation of the approach. Another focus could be on the dataset used to establish the method and expanding it to other substance classes, with different CCS vs mass correlations. Complex mixtures of different singly-charged substance classes could then be easily analyzed with IM-MS, for example, and the results directly related to structural and sequence-dependent properties. For

such an analysis to be possible, the dataset on which the MD method is based needs to be expanded. Integrating results from different ionization sources might as well improve the method. Mostly, a detailed and systematic study of sequence-dependent effects should be carried out, in order to make sure that the basis dataset covers them in an adequate manner. The automation of the MD-based method could be completed, thus opening the door for large scale implementation. The advantage of the latter would be the integration with existing datasets from different sources, as well as information obtained from the simulation trajectory, such as H bonding, RMSD matrix, RMSF, dihedral angles, which in combination with machine learning could establish links between sequence, structure and experimentally-observed features. Optimistically, such a “big data” approach could even result in probabilistic structure prediction based on experimental results.

VI. References

[1] G.A. Eiceman, Z. Karpas, H.H. Hill, Jr., Ion Mobility Spectrometry, Third Edition, CRC Press, 2013.

[2] M. Dole, L.L. Mack, R.L. Hines, R.C. Mobley, L.D. Ferguson, M.B. Alice, Molecular Beams of Macroions, J. Chem. Phys. 49 (1968) 2240–2249. doi:10.1063/1.1670391.

[3] M. Yamashita, J.B. Fenn, Electrospray ion source. Another variation on the free-jet theme, J. Phys. Chem. 88 (1984) 4451–4459. doi:10.1021/j150664a002.

[4] M. Karas, F. Hillenkamp, Laser Desorption Ionization of Proteins with Molecular Masses Exceeding 10 000 Daltons, Anal. Chem. 60 (1988) 2299–2301. doi:10.1021/ac00171a028.

[5] K. Tanaka, H. Waki, Y. Ido, S. Akita, Y. Yoshida, T. Yoshida, T. Matsuo, Protein and polymer analyses up to m/z 100 000 by laser ionization time-of-flight mass spectrometry, Rapid Commun. Mass Spectrom. 2 (1988) 151–153. doi:10.1002/rcm.1290020802.

[6] C.B. Shumate, H.H. Hill, Coronaspray Nebulization and Ionization of Liquid Samples for Ion Mobility Spectrometry, Anal. Chem. 61 (1989) 601–606. doi:10.1021/ac00181a021.

[7] R.H. St. Louis, H.H. Hill, G.A. Eiceman, Ion Mobility Spectrometry in Analytical Chemistry, Crit. Rev. Anal. Chem. 21 (1990) 321–355. doi:10.1080/10408349008050848.

[8] M. Zühlke, Elektrosprayionisation Ionenmobilitätsspektrometrie – Entwicklung , Charakterisierung und Anwendung zur HPLC-Detektion und zum Reaktionsmonitoring, Universität Potsdam, 2017.

[9] G. von Helden, T. Wyttenbach, M.T. Bowers, Inclusion of a MALDI ion source in the ion chromatography technique: conformational information on polymer and biomolecular ions, Int. J. Mass Spectrom. Ion Process. 146–147 (1995) 349–364. doi:10.1016/0168-1176(95)04211-3.

[10] J.M. Koomen, B.T. Ruotolo, K.J. Gillig, J.A. McLean, D.H. Russell, M. Kang, K.R. Dunbar, K. Fuhrer, M. Gonin, J.A. Schultz, Oligonucleotide analysis with MALDI-ion-mobility-TOFMS, Anal. Bioanal. Chem. 373 (2002) 612–7. doi:10.1007/s00216-002-1363-2.

[11] H. Tong, N. Sze, B. Thomson, S. Nacson, J. Pawliszyn, Solid phase microextraction with matrix assisted laser desorption/ionization introduction to mass spectrometry and ion mobility spectrometry, Analyst. 127 (2002) 1207–10.

[12] Y. Wang, M. Walles, B. Thomson, S. Nacson, J. Pawliszyn, Solid-phase microextraction combined with surface-enhanced laser desorption/ionization introduction for ion mobility spectrometry and mass spectrometry using polypyrrole coatings, Rapid Commun. Mass Spectrom. 18 (2004) 157–162. doi:10.1002/rcm.1295.

[13] W.E. Steiner, B.H. Clowers, W.A. English, H.H. Hill, Atmospheric pressure matrix-assisted laser desorption/ionization with analysis by ion mobility time-of-flight mass spectrometry, Rapid Commun. Mass Spectrom. 18 (2004) 882–8. doi:10.1002/rcm.1419.

[14] A. Charvat, E. Lugovoj, M. Faubel, B. Abel, Analytical laser induced liquid beam desorption mass spectrometry of protonated amino acids and their non-covalently bound aggregates, Eur. Phys. J. D. 20 (2002) 573–582. doi:10.1140/epjd/e2002-00169-0.

[15] W. Kleinekofort, A. Pfenninger, T. Plomer, C. Griesinger, B. Brutschy, Observation of noncovalent complexes using laser-induced liquid beam ionization/desorption, Int. J. Mass Spectrom. Ion Process. 156 (1996) 195–202. doi:10.1016/S0168-1176(96)04507-7.

[16] W. Kleinekofort, J. Avdiev, B. Brutschy, A new method of laser desorption mass spectrometry for the study of biological macromolecules, Int. J. Mass Spectrom. Ion Process. 152 (1996) 135–142. doi:10.1016/0168-1176(95)04330-6.

[17] F. Sobott, A. Wattenberg, H.D. Barth, B. Brutschy, Ionic clathrates from aqueous solutions detected with laser induced liquid beam ionization/desorption mass spectrometry, Int. J. Mass Spectrom. 185 (1999) 271–279. doi:10.1016/S1387-3806(98)14158-1.

[18] A. Wattenberg, F. Sobott, H.D. Barth, B. Brutschy, Studying noncovalent protein complexes in aqueous solution with laser desorption mass spectrometry, Int. J. Mass Spectrom. 203 (2000) 49–57. doi:10.1016/S1387-3806(00)00261-X.

[19] S. Schulze, M. Pahl, F. Stolz, J. Appun, B. Abel, C. Schneider, D. Belder, Liquid Beam Desorption Mass Spectrometry for the Investigation of Continuous Flow Reactions in Microfluidic Chips, Anal. Chem. 89 (2017) 6175–6181. doi:10.1021/acs.analchem.7b01026.
[20] N. Morgner, H.-D. Barth, B. Brutschy, A New Way To Detect Noncovalently Bonded Complexes of Biomolecules from Liquid Micro-Droplets by Laser Mass Spectrometry, Aust. J. Chem. 59 (2006) 109. doi:10.1071/CH05285.
[21] R. Knochenmuss, Ion formation mechanisms in UV-MALDI, Analyst. 131 (2006) 966. doi:10.1039/b605646f.
[22] C. Menzel, K. Dreisewerd, S. Berkenkamp, F. Hillenkamp, The role of the laser pulse duration in infrared matrix-assisted laser desorption/ionization mass spectrometry, J. Am. Soc. Mass Spectrom. 13 (2002) 975–984. doi:10.1016/S1044-0305(02)00397-5.
[23] K. Dreisewerd, S. Berkenkamp, A. Leisner, A. Rohlfing, C. Menzel, Fundamentals of matrix-assisted laser desorption/ionization mass spectrometry with pulsed infrared lasers, Int. J. Mass Spectrom. 226 (2003) 189–209. doi:10.1016/S1387-3806(02)00977-6.
[24] W. Zhang, S. Niu, B.T. Chait, Exploring infrared wavelength matrix-assisted laser desorption/ionization of proteins with delayed-extraction time-of-flight mass spectrometry, J. Am. Soc. Mass Spectrom. 9 (1998) 879–884. doi:10.1016/S1044-0305(98)00060-9.
[25] S. Berkenkamp, C. Menzel, M. Karas, F. Hillenkamp, Performance of Infrared Matrix-assisted Laser Desorption/Ionization Mass Spectrometry with Lasers Emitting in the 3 µm Wavelength Range, Rapid Commun. Mass Spectrom. 11 (1997) 1399–1406. doi:10.1002/(SICI)1097-0231(19970830)11:13<1399::AID-RCM29>3.0.CO;2-B.
[26] C. Menzel, S. Berkenkamp, F. Hillenkamp, Infrared matrix-assisted laser desorption/ionization mass spectrometry with a transversely excited atmospheric pressure carbon dioxide laser at 10.6 µm wavelength with static and delayed ion extraction, Rapid Commun. Mass Spectrom. 13 (1999) 26–32. doi:10.1002/(SICI)1097-0231(19990115)13:1<26::AID-RCM443>3.0.CO;2-N.
[27] R. Cramer, W.J. Richter, E. Stimson, A.L. Burlingame, Analysis of Phospho-and Glycopolypeptides with Infrared Matrix-Assisted Laser Desorption and Ionization, Anal. Chem. 70 (1998) 4939–4944. doi:10.1021/ac9803939.
[28] C. Menzel, K. Dreisewerd, S. Berkenkamp, F. Hillenkamp, Mechanisms of energy deposition in infrared matrix-assisted laser desorption/ionization mass spectrometry, Int. J. Mass Spectrom. 207 (2001) 73–96. doi:10.1016/S1387-3806(01)00363-3.
[29] A.S. Woods, M. Ugarov, S.N. Jackson, T. Egan, H.Y.J. Wang, K.K. Murray, J.A. Schultz, IR-MALDI-LDI combined with ion mobility orthogonal time-of-flight mass spectrometry, J. Proteome Res. 5 (2006) 1484–1487. doi:10.1021/pr060055l.
[30] C.W. Rudy, Mid-IR Lasers: Power and pulse capability ramp up for mid-IR lasers, LaserFocusWorld. 50 (2014).
[31] The Scott Partnership, Mid-infrared lasers, Nat. Photonics. 4 (2010) 576–577. doi:10.1038/nphoton.2010.173.
[32] J.A. Crank, D.W. Armstrong, Towards a Second Generation of Ionic Liquid Matrices (ILMs) for MALDI-MS of Peptides, Proteins, and Carbohydrates, J. Am. Soc. Mass Spectrom. 20 (2009) 1790–1800. doi:10.1016/j.jasms.2009.05.020.
[33] P. Zöllner, G. Stübiger, E. Schmid, E. Pittenauer, G. Allmaier, MALDI mass spectrometry of biomolecules and synthetic polymers using alkali hexacyanoferrate (II) complexes and glycerol as matrix, Int. J. Mass Spectrom. Ion Process. 169–170 (1997) 99–109. doi:http://dx.doi.org/10.1016/S0168-1176(97)00230-9.
[34] Y. Fukuyama, Liquid Matrices in MALDI-MS, in: S. Handy (Ed.), Appl. Ion. Liq. Sci. Technol., InTech, 2011: pp. 361–364. doi:10.5772/24407.
[35] D.W. Armstrong, L.K. Zhang, L.F. He, M.L. Gross, Ionic liquids as matrixes for matrix-assisted laser desorption/ionization mass spectrometry, Anal. Chem. 75 (2001) 3679–3686.

doi:10.1021/ac010259f.
[36] T.-W.D. Chan, A.W. Colburn, P.J. Derrick, Matrix-assisted laser desorption/ionization using a liquid matrix: Formation of high-mass cluster ions from proteins, Org. Mass Spectrom. 27 (1992) 53–56. doi:10.1002/oms.1210270114.
[37] S. Zhao, K. V Somayajula, A.G. Sharkey, D.M. Hercules, F. Hillenkamp, M. Karas, A. Ingendoh, Novel Method for Matrix-Assisted Laser Mass Spectrometry of Proteins, Anal. Chem. 63 (1991) 450–453. doi:10.1021/ac00005a012.
[38] A. Overberg, M. Karas, F. Hillenkamp, R.J. Cotter, Matrix-assisted laser desorption of large biomolecules with a TEA-CO_2-laser, Rapid Commun. Mass Spectrom. 5 (1991) 128–131. doi:10.1002/rcm.1290050308.
[39] A. Overberg, M. Karas, U. Bahr, R. Kaufmann, F. Hillenkamp, Matrix-assisted infrared-laser (2.94 µm) desorption/ionization mass spectrometry of large biomolecules, Rapid Commun. Mass Spectrom. 4 (1990) 293–296. doi:10.1002/rcm.1290040808.
[40] D.S. Cornett, M.A. Duncan, I.J. Amster, Liquid Mixtures for Matrix-Assisted Laser Desorption, Anal. Chem. 65 (1993) 2608–2613.
[41] T. Williams, C. Fenselau, p-Nitroaniline/glycerol: a binary liquid matrix for MALDI analysis, Eur. J. Mass Spectrom. 4 (1998) 379. doi:10.1255/ejms.236.
[42] P. Zöllner, E.R. Schmid, G. Allmaier, K4[Fe(CN)6]/glycerol - A new liquid matrix system for matrix-assisted laser desorption/ionization mass spectrometry of hydrophobic compounds, Rapid Commun. Mass Spectrom. 10 (1996) 1278–1282. doi:10.1002/(SICI)1097-0231(19960731)10:10<1278::AID-RCM661>3.0.CO;2-L.
[43] J. Sunner, E. Dratz, Y.-C. Chen, Graphite surface-assisted laser desorption/ionization time-of-flight mass spectrometry of peptides and proteins from liquid solutions, Anal. Chem. 67 (1995) 4335–4342. doi:10.1021/ac00119a021.
[44] M.J. Dale, R. Knochenmuss, R. Zenobi, Graphite/liquid mixed matrices for laser desorption/ionization mass spectrometry, Anal. Chem. 68 (1996) 3321–3329. doi:10.1021/ac960558i.
[45] B.P. Nikolski, Handbuch des Chemikers, Band III, VEB Verlag Technik, Berlin, 1959.
[46] D.M. Wieliczka, S. Weng, M.R. Querry, Wedge shaped cell for highly absorbent liquids: infrared optical constants of water, Appl. Opt. 28 (1989) 1714. doi:10.1364/AO.28.001714.
[47] S. Berkenkamp, M. Karas, F. Hillenkamp, Ice as a matrix for IR-matrix-assisted laser desorption/ionization: mass spectra from a protein single crystal, Proc. Natl. Acad. Sci. U. S. A. 93 (1996) 7003–7. doi:10.1073/pnas.93.14.7003.
[48] M. Faubel, S. Schlemmer, J.P. Toennies, A molecular beam study of the evaporation of water from a liquid jet, Zeitschrift Für Phys. D Atoms, Mol. Clust. 10 (1988) 269–277. doi:10.1007/BF01384861.
[49] A. Wattenberg, F. Sobott, H.-D. Barth, B. Brutschy, Laser desorption mass spectrometry on liquid beams, Eur. J. Mass Spectrom. 5 (1999) 71. doi:10.1255/ejms.251.
[50] A. Charvat, B. Abel, How to make big molecules fly out of liquid water: applications, features and physics of laser assisted liquid phase dispersion mass spectrometry, Phys. Chem. Chem. Phys. 9 (2007) 3335–60. doi:10.1039/b615114k.
[51] J.M. Daniel, S. Ehala, S.D. Friess, R. Zenobi, On-line atmospheric pressure matrix-assisted laser desorption/ionization mass spectrometry, Analyst. 129 (2004) 574–578. doi:10.1039/b404178j.
[52] V. V. Laiko, M.A. Baldwin, A.L. Burlingame, Atmospheric pressure matrix-assisted laser desorption/ionization mass spectrometry, Anal. Chem. 72 (2000) 652–657. doi:10.1021/ac990998k.
[53] K. Turney, W.W. Harrison, Liquid supports for ultraviolet atmospheric pressure matrix-assisted laser desorption/ionization, Rapid Commun. Mass Spectrom. 18 (2004) 629–635. doi:10.1002/rcm.1379.
[54] V. V. Laiko, N.I. Taranenko, V.D. Berkout, M.A. Yakshin, C.R. Prasad, H.S. Lee, V.M.

Doroshenko, Desorption/ionization of biomolecules from aqueous solutions at atmospheric pressure using an infrared laser at 3 μm, J. Am. Soc. Mass Spectrom. 13 (2002) 354–361. doi:10.1016/S1044-0305(02)00341-0.

[55] C.E. Von Seggern, S.C. Moyer, R.J. Cotter, Liquid infrared atmospheric pressure matrix-assisted laser desorption/ionization ion trap mass spectrometry of sialylated carbohydrates, Anal. Chem. 75 (2003) 3212–3218. doi:10.1021/ac0262006.

[56] C.E. Von Seggern, P.E. Zarek, R.J. Cotter, Fragmentation of Sialylated Carbohydrates Using Infrared Atmospheric Pressure MALDI Ion Trap Mass Spectrometry from Cation-Doped Liquid Matrixes, Anal. Chem. 75 (2003) 6523–6530. doi:10.1021/ac0348367.

[57] J.M. Daniel, V. V. Laiko, V.M. Doroshenko, R. Zenobi, Interfacing liquid chromatography with atmospheric pressure MALDI-MS, Anal. Bioanal. Chem. 383 (2005) 895–902. doi:10.1007/s00216-005-0098-2.

[58] E. Rapp, A. Charvat, A. Beinsen, U. Plessmann, U. Reichl, A. Seidel-Morgenstern, H. Urlaub, B. Abel, Atmospheric pressure free liquid infrared MALDI mass spectrometry: Toward a combined ESI/MALDI-liquid chromatography interface, Anal. Chem. 81 (2009) 443–452.

[59] K. Hiraoka, S. Saito, J. Katsuragawa, I. Kudaka, A new liquid chromatography/mass spectrometry interface: Laser spray, Rapid Commun. Mass Spectrom. 12 (1998) 1170–1174. doi:10.1002/(SICI)1097-0231(19980915)12:17<1170::AID-RCM297>3.0.CO;2-O.

[60] I. Kudaka, T. Kojima, S. Saito, K. Hiraoka, A comparative study of laser spray and electrospray, Rapid Commun. Mass Spectrom. 14 (2000) 1558–1562. doi:10.1002/1097-0231(20000830)14:16<1558::AID-RCM64>3.0.CO;2-3.

[61] J. Shiea, M.-Z. Huang, H.-J. HSu, C.-Y. Lee, C.-H. Yuan, I. Beech, J. Sunner, Electrospray-assisted laser desorption/ionization mass spectrometry for direct ambient analysis of solids, Rapid Commun. Mass Spectrom. 19 (2005) 3701–3704. doi:10.1002/rcm.2243.

[62] P. Nemes, A. Vertes, Laser ablation electrospray ionization for atmospheric pressure, in vivo, and imaging mass spectrometry, Anal. Chem. 79 (2007) 8098–8106. doi:10.1021/ac071181r.

[63] Y.H. Rezenom, J. Dong, K.K. Murray, Infrared laser-assisted desorption electrospray ionization mass spectrometry, Analyst. 133 (2008) 226–232. doi:10.1039/b715146b.

[64] J.S. Sampson, A.M. Hawkridge, D.C. Muddiman, Generation and Detection of Multiply-Charged Peptides and Proteins by Matrix-Assisted Laser Desorption Electrospray Ionization (MALDESI) Fourier Transform Ion Cyclotron Resonance Mass Spectrometry, J. Am. Soc. Mass Spectrom. 17 (2006) 1712–1716. doi:10.1016/j.jasms.2006.08.003.

[65] J.S. Sampson, K.K. Murray, D.C. Muddiman, Intact and Top-Down Characterization of Biomolecules and Direct Analysis Using Infrared Matrix-Assisted Laser Desorption Electrospray Ionization Coupled to FT-ICR Mass Spectrometry, J. Am. Soc. Mass Spectrom. 20 (2009) 667–673. doi:10.1016/j.jasms.2008.12.003.

[66] J.J. Brady, E.J. Judge, R.J. Levis, Mass spectrometry of intact neutral macromolecules using intense non-resonant femtosecond laser vaporization with electrospray post-ionization, Rapid Commun. Mass Spectrom. 23 (2009) 3151–3157. doi:10.1002/rcm.4226.

[67] S.-C. Cheng, C. Shiea, Y.-L. Huang, C.-H. Wang, Y.-T. Cho, J. Shiea, Laser-based ambient mass spectrometry, Anal. Methods. 9 (2017) 4924–4935. doi:10.1039/C7AY00997F.

[68] L. V. Zhigilei, B.J. Garrison, Microscopic mechanisms of laser ablation of organic solids in the thermal and stress confinement irradiation regimes, J. Appl. Phys. 88 (2000) 1281–1298. doi:10.1063/1.373816.

[69] Z. Chen, A. Vertes, Early plume expansion in atmospheric pressure midinfrared laser ablation of water-rich targets, Phys. Rev. E - Stat. Nonlinear, Soft Matter Phys. 77 (2008) 036316. doi:10.1103/PhysRevE.77.036316.

[70] A. Charvat, B. Stasicki, B. Abel, Product screening of fast reactions in IR-laser-heated liquid water filaments in a vacuum by mass spectrometry, J. Phys. Chem. A. 110 (2006) 3297–3306. doi:10.1021/jp055165e.

[71] R. Knochenmuss, L. V. Zhigilei, Molecular dynamics model of ultraviolet matrix-assisted laser desorption/ionization including ionization processes, J. Phys. Chem. B. 109 (2005) 22947–22957. doi:10.1021/jp052945e.
[72] R. Knochenmuss, A quantitative model of ultraviolet matrix-assisted laser desorption/ionization, J. Mass Spectrom. 37 (2002) 867–877. doi:10.1002/jms.349.
[73] J. Blumm, A. Lindemann, Characterization of the thermophysical properties of molten polymers and liquids using the flash technique, High Temp. - High Press. 35–36 (2003) 627–632. doi:10.1068/htjr144.
[74] A. Miotello, R. Kelly, Laser-induced phase explosion: New physical problems when a condensed phase approaches the thermodynamic critical temperature, Appl. Phys. A Mater. Sci. Process. 69 (1999) 67–73. doi:10.1007/s003399900296.
[75] A. Vogel, V. Venugopalan, Mechanisms of pulsed laser ablation of biological tissues, Chem. Rev. 103 (2003) 577–644. doi:10.1021/cr010379n.
[76] A. Vogel, I. Apitz, V. Venugopalan, Phase transitions, material ejection, and plume dynamics in pulsed laser ablation of soft biological tissues, in: T. Kurz, Parlitz; Ulrich, U. Kaatze (Eds.), Oscil. Waves Interact., Univ.-Verl. Göttingen, Göttingen, 2007: pp. 217–258.
[77] Open University; University of Plymouth; University of Salford, PHYS 7.4: Specific heat, latent heat and entropy, PPLATO. (1996). http://www.met.reading.ac.uk/pplato2/h-flap/phys7_4.html (accessed March 29, 2018).
[78] A. Rohlfing, C. Menzel, L.M. Kukreja, F. Hillenkamp, K. Dreisewerd, Photoacoustic Analysis of Matrix-Assisted Laser Desorption/Ionization Processes with Pulsed Infrared Lasers, J. Phys. Chem. B. 107 (2003) 12275–12286. doi:10.1021/jp035554d.
[79] I. Apitz, A. Vogel, Material ejection in nanosecond Er:YAG laser ablation of water, liver, and skin, Appl. Phys. A Mater. Sci. Process. 81 (2005) 329–338. doi:10.1007/s00339-005-3213-5.
[80] A.L. Klein, W. Bouwhuis, C.W. Visser, H. Lhuissier, C. Sun, J.H. Snoeijer, E. Villermaux, D. Lohse, H. Gelderblom, Drop Shaping by Laser-Pulse Impact, Phys. Rev. Appl. 3 (2015) 1–6. doi:10.1103/PhysRevApplied.3.044018.
[81] B. Abel, A. Charvat, U. Diederichsen, M. Faubel, B. Girmann, J. Niemeyer, A. Zeeck, Applications, features, and mechanistic aspects of liquid water beam desorption mass spectrometry, Int. J. Mass Spectrom. 243 (2005) 177–188. doi:10.1016/j.ijms.2005.02.008.
[82] F. Wiederschein, Investigation of Laser-Induced-Liquid- Beam-Ion-Desorption (LILBID) with Molecular Dynamics Simulations, Georg-August-Universität zu Göttingen, 2009.
[83] A. Takamizawa, S. Kajimoto, J. Hobley, K. Hatanaka, K. Ohta, H. Fukumura, Explosive boiling of water after pulsed IR laser heating, Phys. Chem. Chem. Phys. 5 (2003) 888–895. doi:10.1039/b210609d.
[84] F. Wiederschein, E. Vöhringer-Martinez, A. Beinsen, F. Postberg, J. Schmidt, R. Srama, F. Stolz, H. Grubmüller, B. Abel, Charge separation and isolation in strong water droplet impacts, Phys. Chem. Chem. Phys. 17 (2015) 6858–64. doi:10.1039/c4cp05618c.
[85] K. Komatsu, T. Nirasawa, M. Hoshino-Nagasaka, J.Y. Kohno, Mechanism of Protein Molecule Isolation by IR Laser Ablation of Droplet Beam, J. Phys. Chem. A. 120 (2016) 1495–1500. doi:10.1021/acs.jpca.5b10873.
[86] P. Kebarle, L. Tang, From ions in solution to ions in the gas phase - the mechanism of electrospray mass spectrometry, Anal. Chem. 65 (1993) 972A–986A. doi:10.1021/ac00070a001.
[87] L. Konermann, E. Ahadi, A.D. Rodriguez, S. Vahidi, Unraveling the mechanism of electrospray ionization, Anal. Chem. 85 (2013) 2–9. doi:10.1021/ac302789c.
[88] J. V. Iribarne, B.A. Thomson, On the evaporation of small ions from charged droplets, J. Chem. Phys. 64 (1976) 2287. doi:10.1063/1.432536.
[89] B.A. Thomson, J. V. Iribarne, Field induced ion evaporation from liquid surfaces at atmospheric pressure, J. Chem. Phys. 71 (1979) 4451–4463. doi:10.1063/1.438198.

[90] P. Kebarle, U.H. Verkerk, Electrospray: From ions in solution to ions in the gas phase, what we know now, Mass Spectrom. Rev. 28 (2009) 898–917. doi:10.1002/mas.20247.
[91] L. Konermann, A.D. Rodriguez, J. Liu, On the Formation of Highly Charged Gaseous Ions from Unfolded Proteins by Electrospray Ionization, Anal. Chem. 84 (2012) 6798–6804. doi:10.1021/ac301298g.
[92] E. Ahadi, L. Konermann, Modeling the Behavior of Coarse-Grained Polymer Chains in Charged Water Droplets: Implications for the Mechanism of Electrospray Ionization, J. Phys. Chem. B. 116 (2012) 104–112. doi:10.1021/jp209344z.
[93] A. Charvat, A. Bögehold, B. Abel, Time-resolved micro liquid desorption mass spectrometry: Mechanism, features, and kinetic applications, Aust. J. Chem. 59 (2006) 81–103.
[94] E. Ahadi, L. Konermann, Ejection of solvated ions from electrosprayed methanol/water nanodroplets studied by molecular dynamics simulations, J. Am. Chem. Soc. 133 (2011) 9354–9363. doi:10.1021/ja111492s.
[95] Michael P. Allen, Introduction to Molecular Dynamics, in: N. Attig, K. Binder, H. Grubmüller, K. Kremer (Eds.), Comput. Soft Matter From Synth. Polym. to Proteins - Lect. Notes, NIC-Directors, Jülich, 2004: pp. 1–22.
[96] F. Noé, S. Röblitz, B. Schmidt, C. Schütte, M. Weber, Simulation von Biomolekülen, Vor. Skript. (2013).
[97] J.E. Jones, On the Determination of Molecular Fields. II. From the Equation of State of a Gas, Proc. R. Soc. A Math. Phys. Eng. Sci. 106 (1924) 463–477. doi:10.1098/rspa.1924.0082.
[98] L. Verlet, Computer "Experiments" on Classical Fluids. I. Thermodynamical Properties of Lennard-Jones Molecules, Phys. Rev. 159 (1967) 98–103. doi:10.1103/PhysRev.159.98.
[99] J.D. Gale, A.L. Rohl, The General Utility Lattice Program (GULP), Mol. Simul. 29 (2003) 291–341. doi:10.1080/0892702031000104887.
[100] J. Niskanen, H. Henschel, Molecular dynamics simulations, Lecture notes, (2013).
[101] T. Schlick, Force Fields, in: Mol. Model. Simul. An Interdiscip. Guid., Second Edi, Springer New York, New York, NY, 2010: pp. 265–298. doi:10.1007/978-1-4419-6351-2_9.
[102] E. Lindahl, GROMACS 5.1.1 Reference Manual, (n.d.).
[103] J. Richardson, D. Richardson, Principles and Patterns of Protein Conformation, in: Fasman G.D. (Ed.), Predict. Protein Struct. Princ. Protein Conform., Springer US, Boston, MA, 1989: pp. 1–98. doi:10.1007/978-1-4613-1571-1_1.
[104] J. Vymětal, J. Vondrášek, Critical assessment of current force fields. Short peptide test case, J. Chem. Theory Comput. 9 (2013) 441–451. doi:10.1021/ct300794a.
[105] G. Collier, N.A. Vellore, J.A. Yancey, S.J. Stuart, R.A. Latour, Comparison between empirical protein force fields for the simulation of the adsorption behavior of structured LK peptides on functionalized surfaces, Biointerphases. 7 (2012) 1–19. doi:10.1007/s13758-012-0024-z.
[106] H.E. Revercomb, E.A. Mason, Theory of Plasma Chromatography/Gaseous Electrophoresis-A Review, Anal. Chem. 47 (1975) 970–983. doi:10.1021/ac60357a043.
[107] C.S. Creaser, J.R. Griffiths, C.J. Bramwell, S. Noreen, C. a. Hill, C.L.P. Thomas, A. Hill, C.L.P. Thomas, Ion mobility spectrometry: a review. Part 1. Structural analysis by mobility measurement, Analyst. 129 (2004) 984. doi:10.1039/b404531a.
[108] E.A. Mason, E.W. McDaniel, Transport Properties of Ions in Gases, John Wiley & Sons, Inc, USA, 1988. doi:10.1002/3527602852.
[109] G.E. Spangler, C.I. Collins, Peak Shape Analysis and Plate Theory for Plasma Chromatography, Anal. Chem. 47 (1975) 403–407. doi:10.1021/ac60353a013.
[110] G.E. Spangler, Expanded theory for the resolving power of a linear ion mobility spectrometry, Int. J. Mass Spectrom. 220 (2002) 399–418. doi:10.1016/S1387-3806(02)00841-2.
[111] G.E. Spangler, Space Charge Effects in Ion Mobility Spectrometry, Anal. Chem. 64 (1992)

1312.
[112] W.F. Siems, C. Wu, E.E. Tarver, H.H. Hill, P.R. Larsen, D.G. McMinn, Measuring the Resolving Power of Ion Mobility Spectrometers, Anal. Chem. 66 (1994) 4195–4201. doi:10.1021/ac00095a014.
[113] B.C. Hauck, W.F. Siems, C.S. Harden, V.M. McHugh, H.H. Hill, E/N effects on K0 values revealed by high precision measurements under low field conditions, Rev. Sci. Instrum. 87 (2016) 075104. doi:10.1063/1.4955208.
[114] B.C. Hauck, W.F. Siems, C.S. Harden, V.M. McHugh, H.H. Hill, Determination of E / N Influence on K0 Values within the Low Field Region of Ion Mobility Spectrometry, J. Phys. Chem. A. 121 (2017) 2274–2281. doi:10.1021/acs.jpca.6b12331.
[115] V. Gabelica, E. Marklund, Fundamentals of ion mobility spectrometry, Curr. Opin. Chem. Biol. 42 (2018) 51–59. doi:10.1016/j.cbpa.2017.10.022.
[116] E. Mack, Average cross-sectional areas of molecules by gaseous diffusion methods, J. Am. Chem. Soc. 47 (1925) 2468–2482. doi:10.1021/ja01687a007.
[117] G. Von Helden, M.T. Hsu, N. Gotts, M.T. Bowers, Carbon cluster cations with up to 84 atoms: Structures, formation mechanism, and reactivity, J. Phys. Chem. 97 (1993) 8182–8192. doi:10.1021/j100133a011.
[118] A.A. Shvartsburg, M.F. Jarrold, An exact hard-spheres scattering model for the mobilities of polyatomic ions, Chem. Phys. Lett. 261 (1996) 86–91. doi:10.1016/0009-2614(96)00941-4.
[119] A.A. Shvartsburg, S. V. Mashkevich, K.W. Michael Siu, Incorporation of thermal rotation of drifting ions into mobility calculations: Drastic effect for heavier buffer gases, J. Phys. Chem. A. 104 (2000) 9448–9453. doi:10.1021/jp001753a.
[120] C. Bleiholder, T. Wyttenbach, M.T. Bowers, A novel projection approximation algorithm for the fast and accurate computation of molecular collision cross sections (I). Method, Int. J. Mass Spectrom. 308 (2011) 1–10. doi:10.1016/j.ijms.2011.06.014.
[121] C. Bleiholder, S. Contreras, T.D. Do, M.T. Bowers, A novel projection approximation algorithm for the fast and accurate computation of molecular collision cross sections (II). Model parameterization and definition of empirical shape factors for proteins, Int. J. Mass Spectrom. 345–347 (2013) 89–96. doi:10.1016/j.ijms.2012.08.027.
[122] S.E. Anderson, C. Bleiholder, E.R. Brocker, P.J. Stang, M.T. Bowers, A novel projection approximation algorithm for the fast and accurate computation of molecular collision cross sections (III): Application to supramolecular coordination-driven assemblies with complex shapes, Int. J. Mass Spectrom. 330–332 (2012) 78–84. doi:10.1016/J.IJMS.2012.08.024.
[123] C. Bleiholder, S. Contreras, M.T. Bowers, A novel projection approximation algorithm for the fast and accurate computation of molecular collision cross sections (IV). Application to polypeptides, Int. J. Mass Spectrom. 354–355 (2013) 275–280. doi:10.1016/J.IJMS.2013.06.011.
[124] Y. Alexeev, D.G. Fedorov, A.A. Shvartsburg, Effective ion mobility calculations for macromolecules by scattering on electron clouds, J. Phys. Chem. A. 118 (2014) 6763–6772. doi:10.1021/jp505012c.
[125] M.F. Mesleh, J.M. Hunter, A.A. Shvartsburg, G.C. Schatz, M.F. Jarrold, Structural Information from Ion Mobility Measurements: Effects of the Long-Range Potential, J. Phys. Chem. 100 (1996) 16082–16086. doi:10.1021/jp961623v.
[126] H. Kim, H.I. Kim, P. V. Johnson, L.W. Beegle, J.L. Beauchamp, W.A. Goddard, I. Kanik, Experimental and theoretical investigation into the correlation between mass and ion mobility for choline and other ammonium cations in N_2, Anal. Chem. 80 (2008) 1928–1936. doi:10.1021/ac701888e.
[127] I. Campuzano, M.F. Bush, C. V. Robinson, C. Beaumont, K. Richardson, H. Kim, H.I. Kim, Structural characterization of drug-like compounds by ion mobility mass spectrometry: Comparison of theoretical and experimentally derived nitrogen collision cross sections,

Anal. Chem. 84 (2012) 1026–1033. doi:10.1021/ac202625t.
[128] A. Shvartsburg, Differential Ion Mobility Spectrometry, CRC Press, 2008. doi:10.1201/9781420051070.
[129] J. Lozeille, E. Winata, P. Soldán, E.P.F. Lee, L.A. Viehland, T.G. Wright, Spectroscopy of Li+·Rg and Li+–Rg transport coefficients (Rg = He–Rn), Phys. Chem. Chem. Phys. 4 (2002) 3601–3610. doi:10.1039/b111675d.
[130] H.L. Hickling, L.A. Viehland, D.T. Shepherd, P. Soldán, T.G. Wright, Spectroscopy of M+·Rg and transport coefficients of M+ in Rg (M = Rb–Fr; Rg = He–Rn), Phys. Chem. Chem. Phys. 6 (2004) 4233–4239. doi:10.1039/b405221h.
[131] E. Qing, L.A. Viehland, E.P.F. Lee, T.G. Wright, Interaction potentials and spectroscopy of and and transport coefficients for and in Rg Interaction potentials and spectroscopy of Hg+ · Rg and Cd+ · Rg and transport coefficients for Hg + and Cd + in Rg (Rg=He-Rn), J. Chem. Phys. 124 (2006). doi:10.1063/1.2148955.
[132] M. Zühlke, D. Riebe, T. Beitz, H.-G. Löhmannsröben, K. Zenichowski, M. Diener, M.W. Linscheid, An electrospray ionization-ion mobility spectrometer as detector for high-performance liquid chromatography., Eur. J. Mass Spectrom. 21 (2015) 391–402. doi:10.1255/ejms.1367.
[133] P.C. Jocelyn, Chemical Reduction of Disulfides, Methods Enzymol. 143 (1987) 246–256. doi:10.1016/0076-6879(87)43048-6.
[134] M. Zühlke, ESI- und IR-FL-MALDI- Ionenmobilitätsspektrometrie von Biomolekülen, Universität Potsdam, 2012.
[135] A. Erler, Mobilitäten aromatischer Ionen in verschiedenen Driftgasen und Ionisationschemie halogenierter und nitrierter Aromaten in der Ionenmobilitäts- und Massenspektrometrie, Universität Potsdam, 2013.
[136] E.A. Cino, W.Y. Choy, M. Karttunen, Comparison of secondary structure formation using 10 different force fields in microsecond molecular dynamics simulations, J. Chem. Theory Comput. 8 (2012) 2725–2740. doi:10.1021/ct300323g.
[137] K. Lindorff-Larsen, P. Maragakis, S. Piana, M.P. Eastwood, R.O. Dror, D.E. Shaw, Systematic validation of protein force fields against experimental data, PLoS One. 7 (2012) e32131. doi:10.1371/journal.pone.0032131.
[138] W. Chen, C. Shi, A.D. Mackerell, J. Shen, Conformational dynamics of two natively unfolded fragment peptides: Comparison of the AMBER and CHARMM Force Fields, J. Phys. Chem. B. 119 (2015) 7902–7910. doi:10.1021/acs.jpcb.5b02290.
[139] F. Martín-García, E. Papaleo, P. Gomez-Puertas, W. Boomsma, K. Lindorff-Larsen, Comparing molecular dynamics force fields in the essential subspace, PLoS One. 10 (2015) e0121114. doi:10.1371/journal.pone.0121114.
[140] P.E.M. Lopes, O. Guvench, A.D. MacKerell, Current status of protein force fields for molecular dynamics simulations, in: Mol. Model. Proteins Second Ed., Humana Press, New York, NY, 2014: pp. 47–71. doi:10.1007/978-1-4939-1465-4_3.
[141] O. Guvench, A.D. MacKerell, Comparison of protein force fields for molecular dynamics simulations, in: A. Kukol (Ed.), Mol. Model. Proteins. Methods Mol. Biol., Humana Press, 2008: pp. 63–88. doi:10.1007/978-1-59745-177-2_4.
[142] K. Lindorff-Larsen, S. Piana, K. Palmo, P. Maragakis, J.L. Klepeis, R.O. Dror, D.E. Shaw, Improved side-chain torsion potentials for the Amber ff99SB protein force field, Proteins Struct. Funct. Bioinforma. 78 (2010) 1950–1958. doi:10.1002/prot.22711.
[143] C.I. Bayly, P. Cieplak, W.D. Cornell, P.A. Kollman, A well-behaved electrostatic potential based method using charge restraints for deriving atomic charges: The RESP model, J. Phys. Chem. 97 (1993) 10269–10280. doi:10.1021/j100142a004.
[144] M.W. Schmidt, K.K. Baldridge, J.A. Boatz, S.T. Elbert, M.S. Gordon, J.H. Jensen, S. Koseki, N. Matsunaga, K.A. Nguyen, S. Su, T.L. Windus, M. Dupuis, J.A. Montgomery, General atomic and molecular electronic structure system, J. Comput. Chem. 14 (1993) 1347–1363.

doi:10.1002/jcc.540141112.
[145] A.A. Granovsky, Firefly version 8, (n.d.).
[146] F.-Y. Dupradeau, A. Pigache, T. Zaffran, C. Savineau, R. Lelong, N. Grivel, D. Lelong, W. Rosanski, P. Cieplak, The R.E.D. tools: advances in RESP and ESP charge derivation and force field library building, Phys. Chem. Chem. Phys. 12 (2010) 7821. doi:10.1039/c0cp00111b.
[147] F. Wang, J.P. Becker, P. Cieplak, F.-Y. Dupradeau, R.E.D. Python: Object oriented programming for Amber force fields, (2013).
[148] E. Vanquelef, S. Simon, G. Marquant, E. Garcia, G. Klimerak, J.C. Delepine, P. Cieplak, F.Y. Dupradeau, R.E.D. Server: A web service for deriving RESP and ESP charges and building force field libraries for new molecules and molecular fragments, Nucleic Acids Res. 39 (2011). doi:10.1093/nar/gkr288.
[149] J. Wang, W. Wang, P.A. Kollman, D.A. Case, Automatic atom type and bond type perception in molecular mechanical calculations, J. Mol. Graph. Model. 25 (2006) 247–260. doi:10.1016/j.jmgm.2005.12.005.
[150] J. Wang, R.M. Wolf, J.W. Caldwell, P.A. Kollman, D.A. Case, Development and testing of a general Amber force field, J. Comput. Chem. 25 (2004) 1157–1174. doi:10.1002/jcc.20035.
[151] E.F. Pettersen, T.D. Goddard, C.C. Huang, G.S. Couch, D.M. Greenblatt, E.C. Meng, T.E. Ferrin, UCSF Chimera - A visualization system for exploratory research and analysis, J. Comput. Chem. 25 (2004) 1605–1612. doi:10.1002/jcc.20084.
[152] A.G. Harrison, The gas-phase basicities and proton affinities of amino acids and peptides, Mass Spectrom. Rev. 16 (1997) 201–217. doi:10.1002/(SICI)1098-2787(1997)16:4<201::AID-MAS3>3.0.CO;2-L.
[153] M.J. Abraham, T. Murtola, R. Schulz, S. P??all, J.C. Smith, B. Hess, E. Lindah, Gromacs: High performance molecular simulations through multi-level parallelism from laptops to supercomputers, SoftwareX. 1–2 (2015) 19–25. doi:10.1016/j.softx.2015.06.001.
[154] H.J.C. Berendsen, D. van der Spoel, R. van Drunen, GROMACS: A message-passing parallel molecular dynamics implementation, Comput. Phys. Commun. 91 (1995) 43–56. doi:10.1016/0010-4655(95)00042-E.
[155] D. Van Der Spoel, E. Lindahl, B. Hess, G. Groenhof, A.E. Mark, H.J.C. Berendsen, GROMACS: Fast, flexible, and free, J. Comput. Chem. 26 (2005) 1701–1718. doi:10.1002/jcc.20291.
[156] D. Frenkel, B. Smit, Understanding Molecular Simulation, Second Edi, Academic Press, 2002. doi:10.1016/B978-012267351-1/50006-7.
[157] J.E. Jensen, W. a. Tuttle, R.B. Stewart, H. Brechna, A.G. Prodell, Properties of Nitrogen, in: Sel. Cryog. Data Noteb., Brookhaven, Associated Universities, Inc., 1980.
[158] G. Bussi, D. Donadio, M. Parrinello, Canonical sampling through velocity rescaling, J. Chem. Phys. 126 (2007) 014101. doi:10.1063/1.2408420.
[159] S. Röblitz, M. Weber, Fuzzy spectral clustering by PCCA+: application to Markov state models and data classification, Adv. Data Anal. Classif. 7 (2013) 147–179. doi:10.1007/s11634-013-0134-6.
[160] P. Deuflhard, M. Weber, Robust Perron cluster analysis in conformation dynamics, Linear Algebra Appl. 398 (2005) 161–184. doi:10.1016/j.laa.2004.10.026.
[161] M.Weber, T.Galliat, Characterization of Transition States in Conformational Dynamics using Fuzzy Sets. ZIB-Report 02–12, 2002.
[162] M. Weber, R. Becker, V. Durmaz, R. Köppen, Classical hybrid Monte-Carlo simulation of the interconversion of hexabromocyclododecane stereoisomers, Mol. Simul. 34 (2008) 727–736.
[163] N.M. O'Boyle, M. Banck, C.A. James, C. Morley, T. Vandermeersch, G.R. Hutchison, Open Babel: An Open chemical toolbox, J. Cheminform. 3 (2011). doi:10.1186/1758-2946-3-33.
[164] A. Lehmann, Elektrosprayionisation-Ionenmobilitätsspektrometrie zur Peptidanalytik, Universität Potsdam, 2016.
[165] S.J. Valentine, a. E. Counterman, C.S. Hoaglund-Hyzer, D.E. Clemmer, Intrinsic amino acid

size parameters from a series of 113 lysine-terminated tryptic digest peptide ions, J. Phys. Chem. B. 103 (1999) 1203–1207. doi:10.1021/jp983906o.
[166] S.J. Valentine, A.E. Counterman, D.E. Clemmer, A database of 660 peptide ion cross sections: use of intrinsic size parameters for bona fide predictions of cross sections, J. Am. Soc. Mass Spectrom. 10 (1999) 1188–1211. doi:10.1016/S1044-0305(99)00079-3.
[167] J.A. Taraszka, A.E. Counterman, D.E. Clemmer, Gas-phase separations of complex tryptic peptide mixtures, Fresenius. J. Anal. Chem. 369 (2001) 234–245. doi:10.1007/s002160000669.
[168] M.F. Bush, I.D.G. Campuzano, C. V. Robinson, Ion mobility mass spectrometry of peptide ions: Effects of drift gas and calibration strategies, Anal. Chem. 84 (2012) 7124–7130. doi:10.1021/ac3014498.
[169] J.M. Dilger, S.J. Valentine, M.S. Glover, M.A. Ewing, D.E. Clemmer, A database of alkali metal-containing peptide cross sections: Influence of metals on size parameters for specific amino acids, Int. J. Mass Spectrom. 330–332 (2012) 35–45. doi:10.1016/j.ijms.2012.05.001.
[170] S.K. Fegan, M. Thachuk, A charge moving algorithm for molecular dynamics simulations of gas-phase proteins, J. Chem. Theory Comput. 9 (2013) 2531–2539. doi:10.1021/ct300906a.
[171] J.M. Dilger, S.J. Valentine, M.S. Glover, D.E. Clemmer, A database of alkaline-earth-coordinated peptide cross sections: Insight into general aspects of structure, J. Am. Soc. Mass Spectrom. 24 (2013) 768–779. doi:10.1007/s13361-013-0579-z.
[172] Z. Li, J.M. Dilger, V. Pejaver, D. Smiley, R.J. Arnold, S.D. Mooney, S. Mukhopadhyay, P. Radivojac, D.E. Clemmer, Intrinsic Size Parameters for Palmitoylated and Carboxyamidomethylated Peptides, Int. J. Mass Spectrom. 368 (2014) 6–14.
[173] A. Michalik-Onichimowska, T. Beitz, U. Panne, H.G. Löhmannsröben, J. Riedel, Microsecond mid-infrared laser pulses for atmospheric pressure laser ablation/ionization of liquid samples, Sensors Actuators, B Chem. 238 (2017) 298–305. doi:10.1016/j.snb.2016.06.155.
[174] P. Nemes, A. Vertes, Laser Ablation Electrospray Ionization Mass Spectrometry: Mechanisms, Configurations and Imaging Applications, in: Ambient Ioniz. Mass Spectrom., The Royal Society of Chemistry, 2015: pp. 348–371. doi:10.1039/9781782628026-00348.
[175] M. Tabrizchi, T. Khayamian, N. Taj, Design and optimization of a corona discharge ionization source for ion mobility spectrometry, Rev. Sci. Instrum. 71 (2000) 2321. doi:10.1063/1.1150618.
[176] R. Fernández-Maestre, C.S. Harden, R.G. Ewing, C.L. Crawford, H.H. Hill, Chemical standards in ion mobility spectrometry, Analyst. 135 (2010) 1433. doi:10.1039/b915202d.
[177] A. Tolmachev, B. Clowers, Coulombic effects in ion mobility spectrometry, Anal. Chem. 81 (2009) 4778–4787. doi:10.1021/ac802652f.(20).
[178] W. Wißdorf, D. Müller, Y. Brachthäuser, M. Langner, V. Derpmann, S. Klopotowski, C. Polaczek, H. Kersten, K. Brockmann, T. Benter, Gas Flow Dynamics in Inlet Capillaries: Evidence for non Laminar Conditions, J. Am. Soc. Mass Spectrom. 27 (2016) 1550–1563. doi:10.1007/s13361-016-1415-z.
[179] D.J. Santeler, Exit loss in viscous tube flow, J. Vac. Sci. Technol. A Vacuum, Surfaces, Film. 4 (1986) 348. doi:10.1116/1.573925.
[180] P. Holt Sackett, Effect of structure of phenothiazine cation radicals on reactions with aqueous nucleophiles, Ohio State University, 1979.
[181] O. Kohlbacher, K. Reinert, C. Gröpl, E. Lange, N. Pfeifer, O. Schulz-Trieglaff, M. Sturm, TOPP - The OpenMS proteomics pipeline, in: Bioinformatics, Oxford University Press, 2007: pp. 191–197. doi:10.1093/bioinformatics/btl299.
[182] M. Sturm, A. Bertsch, C. Gröpl, A. Hildebrandt, R. Hussong, E. Lange, N. Pfeifer, O. Schulz-Trieglaff, A. Zerck, K. Reinert, O. Kohlbacher, OpenMS - An open-source software framework for mass spectrometry, Bioinformatics. 9 (2008) 1–11. doi:10.1186/1471-2105-9-163.

[183] F. Brugé, M. Bernasconi, M. Parrinello, Density-functional study of hydration of ammonium in water clusters, J. Chem. Phys. 110 (1999) 4734–4736. doi:10.1063/1.478360.
[184] G.F. Verbeck, B.T. Ruotolo, H.A. Sawyer, K.J. Gillig, D.H. Russell, A fundamental introduction to ion mobility mass spectrometry applied to the analysis of biomolecules, J. Biomol. Tech. 13 (2002) 56–61.
[185] J.A. McLean, The Mass-Mobility Correlation Redux: The Conformational Landscape of Anhydrous Biomolecules, J. Am. Soc. Mass Spectrom. 20 (2009) 1775–1781. doi:10.1016/j.jasms.2009.06.016.
[186] L.S. Fenn, M. Kliman, A. Mahsut, S.R. Zhao, J.A. McLean, Characterizing ion mobility-mass spectrometry conformation space for the analysis of complex biological samples, Anal. Bioanal. Chem. 394 (2009) 235–244. doi:10.1007/s00216-009-2666-3.
[187] S.I. Merenbloom, B.C. Bohrer, S.L. Koeniger, D.E. Clemmer, Assessing the peak capacity of IMS-IMS separations of tryptic peptide ions in He at 300 K, Anal. Chem. 79 (2007) 515–22. doi:10.1021/ac061567m.
[188] T. Wyttenbach, G. Von Helden, M.T. Bowers, Gas-phase conformation of biological molecules: Bradykinin, J. Am. Chem. Soc. 118 (1996) 8355–8364. doi:10.1021/ja9535928.
[189] C.F. Rodriquez, G. Orlova, Y. Guo, X. Li, C.K. Siu, A.C. Hopkinson, K.W.M. Siu, Gaseous bradykinin and its singly, doubly, and triply protonated forms: A first-principles study, J. Phys. Chem. B. 110 (2006) 7528–7537. doi:10.1021/jp046015r.

Appendix

The following graph shows the required files for the execution of the cascade of scripts used in the molecular dynamics collision cross-section determination method. Folders are written in bold typeface inside boxes with straight edges while files are in rounded boxes. The greyed folder is created by a script in the sequence, after which the required files in figure A1 must for the time being be introduced manually.

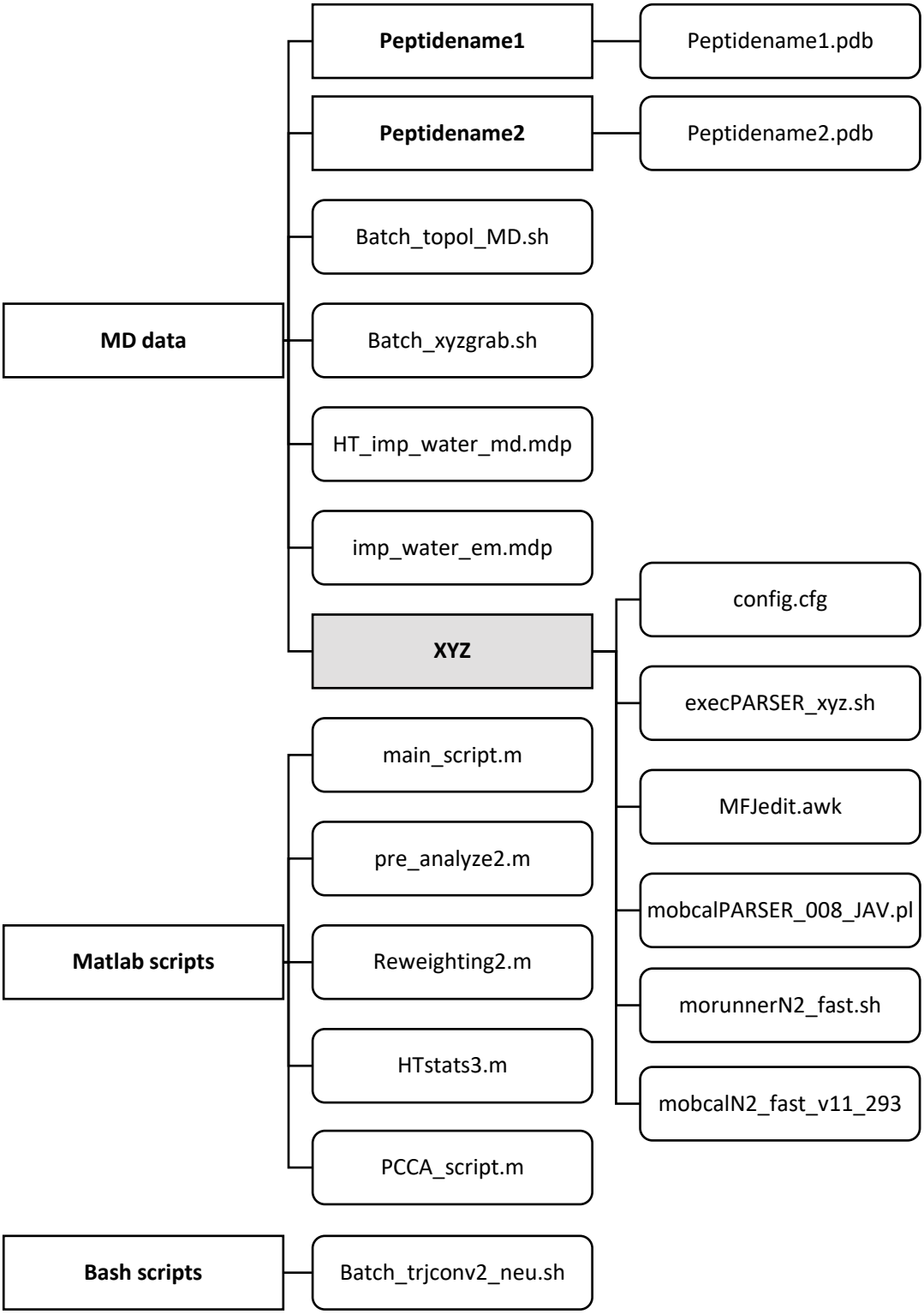

Figure A1: File architecture for running the MD-based collision cross-section estimation method

The series of scripts developed for the MD-based collision cross-section approach and their execution sequence are given in figure A2. The broken hierarchy indicates the steps that still need automation through a higher level script. The script for clustering through PCCA+ and its subroutines were obtained from our group at the Zuse Institute Berlin. The mobcal parser available at sourceforge.net was developed by John Patrick Boyd.

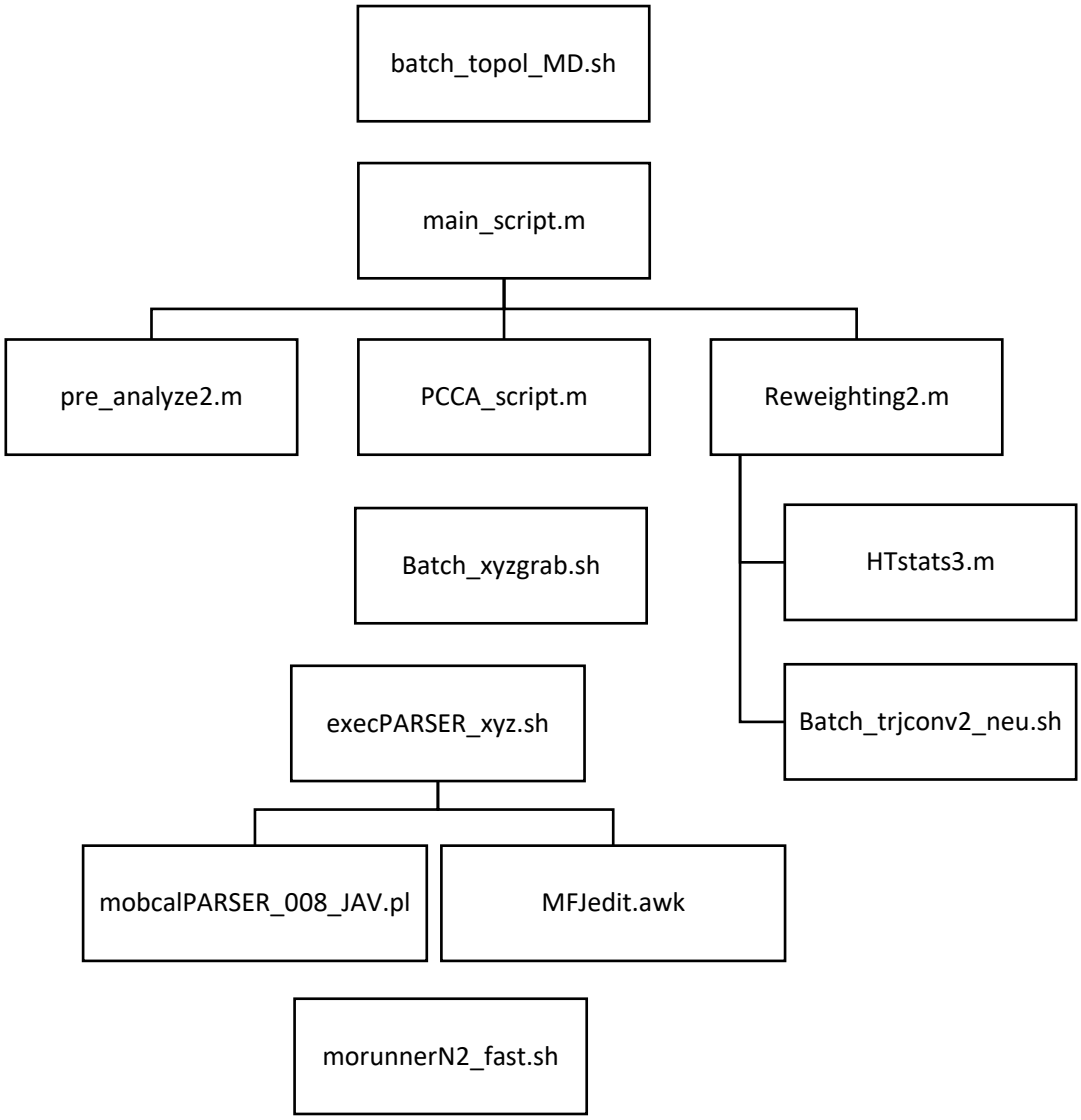

Figure A2: Script sequence with subordinate subscripts

Bash script batch_topol_MD.sh

```
#!/bin/bash

#List all the peptide subfolders there are and save them to a variable
folderlist=$(ls -d */)

#Do in parallel, for all the folders in the list
for folder in $folderlist
do
    #Enter folder. Define peptide name from folder name
    (cd $folder
    peptidename=$(echo $folder | sed s'/.$//')

    #get topology using the customized amber99sb-ildn forcefield and center structure
    yes 6 | gmx pdb2gmx -f ${peptidename}.pdb -o ${peptidename}.gro -water none >>
    log.txt
    gmx editconf -f ${peptidename}.gro -o ${peptidename}_cent.gro -c -d 1.0 -bt cubic >>
    log.txt

    #assemble run files for energy minimization and run energy minimization
    #CAREFUL!! --> it is assumed the topology filename is the default topol.top
    gmx grompp -f ../imp_water_em.mdp -c ${peptidename}_cent.gro -p topol.top -o
    ${peptidename}_em.tpr >> log.txt
    gmx mdrun -nt 1 -v -deffnm ${peptidename}_em >> log.txt

    #assemble run files for MD and run MD
    gmx grompp -f ../HT_imp_water_md.mdp -c ${peptidename}_em.gro -p topol.top -o
    HT_${peptidename}_md.tpr
    gmx mdrun -nt 1 -v -deffnm HT_${peptidename}_md

    wait

    #Get only the isolated coordinates
    yes 0 | gmx trjconv -f HT_${peptidename}_md.trr -s HT_${peptidename}_md.tpr -o
    xyz.gro
    line2=$(sed -n '2p' < xyz.gro)
    sed -n '/Generated/{s/.*//;x;d;};x;p;${x;p;}' xyz.gro | sed '/^$/d' | sed "/^$line2/d" | sed -
    r 's/.{22}//' | sed '$d' > xyz${peptidename}_HT.txt

    #Get potential energy
    yes 11 0 | gmx energy -f HT_${peptidename}_md.edr -o PotEner.xvg
    sed '/^@/d' PotEner.xvg | sed '/^#/d' > PotEnerHT_${peptidename}.txt

    #Copy files to peptides
    mkdir -p /home/numerik/bzfvilla/Dokumente/Conformations/Peptides/${peptidename}
    wait
    cp xyz${peptidename}_HT.txt PotEnerHT_${peptidename}.txt
    /home/numerik/bzfvilla/Dokumente/Conformations/Peptides/${peptidename}

    cd ..)&
done
```

imp_water_em.mdp

```
define                  =                   ; -DFLEXIBLE -DPOSRES
constraints             = none
integrator              = steep             ; cg
dt                      = 0.001             ; ps
nsteps                  = 30000

cutoff-scheme           = group
vdwtype                 = cut-off
coulombtype             = cut-off

pbc                     = no
nstlist                 = 0
ns_type                 = simple
rlist                   = 0                 ; this means all-vs-all (no cut-off), which
                                            gets expensive for bigger systems
rcoulomb                = 0
rvdw                    = 0

comm-mode               = angular
comm-grps               = system

; Energy minimizing stuff
emtol                   = 30.0
emstep                  = 0.01

; Implicit solvent
implicit-solvent        = GBSA
gb-algorithm            = Still             ; HCT ; OBC
nstgbradii              = 1
rgbradii                = 0                 ; [nm] Cut-off for the calculation of the Born
                                            radii. Currently must be equal to rlist
gb-epsilon_solvent      = 1.0003623353      ; Dielectric constant for nitrogen at 170 °C
sa-algorithm            = Ace-approximation
sa-surface_tension      = 2.05016           ; with still; -1  ; 2.25936; with HCT/OBC
```

HT_imp_water_md.mdp

```
define                  = -DPOSRES
constraints             = none
integrator              = md
dt                      = 0.001             ; ps
nsteps                  = 10000000          ; 100000 ps = 100 ns
nstcomm                 = 10
nstcalcenergy           = 10
nstxout                 = 5000              ; frequency to write coordinates to output
                                            trajectory
nstvout                 = 0                 ; frequency to write velocities to output
                                            trajectory; the last velocities are always
                                            written
nstfout                 = 0                 ; frequency to write forces to output
                                            trajectory
```

```
nstlog                  =  5000         ; frequency to write energies to log file
nstenergy               =  5000         ; frequency to write energies to edr file

cutoff-scheme           =  group
vdwtype                 =  cut-off
coulombtype             =  cut-off

pbc                     =  no
nstlist                 =  0
ns_type                 =  simple
rlist                   =  0            ; this means all-vs-all (no cut-off), which
                                        gets expensive for bigger systems
rcoulomb                =  0
rvdw                    =  0

comm-mode               =  angular
comm-grps               =  system

; V-rescale temperature coupling is on
Tcoupl                  =  v-rescale
tau-t                   =  0.1
tc-grps                 =  system
ref-t                   =  1443.15
; Pressure coupling is off
Pcoupl                  =  no
; Generate velocites according to a Maxwell distribution with a pseudo-random seed
gen-vel                 =  yes
gen-temp                =  1443.15
gen-seed                =  -1

; Implicit solvent
implicit-solvent        =  GBSA
gb-algorithm            =  Still        ; HCT ; OBC
nstgbradii              =  1
rgbradii                =  0            ; [nm] Cut-off for the calculation of the Born
                                        radii. Currently must be equal to rlist
gb-epsilon_solvent      =  1.0003623353 ; Dielectric constant for nitrogen at 170 °C
sa-algorithm            =  Ace-approximation
sa-surface_tension      =  2.05016      ; with still; -1  ; 2.25936; with HCT/OBC
```

Matlab main_script.m

```
clear;

%Define the peptide name and the path where the data will be stored.
%The xyz*.txt and PotEnerHT*.txt files need to be in /pathname/
name = ('peptidename');
pathname = ('path/to/stored/data/peptidename/');
workdir=fullfile('/path/to/MD/folder/',name);

%Import data generated with previous script
traj=load(sprintf('%sxyz%s_HT.txt',pathname,name));
PotEnerHT=importdata(sprintf('%sPotEnerHT_%s.txt',pathname,name));
```

```
%Determine the time step in the simulation
delta_t=PotEnerHT(2,1)-PotEnerHT(1,1);

%Set the running average window
window=10;

%for n_frames and n_atoms to work, the step and the writing frequency of
%the md.mdp file have to be the same --> frames in traj = steps written
n_frames=size(PotEnerHT,1);
n_atoms=size(traj,1)/n_frames;

%Re-size PotEnerHT to chi size
for i=1:n_frames-window
   PotEnerHT(i,1)=mean(PotEnerHT(i:i+window,2));
end
PotEnerHT=PotEnerHT(1:n_frames-window,1);

%Define the number of independent bases and their size
n_dist=[16,16,16,16];

%Enter high temperature used and target low temperature
hightemperature=1443.15;
lowtemperature=293.15;

%Determine indicator distances for all bases by running pre_analyze2
frame_dist=[];v1=[];v2=[];
for i=1:length(n_dist)
    [frame_dist1, v11, v21]=pre_analyze2(traj, n_atoms, n_frames, n_dist(i));
    frame_dist=[frame_dist, frame_dist1];
    v1=[v1, v11];
    v2=[v2, v21];
end
clearvars frame_dist1 v11 v21 i;

%Perform running average
for i=1:size(frame_dist,1)-window
   Mtilde(:,i)=transpose(mean(frame_dist(i:i+window,:)));
   stdtilde(:,i)=transpose(std(frame_dist(i:i+window,:)));
end

%%
%Run PCCA+ script
PCCA_script;

%Determine the low temperature distribution
stat_weight=mean(chi)

%Run thermodynamic reweighting
Reweighting2;
```

Matlab function pre_analyze2.m

```
function [frame_dist, v1, v2]=pre_analyze2(traj, n_atoms, n_frames, n_dists)
```

```
%Define a random set of atoms to become a basis
v1=randperm(n_atoms);
v2=randperm(n_atoms);

v1=v1(1:n_dists);
v2=v2(1:n_dists);

% Reshape trajectory into a manageable form
traj = reshape(traj, 3, n_atoms, n_frames);

% Compute indicator distances for all frames
frame_dist=zeros(n_frames, n_dists);
for i=1:n_frames
        frame_dist(i,:)=sum((traj(:,v1,i)-traj(:,v2,i)).^2);
end

end
```

Matlab script Reweighting2.m

```
%High temperature statistics through HTstats3 script
[frameChi, U_HT, deltaU_HT]=HTstats3(n, window, frame_dist, M, chi, PotEnerHT,
name, pathname);

%Set the environmental variables to those in bash
path1 = getenv('PATH');
path1 = ['/path/to/gromacs-5.1.1/bin:/path/to/amber14/bin:' path1];
setenv('PATH', path1);
setenv('GMXLIB', '/path/to/Gromacs/top');
lib1 = getenv('LD_LIBRARY_PATH');
lib1 = ['/path/to/amber14/lib' lib1];
setenv('LD_LIBRARY_PATH', lib1)
clearvars path1 lib1

%Send to system bash script and arguments for the extraction of the frames with higher
degree of belonging to a given conformation Energy minimization of those states.
Extraction of the minimized energies.
pathToScript=fullfile('/path/to/bash/scripts/','Batch_trjconv2_neu.sh')
cmdStr = sprintf('"%s" "%g" "%s" "%s" "%g"', pathToScript, delta_t, name, workdir,
window)
[status,cmdout] = system(cmdStr,'-echo')

%Import the minimized energies
MinEner=importdata(sprintf('%sMINIMIZED_ENERGIES_%s.txt',pathname,name));
MinEner=sortrows(MinEner,1);

%Get the conformation energy per chosen frame
j=0;
Enerdecomp=zeros(size(frameChi,1),n+1+1);
for i=1:size(frameChi,1)
   Enerdecomp(i,:)=[MinEner(j+i,1),MinEner(j+i,2)*frameChi(i,2:n+1+1)];
end
clearvars j
```

```
%Get energy minima for every conformation
E_minima=min(Enerdecomp);
E_minima(:,1)=[];

%Compute energy differences delta AB ==> B-A, ln(A/B)
energy_diffs=zeros(n+1);
delta_F_HT=zeros(n+1);
delta_F=zeros(n+1);
beta0=1/(hightemperature*0.0083144621);
beta=1/(lowtemperature*0.0083144621);
for i=1:n+1
   for j=1:n+1
      energy_diffs(i,j)=E_minima(j)-E_minima(i);
      delta_F_HT(i,j)=-1/beta0*log(stat_weight(i)/stat_weight(j));
      delta_F(i,j)=1/beta*((beta-
beta0)*energy_diffs(i,j)+log(beta/beta0)*beta0*(deltaU_HT(i,j)-
energy_diffs(i,j))+beta0*delta_F_HT(i,j));
      end
end
clearvars i j;

%Get low temperature statistics
syst=ones(n+1,1);
syst=diag(syst);
for i=1:n+1-1
   syst(i,i+1)=-exp(delta_F(i+1,i)*beta);
end
syst(n+1,1:n+1)=1;
sol=zeros(n+1,1);
sol(n+1)=1;

clearvars i j;

lowT_stats=linsolve(syst,sol)

%Summarize results in a text file
name2 = sprintf('%s%s_frameChi.txt',pathname,name);
fileID = fopen(name2, 'a');
   fprintf(fileID, '\nDistribution at %.2f K \n',lowtemperature);
   fprintf(fileID, '%d ',lowT_stats);
   fprintf(fileID, '\n');
fclose(fileID);
clearvars name2 fileID;
```

Matlab function HTstats3.m

```
function [frameChi, U_HT, deltaU_HT]=HTstats3(n, window, frame_dist, M, chi,
PotEnerHT, name, pathname)

%For each conformation extract the index of the frame which is the most
%like this conformation and then the conformational distribution for that
%frame. Then convert from chi indices to frame_dist indices.
[~,frame_idx]=max(chi);
```

```
for i=1:size(frame_idx,2)
    extract=frame_dist(frame_idx(i):frame_idx(i)+window,:);
    d=ones(size(extract,1),1)*M(frame_idx(i),:);
    d=d-extract;
    d=sum(d.^2,2);
    [~,MIN]=min(d)
    frameChi(i)=MIN(1)+frame_idx(i)-1;
end


frameChi=transpose(frameChi);


for i=1:size(frame_idx,2)
    frameChi=[frameChi,transpose(chi(frame_idx(i),:))]
end

%Export information to text files
name1 = sprintf('%s%s_frameidxs.txt',pathname,name);
fileID = fopen(name1, 'w');
fprintf(fileID, '%d ',unique(frameChi(:,1)));
fclose(fileID);

name2 = sprintf('%s%s_frameChi.txt',pathname,name);
fileID = fopen(name2, 'w');
for i=1:size(frameChi,1)
    fprintf(fileID, '%d ',frameChi(i,:));
    fprintf(fileID, '\n');
end
fclose(fileID);

name3 = sprintf('%s%s_windowidxs.txt',pathname,name);
fileID = fopen(name3, 'w');
fprintf(fileID, '%d ',frame_idx(1,:));
fclose(fileID);

%Potential energy average for each conformation over trajectory window
U_HT=chi'*PotEnerHT./sum(chi)';

%delta AB ==> B-A, delta columnrow ==> row-column
deltaU_HT=zeros(n+1);
for i=1:n+1
    for j=1:n+1
        deltaU_HT(i,j)=U_HT(j)-U_HT(i);
    end
```

Bash script Batch_trjconv2_neu.sh

```
#!/usr/bin/bash

timestep=$1
peptidename=$2
workdir=$3
window=$4
```

```
echo $timestep $peptidename $workdir

#Find the folder where the list of frames (Matlab output) is and get this list, store it in a variable
#read peptidename
framelistpath=$(find /path/to/stored/data -name ${peptidename}_frameidxs.txt -print)
framelist=$(cat $framelistpath)

windowlistpath=$(find /path/to/stored/data -name ${peptidename}_windowidxs.txt -print)
windowlist=$(cat $windowlistpath)


#Go to the directory where all the GROMACS md run files are
cd $workdir

basename=$(echo HT*md.trr)
basename=${basename%.trr}

pwd

#Create a file to store all the energies after minimization
touch MINIMIZED_ENERGIES.txt


#Do in parallel, for all the frames in the list
for frame in $windowlist
do

    #translate the frame number into time
    let "frame_i=${frame}-1"
    let "frame_e=${frame}+${window}-2"
    time=$(echo ${timestep}*${frame_i} | bc)
    time_end=$(echo ${timestep}*${frame_e} | bc)
    #set names to use, create subdirectory to store specific outputs per frame, go there
    subdir=In${frame}_W${window}_${basename}
    subname=${basename}_${frame}
    mkdir $subdir
    cd $subdir

    #extract the structure corresponding to the frames in framelist as a pdb file and when
    prompted by trjconv answer always "0" (whole system)
    yes 0 | gmx trjconv -f ../${basename}.trr -s ../${basename}.tpr -b ${time} -e
    ${time_end} -o ${subname}.pdb -sep

    #Convert pdb to xyz for later use with MOBCAL
    babel -ipdb *.pdb -oxyz *.xyz

    #create a file storing the charges for later introduction into .mfj file produced by
    mobcal parser
    grep qtot ../*.top | sed 's/^.\{48\}//' | sed 's/\(.......\).*/\1/' > charges.txt

        chargesfile='charges.txt'
        chargelines=$(cat ${chargesfile})
        for line in $chargelines ; do
```

```
            LC_NUMERIC="en_US.UTF-8" printf '% .5f\n' "$line" >>
            charges_${peptidename}.txt
        done

    rm *.pdb
    rm charges.txt

    cd $workdir
done

#wait for all the parallel runs started in the for loop (wait for all the previous code) to be
executed before continuing
wait

#Do in parallel, for all the frames in the list
for frame in $framelist
do

    #translate the frame number into time
    let "frame_i=${frame}-1"
    time=$(echo ${timestep}*${frame_i} | bc)

    #set names to use, create subdirectory to store specific outputs per frame, go there
    subdir=${frame}_${basename}
    subname=${basename}_${frame}
    mkdir $subdir
    cd $subdir

    #extract the structure corresponding to the frames in framelist as a pdb file and when
    prompted by trjconv answer always "0" (whole system)
    yes 0 | gmx trjconv -f ../${basename}.trr -s ../${basename}.tpr -dump ${time} -o
    ${subname}.pdb

    #assemble run files for energy minimization and run energy minimization
    #CAREFUL!! --> it is assumed the topology filename is the default topol.top
    gmx grompp -f ../../imp_water_em.mdp -c ${subname}.pdb -p ../topol.top -o
    ${subname}_em.tpr
    gmx mdrun -nt 1 -deffnm ${subname}_em

    #extract the potential energy info line from the run log and store it in the text file
    created before as two columns with the frame number and the potential energy info
    energyvar=$(grep "Potential Energy  =" ${subname}_em.log)
    printf "%-10s  %-40s\n" "$frame" "$energyvar" >> ../MINIMIZED_ENERGIES.txt

    cd $workdir
done

#wait for all the parallel runs started in the for loop (wait for all the previous code) to be
executed before continuing
wait

#get rid of useless info
sed 's/Potential Energy  =//g' MINIMIZED_ENERGIES.txt >
MINIMIZED_ENERGIES_${peptidename}.txt
rm MINIMIZED_ENERGIES.txt
```

```
cp MINIMIZED_ENERGIES_${peptidename}.txt /path/to/stored/data/${peptidename}
```

Bash script Batch_xyzgrab.sh

```
#!/bin/bash

#List all the peptide subfolders there are and save them to a variable
folderlist=$(ls -d */)
mkdir -p XYZ

#Do in parallel, for all the folders in the list
for folder in $folderlist
do
    #Enter folder. Define peptide name
    cd $folder
    peptidename=$(echo $folder | sed s'/.$//')
    subfolderlist=$(echo In*)
    cp -r $subfolderlist ../XYZ/
    cd ../
done
```

Bash script execPARSER_xyz.sh

```
#!/bin/bash
# careful: mobcalPARSER_008_JAV.pl and config.cfg must be in same folder
# mobcalPARSER_008.pl must be executable

for diro in $(find ./* -maxdepth 1 -type d); do
        cp config.cfg mobcalPARSER_008_JAV.pl MFJedit.awk "$diro"/
        cd "$diro"
        filo=$(echo charges*.txt)

        #Run mobcal parser
        ./mobcalPARSER_008_JAV.pl
        mv MOBCAL.mfj MOBCAL2.mfj

        #Edit output of parser with awk
        ./MFJedit.awk $filo MOBCAL2.mfj > MOBCAL.mfj
        rm config.cfg mobcalPARSER_008_JAV.pl MFJedit.awk MOBCAL2.mfj
        cd ..
done

#Did the parser screw up and give some non-integer random seeds?
echo "Non-integer random seed:"
echo $(find ./*/mobcal.run -type f | xargs grep "[0-9]*\.[0-9]")

echo "Empty:"
echo $(find ./*/ -type f -empty)
```

Awk script MFJedit.awk

```
#!/usr/bin/awk -f
```

```
#first charges file. store charges
FNR==NR{
   ch[NR]=$1;next;
}FNR!=NR{  #second file
#store number of structures
   if (FNR==2) {
      n[FNR]=$1;
   } else if (FNR==3) {
#store number of atoms
      n[FNR]=$1;
   } else if (FNR==5) {
      $1="calc";
#loop over structures and atoms starting with line 7 of mfj file
   } else {
            for (j=1; j<=n[2];j++){
                  for (i=1; i<=n[3]; i++){
                     if(FNR==6+(n[3]+1)*(j-1)+i) {
#replace column 5 with value in stored charge array and format every column to keep
spacings.
                        var[FNR]=sprintf("%16.5f%16.5f%16.5f%10.0f%16.6f", $1, $2, $3,
$4 , ch[i]); $0=var[FNR];
                        }
         }
      }
   }
}1
```

Bash script morunnerN2_fast.sh

```
#!/bin/bash

for dddn in $(find ./* -type d); do
            cp mobcalN2_fast_v11_293 ${dddn}/
            cd $dddn
            if [ ! -f *.mob ]; then
                        date
                        echo "$dddn"
                        (time ./mobcalN2_fast_v11_293 && echo "$dddn") &
            fi
            cd ..
done

wait

for dddn in $(find ./* -type d); do
            cd $dddn
            mkdir -p ../done/
            cp *.mob ../done/
            rm mobcalN2_fast_v11_293
            echo
"========================================================="
            echo
            cd ..
done
```